Imperial College of Science, Technology and Medicine
Department of Aeronautics

Optimisation of 3D printed composite fibre structures

Luo, Yi-Rong
Supervisors: Prof. Robert Hewson & Prof. Matthew Santer

Submitted in part fulfilment of the requirements for the degree of
Doctor of Philosophy in the Department of Aeronautics of Imperial College London,
September 2024

Abstract

A novel design approach for 3D printed fibre-reinforced composite structures that combines topology and fibre orientation optimisation is presented in this thesis. Solid Isotropic Material with Penalisation (SIMP) and Continuous Fibre Angle Optimisation (CAFO) method are developed to determine the optimal design of fibre-reinforced composites subject to a range of requirements including buckling resistance. A continuity equation is adopted to constrain fibre orientation and ensure continuous fibres within realistic fibre volume fractions. This results in fibre orientation with a corresponding and controllable variation of the fibre volume fraction. To ensure continuous fibre can be deposited, the manufacturability of the optimised results is ensured by introducing constraints controlled with two scalar fields to reconstruct fibre paths which are able to provide sufficient information to generate printer toolpaths. By considering realistic fibre volume fractions and manufacturability, numerical examples presented show that this approach successfully guarantees manufacturability with minimal loss of performance.

The design approach is developed to account for buckling resistance. The novelty of this extension lies in improving buckling resistance through varying both the topology layout and fibre orientation. Linear buckling analysis is applied to obtain the buckling characteristics. A stress field erosion and regularisation approach is adopted to alleviate the occurrence of spurious buckling modes during the optimisation process. Manufacturability is also considered while pursuing maximum buckling resistance. Numerical examples demonstrate a significant increase in buckling resistance and ensure manufacturability of optimal designs with little compromise in terms of stiffness.

Acknowledgements

I would like to express my sincere gratitude to Prof. Robert Hewson and Prof. Matthew Santer for their invaluable guidance, unwavering support, and encouragement throughout the duration of this research endeavour. Their academic expertise, insightful feedback, and mentorship have been instrumental in shaping this thesis.

I would like to express my gratitude to Ryan, Dilaksan, Morgan, and Wei for generously sharing their experiences, providing technical support, and engaging in insightful discussions. It is a pleasure to work alongside them.

I am also deeply grateful to the Chung-Cheng Institute of Technology for the financial support, which made this research possible. Their investment in academic excellence has been indispensable in facilitating the completion of this work.

Finally, I would like to extend my deepest gratitude to my wife Shao-Ying and daughter Yu-Ning, for their unwavering encouragement, companionship, and love throughout this academic journey. Their constant presence, understanding, and belief in me have been my source of strength and motivation. I am deeply grateful for their sacrifices and unwavering support, which have enabled me to pursue my academic and professional aspirations with determination and resilience. Their love and support have been invaluable, and I am truly blessed to have them by my side.

Statement of Originality

I hereby declare that contents of this thesis are original and have not been submitted in whole or in part for consideration for any other degree or qualification. The work presented herein is my own, and all ideas derived from others have been appropriately referenced. This thesis has also been reviewed by my supervisors before submission.

Copyright Statement

The copyright of this thesis rests with the author. Unless otherwise indicated, its contents are licensed under a Creative Commons Attribution-Non Commercial 4.0 International Licence (CC BY-NC).

Under this licence, you may copy and redistribute the material in any medium or format. You may also create and distribute modified versions of the work. This is on the condition that:

- You credit the author and do not use it, or any derivative works, for a commercial purpose.
- When reusing or sharing this work, ensure you make the licence terms clear to others by naming the licence and linking to the licence text. Where a work has been adapted, you should indicate that the work has been changed and describe those changes.

Please seek permission from the copyright holder for uses of this work that are not included in this licence or permitted under UK Copyright Law.

Nomenclature

Acronyms

AFP Automatic Fibre Placement

AM Additive Manufacturing

BESO Bi-directional Evolutionary Structural Optimisation

CAFO Continuous Fibre Angle Optimisation

CTS Continuous Tow Shearing

ESO Evolutionary Structural Optimisation

FDM Filament Deposition Modelling

FMO Free Material Optimisation

FRC Fibre-reinforced Composite

L-BGFS Limited-memory Broyden–Fletcher–Goldfarb–Shanno algorithm

LSF Level-set Function

LSM Level-set Method

SIMP Solid Isotropic Material with Penalisation

TFP Tailored Fibre Placement

TO Topology Optimisation

Greek Symbols

α	Angle between the gradients of the scalar fields
β	Projection parameter
Γ	Surface
γ	Number of considered eigenpairs
δ	Scalar value of the isosurfaces
ϵ	Linear strain
η	Projection parameter
η_k	Projection parameter for stiffness
η_σ	Projection parameter for stress stiffness
θ	First rotation angle
Λ	Solid domain
$\partial\Lambda$	Interface between void and solid
λ	Eigenvalue
λ_c	Critical buckling load factor
μ	Inverse buckling load factor
μ_{KS}	Aggregated inverse buckling load factor
ν_F	Poisson ratio interpolant (fibre direction)
ν_T	Poisson ratio interpolant (transverse directions)
ν_s	Poisson ratio (short random-oriented FRC)
ρ	pseudo-density

ρ_i Discrete density function

ρ_F Density of fibre

ρ_{min} Tolerance for stiffness matrix interpolant

$\overline{\rho}$ Filtered pseudo-density

$\widehat{\rho}$ Projected filtered pseudo-density

$\widehat{\rho_k}$ Projected filtered pseudo-density for stiffness

$\widehat{\rho_\sigma}$ Projected filtered pseudo-density for stress stiffness

σ Linear stress

$\widehat{\sigma}$ Filtered stress

ϕ Strain energy density

φ Second rotation angle

χ Set of design variables

$\overline{\chi}$ Set of filtered design variables

ψ Level-set function

$\boldsymbol{\psi}$ Eigenvector

Ω Design domain

ω Weight function

Roman Symbols

b	Width of the loading edge
c	Scaling constant
C_1	Set of the continuity constraints
C_2	Set of the fibre path generation constraints
D	Distance between isosurfaces
$E(\rho)$	Material stiffness interpolant
E_0	Young's modulus (void)
E_1	Young's modulus (solid)
E_f	Young's modulus (fibre)
E_m	Young's modulus (matrix)
E_s	Young's modulus (short random-oriented FRC)
E_F	Material stiffness interpolant (fibre direction)
E_T	Material stiffness interpolant (transverse directions)
$\boldsymbol{F}$	Body force
$\boldsymbol{f}$	External force
G_F	Shear modulus interpolant (fibre direction)
G_T	Shear modulus interpolant (transverse directions)
$\boldsymbol{G(u)}$	Global stress stiffness matrix
$\boldsymbol{G}_e$	Stress stiffness matrix of microscale model
$\widehat{\boldsymbol{G}_e}$	Penalised stress stiffness matrix of microscale model

J Objective function

J_0 Compliance of minimum compliance design

$\boldsymbol{K}$ Global stiffness matrix

$\boldsymbol{K}_e^0(V_f)$ Stiffness matrix of microscale model

$\boldsymbol{K}_e(V_f, \boldsymbol{U})$ Rotated stiffness matrix of microscale model

$\widehat{\boldsymbol{K}_e}$ Penalised stiffness matrix of microscale model

L_x Dimension of the design domain in x direction

L_y Dimension of the design domain in y direction

L_z Dimension of the design domain in z direction

N Number of elements

n Number of fibres within a deposited bundle

p Penalisation parameter

q Aggregation parameter

r_{min} Weighted average filter radius

r_h Helmholtz filter radius

r_f Radius of a single strand of fibre

r_σ Stress filter radius

S Scalar field design variable (2D)

S_1 Scalar field design variable

S_2 Scalar field design variable

t_p Psedudo time

$\boldsymbol{T}$	Transformation matrix
$\boldsymbol{t}$	Boundary traction
U_x	Component of fibre orientation vector in x direction
U_y	Component of fibre orientation vector in y direction
U_z	Component of fibre orientation vector in z direction
U_x"	Component of fibre orientation vector in x" direction (local coordinate system)
$\boldsymbol{U}$	Fibre orientation vector
$\boldsymbol{U'}$	Orthogonal fibre orientation vector (2D)
$\boldsymbol{u}$	Displacement
V	Volume of elements
V_f	Fibre volume fraction
V_F	Volume of fibre
V_m	Matrix volume fraction
V_0	Target volume
V_{LSF}	Velocity field of level-set function
$\boldsymbol{v}$	Adjoint displacement field
x	Coordinate axis
xyz	Global coordinate system
$x'y'z'$	Transit coordinate system
x"y"z"	Local coordinate system
$\boldsymbol{x}$	Design variables

Contents

Abstract **i**

Acknowledgements **iii**

Nomenclature **vi**

1 Introduction **1**

1.1 Thesis Objectives 3

1.2 Thesis Outline 4

1.3 Presentations and Publications 4

2 Review of Structural Optimisation **6**

2.1 Topology Optimisation 7

2.1.1 Discrete Approaches 8

2.1.2 Level-set Methods 9

2.1.3 Relaxation Approaches 10

2.1.4 Solid Isotropic Material with Penalisation 11

2.2 Fibre-reinforced Composites (FRCs) Optimisation 15

2.2.1 Optimality Criterion 16
2.2.2 Continuous Fibre Angle Optimisation 17
2.2.3 Discrete Material Optimisation 17
2.2.4 Lamination Parameters Parameterisation 18
2.2.5 Heuristic Approaches 18
2.2.6 Curvilinear Parameterisation 18
2.3 Topology and Fibre Orientation Optimisation 19
2.4 Manufacturing 21
2.5 Optimisation with Buckling Resistance 22
2.6 Summary 23

3 Topology and Fibre Orientation Optimisation Framework 25

3.1 Constitutive Law 25
3.2 Microscale Model 26
3.2.1 Material Properties 26
3.2.2 Rotation Function 27
3.3 Topology Optimisation 29
3.4 Manufacturing Constraints 30
3.4.1 Continuity Constraints 30
3.4.2 Fibre Path Generation Constraints 31
3.5 Optimisation Formulation 35
3.5.1 Variable Filter 35

3.5.2 Constraints formulations 36

3.5.3 Sensitivity analysis 37

3.5.4 Optimisation formulation 38

3.6 Summary 39

4 Fibre Orientation Optimisation Results 40

4.1 Cantilever Beam (2D) 41

4.1.1 Design without Manufacturing Constraints 42

4.1.2 Design with Manufacturing Constraints 43

4.2 Beam with Open Holes (2D) 46

4.2.1 Design without Manufacturing Constraints 47

4.2.2 Design with Manufacturing Constraints 48

4.3 Summary 51

5 Topology and Fibre Orientation Optimisation Results 52

5.1 Cantilever Beam 52

5.1.1 Problem Setup 54

5.1.2 Cases without Manufacturing Constraints 55

5.1.3 Cases with Manufacturing Constraints 60

5.2 Twisted and Compressed Column 67

5.2.1 Problem Setup 67

5.2.2 Design without Manufacturing Constraints 68

5.2.3 Design with Manufacturing Constraints 70
5.3 L-shape Beam 73
5.3.1 Problem Setup 73
5.3.2 Design without Manufacturing Constraints 73
5.3.3 Design with Manufacturing Constraints 75
5.4 Buckling Analysis of Optimal Design 84
5.5 Summary 84

6 Design for Buckling Resistance 88

6.1 Buckling Analysis 88
6.2 Strategy for Mode Switching 90
6.3 Spurious Modes Reduction 91
6.4 Sensitivity Analysis 92
6.5 Optimisation Formulations 94
6.6 Summary 95

7 Design for Buckling Resistance Results and Discussion 96

7.1 Parameters Setup 96
7.2 Compressed Column (2D) 97
7.3 Stubby Cantilever (2D) 104
7.4 MBB Beam (2D) 107
7.5 Twisted and Compressed Column 111
7.5.1 Minimum Compliance Design 112
7.5.2 Maximum Buckling Resistance Design 114
7.6 Summary 116

8 Conclusion **119**

8.1 Summary of Thesis Achievements 121

8.2 Limitations and Future Work 121

Bibliography **122**

List of Tables

2.1 Summary of common fabrication issues found in optimised designs 20

4.1 The problem setup of the 2D cantilever beam 42

4.2 The compliance comparison of the 2D cantilever beam 46

4.3 The problem setup of the 2D beam with open holes 48

4.4 The compliance comparison of the 2D beam with open holes 51

5.1 Scenarios for the cantilever beam design problem 53

5.2 The problem setup of the 3D cantilever beam 56

5.3 Comparison of compliance for the 3D cantilever beam 64

5.4 The problem setup of the twisted and compressed column 70

5.5 The comparison of the compliance of the twisted and compressed column 73

5.6 The problem setup of the L-shape beam 85

5.7 The comparison of the compliance of the twisted and compressed column 85

7.1 The problem setup of the 2D buckling resistance problems 98

7.2 The material and manufacturing constraints setup for the compressed column cases 100

7.3 The problem setup of the twisted and compressed column (maximisation of buckling resistance) 116

7.4 The summary of the buckling resistance 118

List of Figures

1.1 Optimisation results from (a) Papapetrou et al. (2020) and (b) Brampton et al. (2015) 2

2.1 Size, shape and topology optimisation examples 7

2.2 An example of a LSF and the corresponding domains 10

2.3 The effect of penalisation parameter p and the Hashin-Shtrikman (H-S) upper bound 12

2.4 The projection of the pseudo-density through different formulations 14

2.5 The curvilinear parameterisation example 19

3.1 The fibre orientation vector definition 27

3.2 Fibre path generation example 32

3.3 The cross section of deposited fibre bundles 33

4.1 The design domain and the boundary condition of the 2D cantilever beam . . . 41

4.2 Mesh convergence study for the 2D cantilever beam problem 41

4.3 The convergence plot of the 2D cantilever beam optimisation without manufacturing constraint 43

4.4 The optimised design of the cantilever beam without manufacturing constraints 44

4.5 The fibre paths of the 2D cantilever beam without manufacturing constraints . . 45

4.6 The convergence plot of the 2D cantilever beam optimisation with manufacturing constraints 45

4.7 The optimised fibre orientation and the fibre volume fraction of the 2D cantilever beam with manufacturing constraints 46

4.8 The fibre paths of the 2D cantilever beam with manufacturing constraints 46

4.9 The design domain and the boundary condition of the 2D beam with open holes 47

4.10 The convergence plot of the 2D beam with open holes optimisation without manufacturing constraints 47

4.11 (a) The fibre orientation and fibre volume fraction of the design without manufacturing constraints (b) The maximum principal stresses (c) The minimum principal stresses (d) The fibre paths generated using randomly seeded streamlines 49

4.12 The convergence plot of the 2D beam with open holes optimisation with manufacturing constraints 50

4.13 The optimised fibre orientation and the fibre volume fraction 50

4.14 The fibre paths of the 2D cantilever beam with manufacturing constraints 51

5.1 Geometry and boundary conditions of the cantilever beam 54

5.2 Mesh convergence study for the 3D cantilever beam problem 55

5.3 Optimised topologies of the 3D cantilever beam without manufacturing constraints 57

5.4 Comparison of the constant fibre volume fraction unidirectional case and the spatially-optimised case 58

5.5 The maximum and minimum principal stresses of the (a) Unidirectional case and (b) Spatially-optimised case (Note that the stress magnitude lower than 0.5 GPa is not shown for a better visualisation) 59

5.6 The convergence plots of the 3D cantilever beam without manufacturing constraints 61

5.7 The optimised topologies of the 3D cantilever beam with manufacturing constraints 62

5.8 The fibre orientation of the 3D cantilever beam with manufacturing constraints . 63

5.9 The principal stresses of the fibre path generation case 64

5.10 Fibre path generation of the 3D cantilever beam with manufacturing constraints 65

5.11 The convergence plots of the 3D cantilever beam with manufacturing constraints 66

5.12 The design domain and the boundary condition of the twisted and compressed column 68

5.13 The convergence plot of the twisted and compressed column optimisation 69

5.14 The optimised design of the 3D twisted and compressed column without manufacturing constraints 69

5.15 The build up plane example for the twisted and compressed column 69

5.16 The convergence plot of the twisted and compressed column optimisation with manufacturing constraint 71

5.17 The optimised design of the twisted and compressed column with manufacturing constraints 72

5.18 The isosurfaces of the scalar fields of the twisted and compressed column 72

5.19 The design domain of the L-shape beam 74

5.20 The convergence plot of the L-shape beam optimisation without the manufacturing constraints 74

5.21 The optimised topology of the L-shape beam without manufacturing constraints 76

5.22 The optimised fibre orientation of the L-shape structure without manufacturing constraints 77

5.23 The principal stresses of the L-shape structure without manufacturing constraints 78

5.24 The convergence plot of the L-shape beam optimisation with the manufacturing constraints 79

5.25 The optimised topology of the L-shape structure with manufacturing constraints 80

5.26 The optimised fibre orientation of the L-shape structure with manufacturing constraints 81

5.27 The isosurfaces of the L-shape beam 82

5.28 The fibre path of the L-shape beam 83

5.29 The first buckling mode of the optimised designs (Note that the buckling modes are coloured by the strain energy density, ϕ_e, using the scale of $\log(\phi_e/\phi_{max})$) . . 86

7.1 The design domain of the 2D buckling problems 99

7.2 The minimum compliance designs of the 2D compressed column 100

7.3 The buckling design of the 2D compressed column 101

7.4 The first buckling mode of the 2D compressed column 102

7.5 The convergence plots of the 2D compressed column 103

7.6 The minimum compliance design of the 2D stubby cantilever 104

7.7 The buckling design of the 2D stubby cantilever 105

7.8 The convergence plots of the 2D stubby cantilever 106

7.9 The minimum compliance design of the 2D MBB beam 108

7.10 The principal stresses of the 2D MBB beam minimum compliance design 108

7.11 The buckling design of the 2D MBB beam 109

7.12 The convergence plots of the 2D MBB beam 110

7.13 Mesh convergence plot of the twisted and compressed column 111

7.14 The minimum compliance design of the twisted and compressed column 112

7.15 The buckling design of the twisted and compressed column 113

7.16 The convergence plot of the 3D twisted and compressed column 113

7.17 The first and third buckling modes of (a) minimum compliance design and (b) buckling resistance design 115

Chapter 1

Introduction

Fibre-reinforced composites (FRCs) play an important role in many industries where weight is critical to efficiency and/or structural performance, due to their high strength and high stiffness-to-weight ratio. Traditional manufacturing approaches normally require complex processes and manual operation which increases the cost and limits wider application. The rapid development of additive manufacturing (AM) has changed the manufacturing and design approaches for FRCs. Fibres deposited using the AM processes follow programmed trajectories which enables the flexibility of steering the fibre orientation within the structure. Researchers have developed continuous fibre angle optimisation approaches to parameterise the fibre orientation to fully utilise the anisotropic properties and achieve optimal structural performance of a variable stiffness laminate (Pedersen, 1989; Gürdal et al., 2008; Cheng et al., 1994; Tosh and Kelly, 2000; Brampton et al., 2015; Khani et al., 2017).

A limitation of variable stiffness laminates is that they are naturally constrained within 2D stacks which results in a loss of some potential benefit from depositing fibres in 3D. The geometrical design flexibility is extended by the utilisation of advanced robotic 3D printers which makes it possible to deposit fibres out of the building plane (Huang et al., 2016). Research interest in the optimisation approaches then moves onto combining fibre orientation optimisation and topology optimisation (TO) to gain an advantage from anisotropic properties and extra lightweighting (Nomura et al., 2015; Lee et al., 2018; Boddeti et al., 2020; Caivano et al., 2020; Papapetrou et al., 2020; Schmidt et al., 2020; Jantos et al., 2020; Luo et al., 2023).



(a) (b)

Figure 1.1: Optimisation results from (a) Papapetrou et al. (2020) and (b) Brampton et al. (2015) show gaps between fibre paths and sharp fibre turns

A common challenge of the optimisation approaches is that post-processing is typically needed to interpret fibre path from the optimal fibre orientation to enable fabrication. A few challenges are also commonly observed from the generated fibre path, for example, sharp fibre turns and gaps between the fibre paths (see Fig. 1.1). The sharp turns in the fibre path lead to high curvature of the deposited fibres which may result in them twisting or folding-back (Matsuzaki et al., 2018). The gaps between fibre paths result in generating voids, which decrease the fibre volume fraction. As a result, these issues may degrade the mechanical properties of the FRCs and potentially increase the chance of composite failure. Moreover, fibre paths have been interpreted by 3D streamlines, the most common way to interpret the fibre path, are difficult to be transferred to slicing software whilst still accounting for the fibre volume fraction variation.

The primary aim of this thesis is to address the challenge of interpreting the fibre path. By generating the fibre path within the optimisation approach, the extra effort of interpreting the fibre path in post-processing is no longer needed. Benefiting from the primary aim, the second aim of this thesis of tackling the manufacturing issues is easier to address since the fibre path is generated within the optimisation approach so that it can be constrained to avoid the potential problems. Although there is always a trade-off between the manufacturability and the structural performance, it is possible to generate manufacturable optimal designs by including manufacturing constraints.

Although the manufacturable optimal is able to achieve driven by this approach, potential buckling failure has been identified as a dominant design. Structural buckling can occur when their structural member is subjected to compression. The primary reason for a structure buckling is the inability of the structural member to withstand applied loads due to geometric

imperfections, boundary conditions, member slenderness, or material properties. Among these factors, the member slenderness ratio (defined as the length divide by the width or cross section area) is a major factor in determining the buckling resistance; for example, long and slender members are more likely to deflect laterally under compression (Bažant and Cedolin, 2010). Structures with slender members are frequently observed in topologically optimised designs due to the desired minimum weight requirements. Compared to isotropic materials, anisotropic fibre-reinforced composites can be loaded in the fibre direction to transfer loads more efficiently using less material. This may lead to the potential occurrence of extra slender compressed members, hence posing more risks for buckling.

Optimisation considering buckling for FRCs has mainly focused on laminate panels (Gürdal et al., 2008; Wu et al., 2012; Lindgaard and Lund, 2010). Studies have shown that parameterising fibre orientation can increase buckling resistance since compression stresses are redistributed through varying fibre orientation. Unlike fibre orientation optimisation, topology optimisation considering buckling modifies the structural topology and the thickness of members to enhance buckling resistance. By incorporating buckling resistance into the topology and fibre orientation optimisation process, it is possible to optimally distribute compression stress by modifying the topology and fibre orientation.

To achieve stable and manufacturable designs, the final aim of this thesis is to increase buckling resistance of FRC structures whilst simultaneously ensuring the manufacturability. Although considering buckling resistance whilst using the same amount of materials during TO may result in another compromise in structural stiffness due to the redistributed topology, achieving both objectives brings the designs closer to practical terms.

1.1 Thesis Objectives

The aims of this thesis are:

1. To develop a topology and fibre orientation optimisation approach that reduces the additional post-processing required for interpreting fibre path;

2. To apply manufacturing constraints targeting 3D printing technology to make the optimal designs realistic and manufacturable;

3. To increase the buckling resistance of the optimal designs whilst still ensuring their manufacturability.

1.2 Thesis Outline

The structure of this thesis is outlined as follows. Chapter 2 reviews relevant literature on structural optimisation, encompassing various TO approaches for determining the optimal structure layout. The optimisation approaches for FRCs are reviewed as well to determine a feasible approach for combining topology and fibre orientation optimisation. Additionally, the review of the manufacturing of 3D printed FRCs and their optimisation to account for buckling resistance provides awareness of fabrication and potential failure issues that need to be addressed.

Chapter 3 contains a detailed breakdown of the methodology applied to construct the combination of topology and fibre orientation optimisation and the manufacturing constraints. Chapter 4 presents the results derived using the methodology described in Chapter 3, considering fibre orientation optimisation solely, whilst the results of topology and fibre orientation optimisation are demonstrated in Chapter 5.

Chapter 6 provides a detailed breakdown of the methodology applied to account for buckling resistance, with corresponding results presented in Chapter 7. Finally, conclusions are drawn in Chapter 8.

1.3 Presentations and Publications

Conference Presentations

Luo, YR., Hewson, R. & Santer, M., Continuous fibre composites optimisation with buckling and additive manufacturing constraints. The 15th World Congress of Structural and Multidisciplinary Optimisation, Cork, Ireland (2023).

Journal Papers

Luo, YR., Hewson, R. & Santer, M. Spatially optimised fibre-reinforced composites with isosurface-controlled additive manufacturing constraints. *Structural and Multidisciplinary Optimisation* 66, 130 (2023). https://doi.org/10.1007/s00158-023-03586-w

Luo, YR., Hewson, R. & Santer, M. Topology optimisation of fibre-reinforced composites accounting for buckling resistance and manufacturability. *Structural and Multidisciplinary Optimisation* 67, 172 (2024). https://doi.org/10.1007/s00158-024-03895-8

Chapter 2

Review of Structural Optimisation

Structural optimisation is a numerical approach that combines the principles of structural mechanics and mathematical optimisation to achieve one or multiple objectives subject to predefined design criteria (Christensen, 2008). Common objectives include i) maximising stiffness subject to volume constraint or ii) minimising volume subject to stress or displacement constraints. This approach has been widely adopted by the aeronautics and automotive industry due to its potential to improve operational efficiency and reduce costs whilst meeting the mechanical design criteria (Keane and Nair, 2005).

The purpose of structural optimisation is to determine the optimal structural layout. Optimisation approaches such as size, shape and topology have been used to determine the optimal structural layout. Size optimisation involves determining the size of specific features, such as the radius of members in truss structures and the thickness of plies in composite structures. In these cases, the model and the domain are fixed and known before the optimisation process. Shape optimisation focuses on reshaping the structure's layout, resulting in changes to the design domain during optimisation. Topology optimisation determine structural features such as the number, location, and shape of holes, as well as the connectivity of these features within a fixed design domain (Bendsøe and Sigmund, 2004). An example is shown in Fig. 2.1 to illustrate these optimisation approaches. Within these aspects, TO is the sole focus of this thesis.

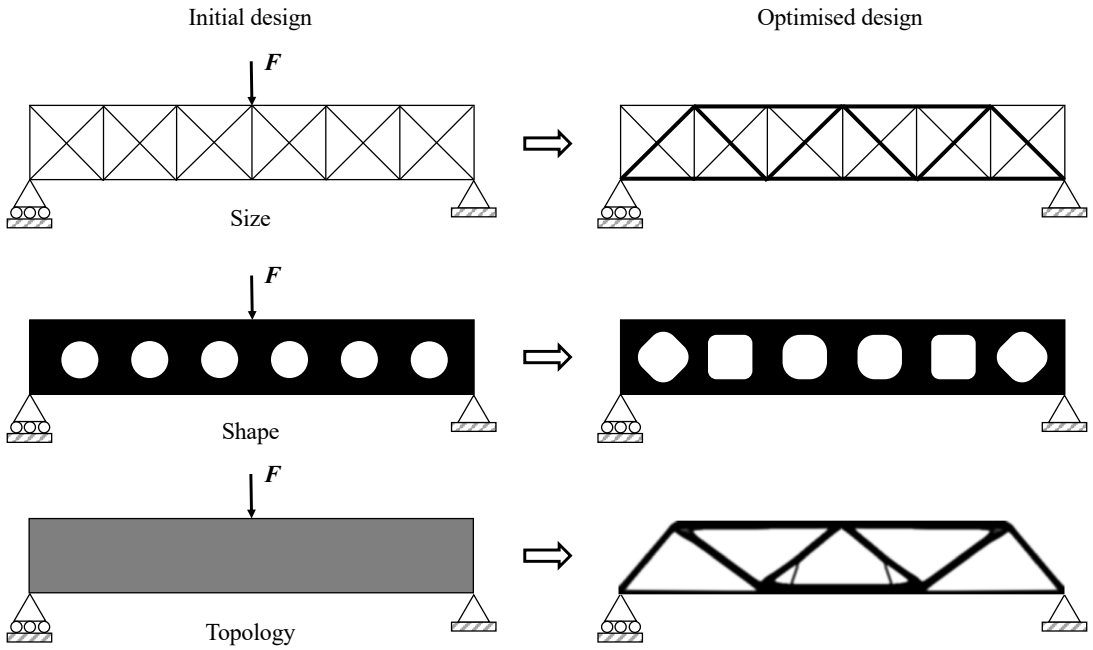


Figure 2.1: Size, shape and topology optimisation examples. The materials are distributed to achieve optimal design through each mechanism. Adapted from Bendsøe and Sigmund (2004)

2.1 Topology Optimisation

TO aims to find an optimal structural layout within a specific region where the size, shape, and topology are unknown prior to the optimisation. The possible known information includes the design domain, loading and support conditions, target volume fraction, or prescribed solid or void regions. The size, shape, and topology are described by a set of functions that represent the material distribution instead of standard parametric functions. These functions are used to interpret the stiffness tensor to evaluate the continuum structural performance. The performance is used by the mathematical optimisation approach as either objectives or constraints to update the structure layout to achieve the optimisation objective (Bendsøe and Sigmund, 2004).

A general form of a structural TO problem can be written as

$$\begin{aligned} \min_{\boldsymbol{x}} \quad & J(\boldsymbol{u}(\boldsymbol{x}), \boldsymbol{x}) \\ s.t. \quad & \int_{\Omega} E_{ijkl}(\boldsymbol{x})\epsilon_{ij}(\boldsymbol{u})\epsilon_{kl}(\boldsymbol{v})d\Omega + \int_{\Omega} \boldsymbol{F}\boldsymbol{v}d\Omega + \int_{\Gamma} \boldsymbol{t}\boldsymbol{v}d\Gamma \\ & \int_{\Omega} V(\boldsymbol{x})d\Omega - V_0 \leq 0 \end{aligned} \tag{2.1}$$

where J denotes the objective function, $\boldsymbol{u}$ denotes the displacement, $\boldsymbol{x}$ denotes the design variables, Ω denotes the design domain, E_{ijkl} denotes the stiffness tensor, ϵ denotes the linear strain, $\boldsymbol{F}$ denotes the body forces, $\boldsymbol{v}$ denotes the virtual displacement, Γ denotes the boundary surfaces, $\boldsymbol{t}$ denotes the surface traction, V denotes the volume of the elements and V_0 denotes the target volume. The linear strains are derived from the displacement field by

$$\epsilon_{ij} = \frac{1}{2}\left(\frac{\partial u_i}{\partial x_j} + \frac{\partial u_j}{\partial x_i}\right) \tag{2.2}$$

where x represent the coordinate axis. Solutions for TO problems described by Eq. (2.1) generally do not exist due to the generation of a larger number of holes leading to a lower objective value (Sigmund and Petersson, 1998). Equation. (2.1) can be solved using computational methods by discretising the domain into N elements and using an element-wise function, ρ_i, to describe the existence of material as

$$\begin{aligned} E_{ijkl}(\boldsymbol{x}) &= \rho_i E^0_{ijkl}, \quad i \in 1 \cdots N \\ \rho_i &= \begin{cases} 1 & \text{if element } i \text{ represents solid} \\ 0 & \text{if element } i \text{ represents void} \end{cases} \end{aligned} \tag{2.3}$$

The discretised TO problem now has solutions since they are posed in finite dimensions, although a numerical instability similar to the original issue, which is termed mesh-dependence, is observed in the solutions, where the number of holes increases as N increases (Sigmund and Petersson, 1998). Additionally, the discretised problems are numerically difficult to solve using the binary discrete variables. Various approaches have been developed to overcome the difficulties and solve the TO problems.

2.1.1 Discrete Approaches

The difficulty of solving discrete TO problems using binary variables limits the size of the problems that can obtain global optimal solutions (Stolpe and Bendsøe, 2011; Svanberg and Werme, 2006). A branch of development in discrete approaches chooses to use non-gradient-based optimisation methods to overcome this limitation and improve the efficiency.

Evolutionary Structural Optimisation (ESO) is inspired by the growth and adaptation mechanisms observed in biological systems. Mattheck and Burkhardt (1990) mimic the process of tree growth to optimise the topology through stress analysis. An evolutionary procedure is applied by Xie and Steven (1993) to update the discrete variables using a rejection criterion based on von Mises stress. However, ESO approaches are easily trapped in local minima since once the material is removed, it cannot be reintroduced in the rest of the optimisation procedure. To circumvent this issue, Bi-directional Evolutionary Structural Optimisation (BESO) was introduced, which permits the removal and addition of material (Young et al., 1999). In this framework, materials can be reintroduced if the stresses in neighbouring elements are sufficiently large. Although the issue of local minima is avoided, a problem of lacking algorithmic convergence to determine the stopping criteria still exists.

ESO and BESO approaches demonstrate efficient ability to provide solutions to discrete TO problems; however, due to the inherent limitations of evolutionary approaches, the number of design variables is still limited compared to gradient-based approaches (Sigmund and Maute, 2013).

2.1.2 Level-set Methods

Instead of using the binary variables to describe the solid and void region, level-set method (LSM) implicitly uses a level-set function (LSF) to describe the topology (Osher and Sethian, 1988; Sethain, 1999; Allaire et al., 2002, 2004; Wang et al., 2003). An example of LSF is shown in Fig. 2.2 where Ω denotes the design domain, $\partial\Lambda$ denotes the interface and Λ denotes the solid domain. The topology boundary is typically defined using the interface of the LSF and the zero level, $\psi(\boldsymbol{x}) = 0$, so that the solid and void regions can be defined as

$$\begin{cases} \psi(\boldsymbol{x}) > 0 & \Leftrightarrow \forall \boldsymbol{x} \in \Lambda \quad \text{(Solid)} \\ \psi(\boldsymbol{x}) = 0 & \Leftrightarrow \forall \boldsymbol{x} \in \partial\Lambda \quad \text{(Interface)} \\ \psi(\boldsymbol{x}) < 0 & \Leftrightarrow \forall \boldsymbol{x} \in \Omega \setminus \Lambda \quad \text{(Void)} \end{cases} \tag{2.4}$$

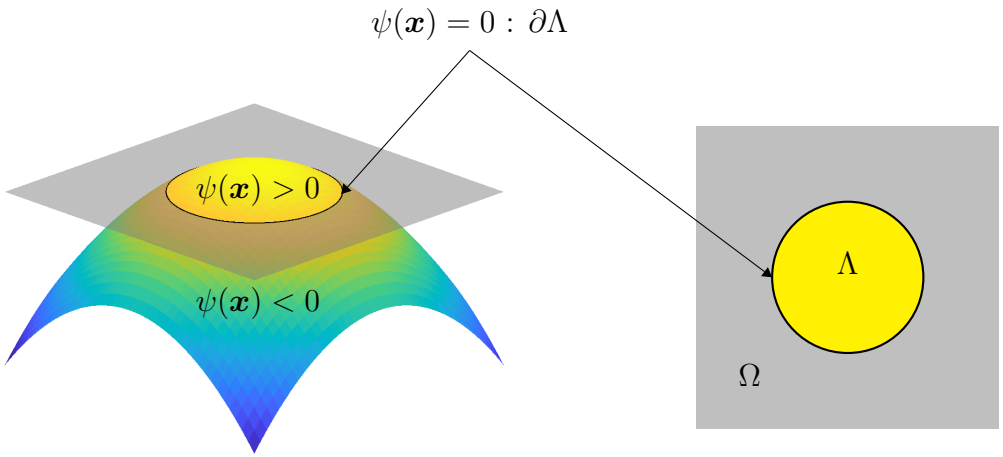


Figure 2.2: An example of a LSF and the corresponding domains adopted from Luo et al. (2008) (Ω: design domain; Λ: solid domain; $\partial\Lambda$: interface)

The LSF is typically updated by the solution of Hamilton-Jacobi equation

$$\frac{\partial\psi(\boldsymbol{x})}{\partial t_p} + V_{LSF}|\nabla\psi(\boldsymbol{x})| = 0 \tag{2.5}$$

where t_p is a pseudo time representing the progress of the optimisation and V_{LSF} denotes a velocity field that represents the sensitivity of the moving interface of the LSF. As the LFS is being iteratively updated using Eq. (2.5), the LSF evolves only along the interfaces of the initial design, resulting in an inability to create new holes and new shape geometries. This leads to a likelihood of tending toward to local-minima (Dijk et al., 2013). To circumvent this, extensions of this method have been proposed (Burger et al., 2004; Fulmanski et al., 2008; Yamasaki et al., 2010) which use topological derivatives to create new holes.

2.1.3 Relaxation Approaches

To address the challenge of solving discretised TO problems using binary variables, researchers have explored reformulating the problems to allow intermediate material distributions. The seminal work of Bendsøe and Kikuchi (1988) introduced the concept of multiscale optimisation, which considers heterogeneous material properties on multiple length scales. This approach enables the interpretation of intermediate materials at the microscale, with element-wise material

properties represented by microscale structures or composite materials through homogenisation theory (Suzuki and Kikuchi, 1991).

Free material optimisation (FMO) has also emerged (Bendsøe et al., 1994; Zowe et al., 1997; Kocvara et al., 2008), allowing for direct interpretation of element-wise material properties using the symmetric and semi-definite elasticity tensor. This enables continuous variations in the material properties, facilitating the creation of more complex and intricate designs. However, the flexibility in material property variation may lead to solutions that are challenging to implement in reality due to the non-existence of certain materials.

2.1.4 Solid Isotropic Material with Penalisation

Solid Isotropic Material with Penalisation (SIMP) is one of the most widely used approaches in TO (Bendsøe, 1989; Zhou and Rozvany, 1991). This approach relaxes the binary variables, allowing them to vary continuously within the interval [0, 1]. One advantage of this continuous description is that it enables the use of gradient-based optimisation approaches to reduce the computational cost. However, a disadvantage of this approach is that it permits the existence of intermediate materials, which do not exist in reality. To discourage the existence of these intermediate materials, the Young's modulus is penalised by a power of the penalisation parameter, p, such that

$$E(\rho) = E_0 + (E_1 - E_0)\rho^p \tag{2.6}$$

where $E(\rho)$ denotes the material stiffness as a function of the pseudo-density, whilst E_0 and E_1 represent the Young's modulus of the void and solid materials, respectively. To illustrate the effect of penalisation, the penalised stiffness with respect to the pseudo-density is shown in Fig. 2.3. The stiffness of the intermediate materials decreases significantly as the penalisation parameter increases. The penalisation results in a more binary distribution of pseudo-density to enhance stiffness because the stiffness of the intermediate materials per unit volume is lower compared to the case when the penalisation is not applied. It is important to note that this approach is only effective when a volume constraint or other constraints that implicitly limit the volume are applied (Sigmund and Maute, 2013).

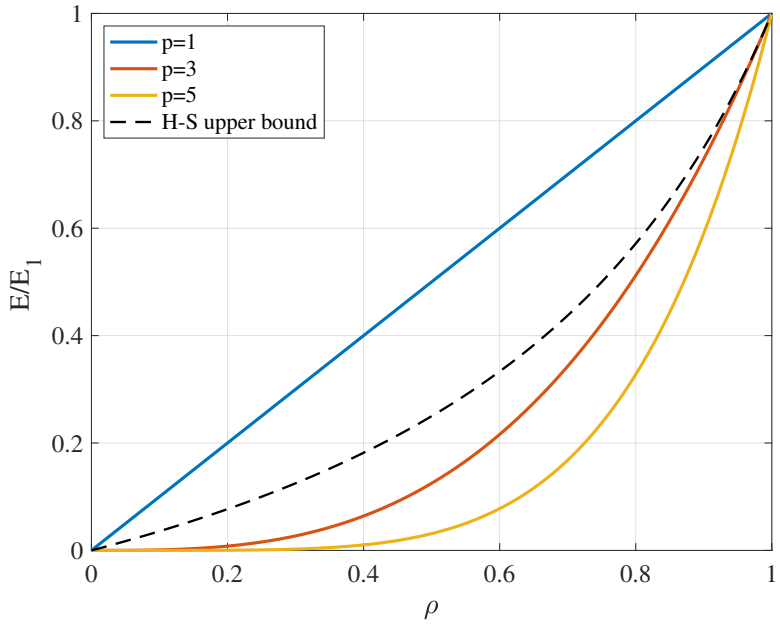


Figure 2.3: The effect of penalisation parameter p and the Hashin-Shtrikman (H-S) upper bound describing the realisation of intermediate densities

Setting the value of the penalisation parameter is often challenging because different values of the penalisation parameter leads to distinct optimal designs. When solving a compliance objective problem using linear interpolation ($p = 1$), the optimisation problem has been proved convex (Petersson, 1999; Bendsøe and Sigmund, 2004), but the optimal design is typically not-physical due to the existence of large regions of intermediate materials. Using a high penalisation parameter results in a more binary distribution of the pseudo-density, but the optimisation is more likely to converge to a local minimum due to the highly nonlinear penalisation. A general widely used value to generate a nearly binary design is $p = 3$. This value has also been demonstrated to produce physically realisable binary designs and satisfy the Hashin-Shtrikman upper bound (Bendsøe and Sigmund, 1999). It is important to note that the decision of the penalisation value needs to be adjusted depends on the physical problem being solved. For example, the penalisation value should be high enough to provide sufficient penalisation whilst solving the structural compliance minimisation problem (Sigmund and Maute, 2013).

One common issue encountered in the implementation of TO is the checkerboard problem, which refers to patches of elements exhibiting alternating high and low pseudo-density values, attributed to the usage of low-order elements and assumptions of the finite element method (Díaz and Sigmund, 1995; Jog and Haber, 1996). This issue can be addressed through the adop-

tion of higher-order elements and regularisation techniques. One such regularisation approach is the sensitivity filter proposed by Sigmund and Petersson (1998), which modifies sensitivities using weighted averages based on the distance between neighbouring elements. The sensitivity filter equation is defined as

$$\frac{\partial \overline{J}}{\partial \rho_e} = \frac{1}{\rho_e \sum_i^N w_i} \sum_i^N w_i \rho_i \frac{\partial J}{\partial \rho_i} \tag{2.7}$$

where w_i is the weight function defined as

$$w_i = r_{min} - \text{dist}(e,i), \{i \in N | \text{dist}(e,i) \leq r_{min}\} \tag{2.8}$$

Here, r_{min} denotes the filter radius, and $\text{dist}(e,i)$ denotes the distance between element e and i. The weight function linearly decays along $\text{dist}(e,i)$ and becomes zero when $\text{dist}(e,i)$ is greater than r_{min}. Similarly, the weighted averages approach is adopted to regularise the pseudo-density field, defined as (Bruns and Tortorelli, 2001; Bourdin, 2001)

$$\overline{\rho_e} = \frac{\sum_i^N w_i \rho_i}{\sum_i^N w_i} \tag{2.9}$$

Alternatively, the pseudo-density regularisation can be achieved implicitly by solving a Helmholtz type partial differential equation, as proposed by Lazarov and Sigmund (2011)

$$-r_h^2 \nabla^2 \overline{\rho} + \overline{\rho} = \rho \tag{2.10}$$

where r_h denotes the Helmholtz filter parameter, which imposes a length scale control such as the radius, r_{min}, of the weighted averages filter. By setting $r_h = \frac{r_{min}}{2\sqrt{3}}$, the Helmholtz PDE filter can impose an equal length scale to the weighted averages filter.

These regularisation approaches can successfully address the checkerboard issue and lead to filter radius dependant solutions. However, implementing these filters results in a transition region of intermediate pseudo-density between solid and void. Subsequently, extensions of the regularisation filters are dedicated to alleviating the intermediate pseudo-density region through projection schemes. The projection schemes introduce an extra pseudo-density field, $\widehat{\rho}$, using projection formulations. Guest et al. (2004) proposed a projection formulation as (see Fig. 2.4

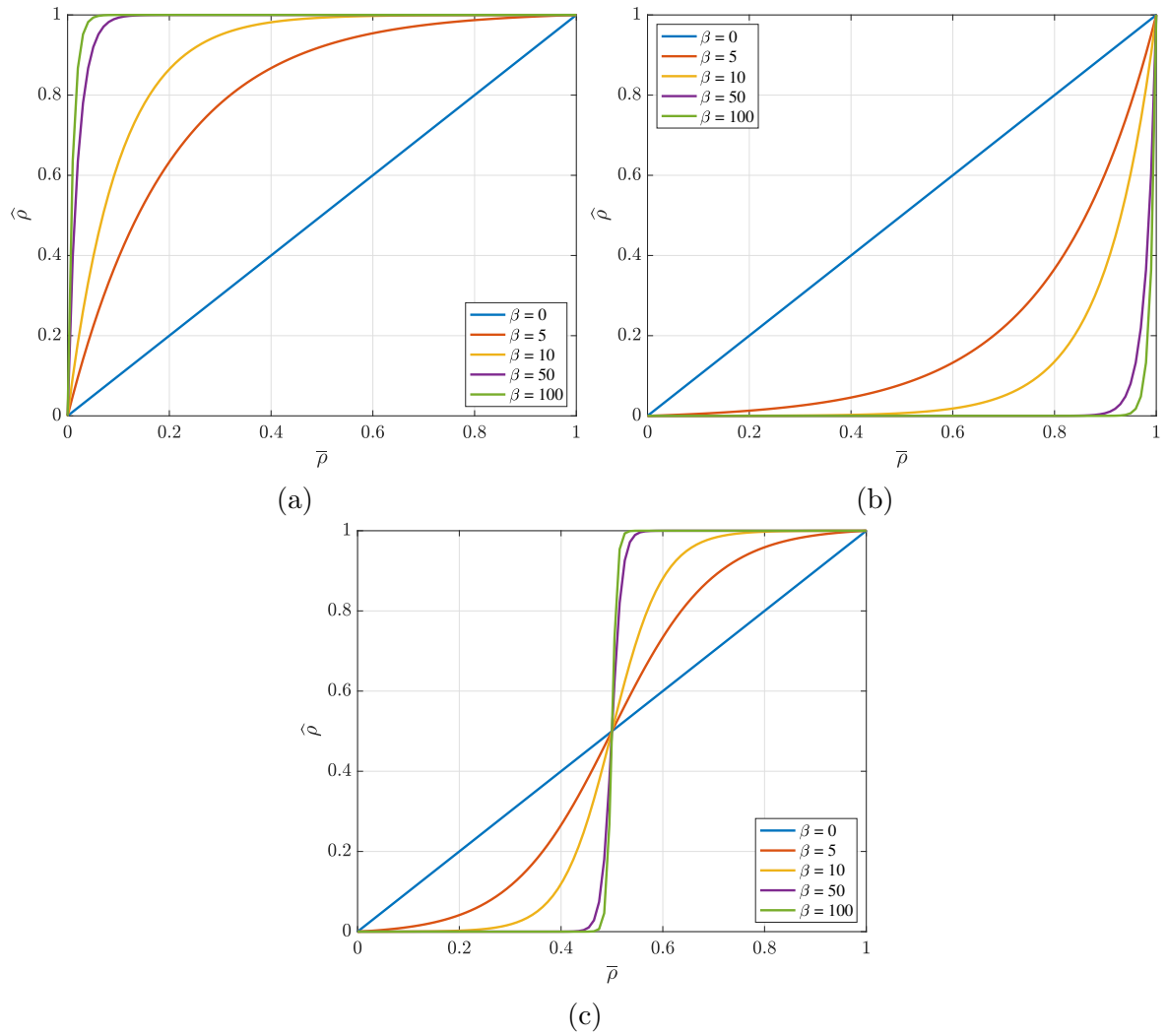


Figure 2.4: The projection of the pseudo-density through different formulations where $\eta = 0.5$ (a) Guest et al. (2004) (b) Sigmund (2007) (c) Xu et al. (2010)

(a))

$$\widehat{\rho} = 1 - e^{-\beta\overline{\rho}} + \overline{\rho}e^{-\beta} \tag{2.11}$$

to dilate the filtered intermediate pseudo-density to solid. In contrast, Sigmund (2007) addressed the issue through the erosion of the filtered intermediate pseudo-density as (see Fig. 2.4 (b))

$$\widehat{\rho} = e^{-\beta(1-\overline{\rho})} - (1 - \overline{\rho})e^{-\beta} \tag{2.12}$$

The dilation and erosion are achieved by gradually increasing the projection parameter, β, during the optimisation iterations. Later, Xu et al. (2010) combined Eq.(2.11) and Eq. (2.12)

as

$$\widehat{\rho} = \begin{cases} \eta \left[e^{-\beta(1-\overline{\rho}/\eta)} - (1-\overline{\rho}/\eta)e^{-\beta} \right] & 0 \leq \overline{\rho} < \eta \\ \eta & \overline{\rho} = \eta \\ (1-\eta)\left[1 - e^{-\beta(\overline{\rho}-\eta)/(1-\eta)} + (\overline{\rho}-\eta)e^{-\beta}/(1-\eta) \right] + \eta & \eta < \overline{\rho} \leq 1 \end{cases} \tag{2.13}$$

that allows volume preservation to avoid objective and volume oscillation during the optimisation (see Fig. 2.4c). A simplified version of Eq. (2.13) is presented in Wang et al. (2011) as

$$\widehat{\rho} = \frac{\tanh \beta\eta + \tanh \beta(\overline{\rho} - \eta)}{\tanh \beta\eta + \tanh \beta(1-\eta)} \tag{2.14}$$

It is important to note that the implementation of the projection scheme does not guarantee discrete designs if the intermediate regions are generated due to insufficient penalisation (Sigmund and Maute, 2013). To address this problem, continuation approaches that gradually increases the penalisation parameter and the projection parameter can be applied. Although the continuation of the projection parameter may significantly increase the optimisation iterations, the extensions of combining pseudo-density regularisation filters and projection schemes successfully results in discrete designs whilst alleviate checkerboard and mesh-dependent issues.

2.2 Fibre-reinforced Composites (FRCs) Optimisation

The design of FRCs typically involves two main categories: constant stiffness and variable stiffness design. In constant stiffness design, the design domain is treated as a single element with uniform material properties, whilst variable stiffness design allows for spatially varying material properties across multiple elements. Optimal designs of constant stiffness design often prioritise considerations such as stacking sequence, the number and thickness of layers, and fibre orientation in each layer (Ghiasi et al., 2009). Variable stiffness design particularly emphasises the variation of fibre orientation due to its significant impact on the anisotropic characteristics and consequent structural performance enhancements. Various optimisation approaches have been developed and documented in the literature to determine the optimal design of FRCs. Note that this work solely focuses on the design of variable stiffness composites, hence literature related to constant stiffness composites is not considered in the following review.

2.2.1 Optimality Criterion

Optimality criterion approaches establish a suitable criterion for specific design conditions and iteratively update the design to achieve optimal solutions (Rao, 2019). The strain-based approach proposed by Pedersen (1989) is one of the earliest approaches for fibre orientation optimisation, where energy density serves as the optimality criterion under the assumption of a uniform strain field. The design variable in this approach is the angle between the fibre orientation and the major principal strain direction, with a closed-form solution derived for optimal fibre orientation. Cheng et al. (1994) later incorporated a stress-based concept, inspired by Díaz and Bendsøe (1992), assuming a uniform stress field. These approaches have demonstrated significant improvements in structural performance, particularly in stiffness and buckling resistance, compared to single fibre orientation FRCs. However, challenges arise as the strain and stress fields are implicit functions of fibre orientation, contradicting the initial assumptions. Moreover, both strain-based and stress-based approaches may struggle to identify a unique optimal fibre orientation due to repeated global minima (Gea and Luo, 2004). An energy-based approach introduced by Luo and Gea (1998) addresses these issues by utilising an inclusion model to approximate the strain and stress fields, eliminating the assumptions of uniformity. This energy-based approach has shown faster convergence than the stress-based approach and greater robustness than the strain-based approach.

Subsequent studies by Pedersen (1990, 1991) showed that for shear-weak materials, the optimal fibre orientation coincides with the principal stress and strain directions. This discovery laid the foundation for the fibre-steering technique, which aims to align fibre orientation with the principal stress direction throughout the design domain. Hyer and Charette (1991) utilised the principal stress direction based on an isotropic material as the initial design for the fibre orientation. In each iteration, the fibre orientation is adjusted to align with the principal stress direction from the previous iteration. Whilst optimal results demonstrated enhanced stiffness and strength (Tosh and Kelly, 2001; Li et al., 2002), this approach results in sub-optimal when buckling resistance is critical (Hyer and Charette, 1991; Crothers et al., 1997). Tosh and Kelly (2000) introduced several approaches to enhance strength, such as adding additional plies in the orthogonal direction to the original plies, aligned with the first principal stress direction, and

utilising the principal stress direction of each loading case in different plies to address multiple loading conditions. To maximise strength, they also proposed aligning the fibre orientation with the load path instead of the principal stress direction.

2.2.2 Continuous Fibre Angle Optimisation

Continuous Fibre Angle Optimisation (CAFO) represents a direct approach utilising element-wise fibre orientation as design variables, which is similar to homogeneous topology optimisation but focusing solely on rotation (Suzuki and Kikuchi, 1991). Instead of using optimality criteria, some approaches update design variables directly from the sensitivities with respect to the objectives and constraints (Jørgensen, 1991; Geier and Zimmermann, 1994; Cho and Rowlands, 2009). Bruyneel and Fleury (2002) introduced sequential convex programming to approximate the objectives and constraints to ease the difficulty of implementing an optimisation problem. This method has been employed to optimise structural performance parameters such as stiffness and buckling resistance (Rion and Bruyneel, 2006; Lindgaard and Lund, 2010). However, a notable challenge with CAFO lies in its typically non-convex design space (Stegmann and Lund, 2005; Ghiasi et al., 2010), leading to the optimal design's dependence on the initial configuration (Bruyneel and Fleury, 2002). This phenomenon is also observed in optimality criterion approaches.

2.2.3 Discrete Material Optimisation

To alleviate the non-convex design space issue, Discrete Material Optimisation (DMO) is introduced by Stegmann and Lund (2005) which optimise the structural performance by selecting the fibre orientation for each element from a predefined set of candidates. This is achieved using a weighted sum of the candidate fibre orientations to represent the element-wise stiffness matrix. Penalisation is applied to encourage a selection of single fibre orientations for each element. The initial design is a fictitious multi-material design composed of different fibre orientations, resulting in less dependency on the initial configuration compared to CFAO (Sigmund and Torquato, 1997; Stegmann and Lund, 2005). A drawback of DMO is that the number of the predefined fibre orientations is limited to avoid the number of design variables from becoming

too large. Extensions of DMO, such as Shape Function with Penalsation (Bruyneel, 2011) and Bi-value Coding Parameterisation (Gao et al., 2012), address this limitation by using weighted formulations to reduce the number of design variables.

2.2.4 Lamination Parameters Parameterisation

An alternative approach to alleviate the non-convex design space issue is to optimise structure performance through lamination parameters (Hammer et al., 1997). Lamination parameters describe the in-plane and bending stiffness of a FRC which is thin and symmetric lay up. The use of lamination parameters implicitly describe the fibre orientation and the ply thickness so that the optimal design is less dependent on the initial configuration compared to CFAO Ghiasi et al. (2010). This approach has proven optimal performance characteristics on various structure performance such as stiffness, buckling resistance, fundamental frequency and flutter speed (Setoodeh et al., 2006a; Abdalla et al., 2007; Khani et al., 2011; Wu et al., 2014). However, it is difficult to determine the feasible region for the lamination parameters (Diaconu et al., 2012), and an extra optimisation problem is typically needed to determine the element-wise FRC configuration from the optimised lamination parameters (van Campen et al., 2012).

2.2.5 Heuristic Approaches

Applying heuristic approaches is another alternative to alleviate the non-convex design space issue. Setoodeh et al. (2006b, 2009) use local optimality criteria and cellular automata to optimise the fibre orientation. Genetic algorithms have also been applied to achieve designs close to the global optimum (Kim et al., 1999; Liu and Haftka, 2001; Antonio, 2006; Keller, 2010; Zabinsky et al., 2006). Although the designs demonstrated in the literature are close to the global optimum, drawbacks such as high computational cost due to the large number of design variables and the lack of global convergence criteria are observed.

2.2.6 Curvilinear Parameterisation

Curvilinear parameterisation applies a curvilinear function to describe the fibre path, which ensures the continuity and connectivity of the element-wise fibre orientation (Parnas et al.,

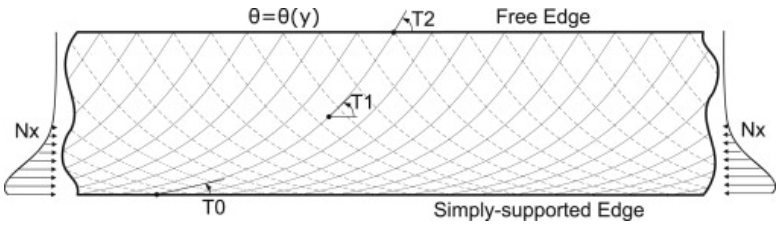


Figure 2.5: The curvilinear parameterisation example presented in Wu et al. (2012) shows three locations, T_0, T_1 and T_2, define the fibre orientation that enables the continuous fibre path

2003; Wu, 2008; Gürdal et al., 2008). Achieving the continuity and connectivity of the fibre path typically requires additional interpretation or constraints for approaches that describe the fibre orientation elementally. The design variables for this approach typically involve parameters to describe the curvilinear function at selected locations, which helps reduce the number of design variables compared to approaches that describe the fibre orientation elementally (see Fig. 2.5). The reduction in the number of design variables allows effective utilisation of evolutionary or graphical approaches to achieve optimality (Huang and Haftka, 2005; Sun and Hyer, 2012; Wu et al., 2012). However, the potential of the curvilinear parameterisation may be limited due to the restricted design space (Ghiasi et al., 2010).

2.3 Topology and Fibre Orientation Optimisation

The combination of topology and fibre orientation optimisation initially focused on optimising the thickness and fibre orientation of laminate panels (Pedersen, 1991; Parnas et al., 2003). As AM technology advanced, the entire structural layout has been considered in recent studies. Various TO approaches such as the cellular automata (Setoodeh et al., 2005), density-based approaches (Rion and Bruyneel, 2006; Li and Atluri, 2008; Hvejsel and Lund, 2011; Caivano et al., 2020), and LSM (Papapetrou et al., 2020) are used to determine the structure layout.

To achieve a smooth variation of fibre orientation, Schmidt et al. (2020) applied the weighted averages approach to regularise the fibre orientation. The equivalent Helmholtz filter is also applied in other studies (Nomura et al., 2015; Lee et al., 2018; Jantos et al., 2020). A drawback in CFAO that stems from the periodic angular representation, for example, when the fibre orientation is equal to 0 and 2π, is avoided by using Cartesian components to represent the fibre orientation (Nomura et al., 2015). This also leads to an optimal design that is less

dependant on the initial configuration. However, singular point and potential "gimbal lock" issues were found in the fibre orientation rotation achieved by coordinate transformation when extending to 3D. Subsequent studies by Nomura et al. (2019); Jung et al. (2022) applied tensor representation to alleviate these issues.

To fabricate optimal designs, the fibre orientation needs to be interpreted as a fibre path that allows AM machines to deposit bundles composed of fibre and matrix. Brampton et al. (2015) applied an LSF to describe the equal spacing fibre path which ensures the manufacturability of laminate composites using the automated fibre placement technique. Nomura et al. (2015) adopted a TO method using isoparametric projection to generate continuous and discrete fibre orientation design. Papapetrou et al. (2020) demonstrated three infill methods—the equal space method, the streamline method and the offset method— to interpret the fibre path. However, the results from Brampton et al. (2015) and the offset method in Papapetrou et al. (2020) show sharp turns in the fibre path, and the results from Nomura et al. (2015) and Papapetrou et al. (2020) show varying distances between the fibre path which potentially lead to the generation of voids. The sharp turns at the fibre path result in high curvature of the deposited fibres which may cause twisting and folding back of the fibres (Matsuzaki et al., 2018) and the voids result in decreasing the fibre volume fraction. As a result, these may degrade the mechanical properties of the FRCs, and the neglected reduction of the fibre volume fraction may lead to a loss of modelling accuracy.

Schmidt et al. (2020) presented an approach which shows the ability to solve large-scale and multiple load optimisation problems. Despite the fact that the optimised GE bracket (GrabCAD, 2013; Whalen et al., 2021) in their work achieved by the streamline method shows a smoothly varying fibre orientation which solves the problem of the sharp turns, varying dis-

Table 2.1: Summary of common fabrication issues found in optimised designs

Common issue	Consequence	Study	Fibre path
Sharp fibre turns	Twisted and folded fibres	Brampton et al. (2015) Papapetrou et al. (2020)	Level-set function Off-set method
Gaps between fibre path	Voids	Nomura et al. (2015) Papapetrou et al. (2020) Schmidt et al. (2020)	Streamlines

tances between the fibre paths can still be observed. This illustrates that the fibre volume fraction variation corresponding to the varying distances could not be account for. It is difficult to extract sufficient information such as layer height and printing width, from the three dimensional streamlines to slicing software before printing. The sharp turns and the varying distances illustrate the challenges of including manufacturability in the optimisation process. Common fabrication issues observed in optimisation results from previous studies are summarised in Tab. 2.1.

2.4 Manufacturing

Traditional manufacturing approaches for FRCs include wet layup, filament winding, or compression moulding, which are complex and labour-demanding. An innovation in composite manufacturing is the fabrication of variable stiffness composites. Tailored Fibre Placement (TFP) is a technique used to fabricate variable stiffness composites by placing a dry fibre roving at the desired position using a stitching yarn (Matveev et al., 2016). Automatic Fibre Placement (AFP) integrates tape laying and filament winding to enable the fabrication of large-scale variable stiffness composites by concurrently placing a large number of fibre tows. Due to the wide fibre tows, gaps and overlaps are often generated during fabrication (Aragh et al., 2021). Continuous Tow Shearing (CTS) applies in-situ impregnation of fibre and resin and constantly imposes shear deformation during deposition, allowing the width and height of the deposited tows to be flexible. This leads to better ability to steer fibres without generating gaps and overlaps (Aragh et al., 2021).

As manufacturing technology advances, 3D printers using filament deposition modelling (FDM) enable the deposition of filament on a smaller scale and with greater precision. Furthermore, robotic arm 3D printers enable out-of-plane printing, which expands the design space for fibre orientation to truly vary in 3D. The fibre impregnation process directly affects the fibre volume fraction. Controlling and increasing the fibre volume fraction over 50% is a challenge (Liu et al., 2020). By pre-impregnating fibres within a matrix, the fibre volume fraction can be enhanced and the quality of impregnation can also be improved (Dickson et al., 2020). However, the fibre volume fraction is not adjustable during the deposition process. One potential method of

manufacturing varying fibre volume fraction composites is using in-situ impregnation. Recently, Pelzer and Hopmann (2021) have presented an algorithm for non-planar path planning with variable layer height. The variable layer height is achieved by adjusting the amount of extruded material. Adapting this concept to in-situ impregnation and assuming the fibres are perfectly impregnated, as the amount of the extruded matrix varies whilst the amount of the fibre stays constant, the fibre volume fraction will have a respective variation. The assumed integration shows the potential manufacturability of fabricating FRCs with varying fibre volume fraction.

2.5 Optimisation with Buckling Resistance

To account for buckling resistance during the optimisation process, stability analysis is necessary to obtain the buckling characteristics. Linear buckling analysis is commonly applied in TO (Ferrari and Sigmund, 2020, 2023; Xu et al., 2023), although there may be over- or underestimation of critical buckling load factor due to the geometrical nonlinearity inherent in buckling (Dunning, 2023). In contrast, nonlinear buckling analysis is able to compute critical buckling load factors more accurately (Pedersen and Pedersen, 2018; Dalklint et al., 2021); however, it has received less attention likely due to the expensive computational cost of nonlinear solution.

Challenges such as mode switching and spurious modes are commonly encountered when incorporating buckling into TO. Mode switching is a common phenomenon observed in eigenvalue-type optimisation problems due to the order of the eigenvectors changing. This phenomenon is detrimental to gradient-based optimisation approaches since the sequence of the considered eigenvalues and the corresponding sensitivities used by the optimiser are not consistent. This issue is typically addressed by considering multiple buckling modes. It can be achieved by directly using multiple constraints or employing aggregation formulations to represent the multiple buckling modes (Dunning et al., 2016; Ferrari and Sigmund, 2019). Bruyneel et al. (2007); Dunning et al. (2016) have shown that considering more than 10 buckling modes during the optimisation process is able to avoid the effect of mode switching and generate smooth convergence.

The occurrence of spurious modes presents a considerable challenge when optimising for buckling at low pseudo-density areas, where strain energy is predicted to be too low compared to

total strain energy, has gathered attention from several studies. Neves et al. (1995) proposed a cutoff on the contribution of geometrical nonlinearity in the low density regions. Bendsøe and Sigmund (2004) introduced a different interpolation scheme on the stiffness matrix and the geometric stiffness matrix. Gao and Ma (2015) noted that the decision regarding the stiffness of void elements would impact on the occurrence of the spurious modes and proposed a spurious modes identification approach to track on the physical buckling modes. This issue is also identified in nonlinear buckling analysis, where Dalklint et al. (2021) uses energy transition strategy proposed by Wang et al. (2014) to alleviate the occurrence of the spurious modes. Recently, spurious modes at high pseudo-density areas (solid) where the magnitude of stresses fluctuates severely has been identified and effectively avoided using a regularisation of the stress components (Ferrari and Sigmund, 2023).

2.6 Summary

This chapter provides a review of structural optimisation, focusing solely on TO within the category of structural optimisation. Among the TO approaches reviewed, SIMP is deemed more suitable for the objective of this thesis due to its characteristics such as easy implementation, efficient converging behaviour, and robustness in reaching global optimality. For the optimisation of fibre orientation, CFAO using Cartesian components representation with a fibre orientation filter has shown great ability to achieve global optimality whilst keeping the design space flexible for the implementation of manufacturing constraints. Hence, the developed optimisation framework will be based on the combination of SIMP and CFAO to achieve optimal designs for both topology and fibre orientation.

Several manufacturing issues have been identified, including the sharp fibre turns, neglected consideration of fibre volume fraction, and additional post-processing efforts required to interpret fibre paths. Additionally, the potential manufacturability, facilitated by the assumed integration of in-situ impregnation and non-planar path planning, motivates the objective of developing novel manufacturing constraints to achieve 3D printed FRCs.

The review of stability issues commonly seen in topologically optimised structures raises the objective of improving buckling resistance. Although challenges have been identified in the

incorporation of buckling resistance within TO frameworks, improving buckling resistance can bring optimal designs closer to real-world applications.

Chapter 3

Topology and Fibre Orientation Optimisation Framework

This chapter describes the methodology of the topology and fibre orientation optimisation framework developed in this thesis. It establishes the constitutive law of the framework, followed by detailing the microscale model, the optimisation formulation and the manufacturing constraints.

3.1 Constitutive Law

The constitutive law of the framework is within the theory of linear elasticity. The equation of equilibrium is described as

$$\frac{\partial \sigma_{ij}}{\partial x_j} + F_i = 0 \tag{3.1}$$

where σ_{ij} denotes the Cauchy stress tensor, F_i denotes the body force on the design domain, and i, j represent the coordinate axes. The strain is assumed to be infinitesimal and the relationship between stress and strain is linear such that

$$\begin{aligned} \sigma_{ij} &= E_{ijkl}\epsilon_{kl} \\ \epsilon_{ij} &= \frac{1}{2}\left(\frac{\partial u_i}{\partial x_j} + \frac{\partial u_j}{\partial x_i}\right) \end{aligned} \tag{3.2}$$

where E_{ijkl} denotes the elasticity tensor, ϵ_{ij} denotes the strain tensor and u_i, u_j denote the displacement.

3.2 Microscale Model

The microscale model is a unidirectional fibre-reinforced composite which can be oriented in three dimensional space. To describe the mechanical properties of the microscale model, the material properties interpretation of the unidirectional fibre-reinforced composites and the rotation function are derived.

3.2.1 Material Properties

There are different approaches to obtain the mechanical properties of unidirectional fibre-reinforced composites, such as the well-known rule of mixtures, the Eshelby equivalent homogeneous inclusion approach and the approach of using representative volume elements modelled using the finite elements method (Clyne and Hull, 2019). For simplicity, the rule of mixtures using the slab model under the assumption of equal stress and equal strain is applied to evaluate the elasticity characteristics as

$$\begin{aligned} E_{1111} = E_F &= E_f V_f + E_m V_m \\ E_{2222} = E_{3333} = E_T &= \frac{1}{\frac{V_f}{E_f} + \frac{V_m}{E_m}} \end{aligned} \tag{3.3}$$

where E denotes Young's modulus, V denotes the volume fraction, subscripts 1 and F denote the fibre direction, subscripts 2, 3 and T denote transverse directions, and subscripts f, m denote fibre and matrix respectively. To capture the variation of the fibre volume fraction during optimisation, the fibre volume fraction is chosen to be one of the optimisation variables. Substituting Eq. (3.3) to the elasticity tensor and rewriting it as a second order tensor gives

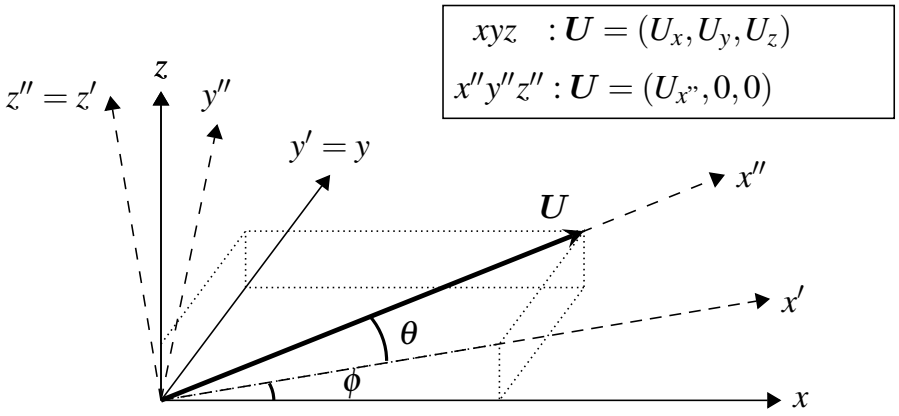


Figure 3.1: The fibre orientation vector $\boldsymbol{U}$ is defined as (U_x, U_y, U_z) in the coordinate system xyz and it can be written as $(U_{x''}, 0, 0)$ in the coordinate system $x''y''z''$. The local coordinate system, $x''y''z''$, is rotated about the z'' axis through an angle θ which results in a transit coordinate system $x'y'z'$. The transition coordinate system is then rotated about the y' axis through an angle ϕ which results in the global coordinate system xyz

the stiffness matrix of the microscale model

$$\boldsymbol{K}_e^0(V_f) = \begin{bmatrix} \frac{1}{E_F} & -\frac{\nu_F}{E_F} & -\frac{\nu_F}{E_F} & 0 & 0 & 0 \\ -\frac{\nu_F}{E_F} & \frac{1}{E_T} & -\frac{\nu_T}{E_T} & 0 & 0 & 0 \\ -\frac{\nu_F}{E_F} & -\frac{\nu_T}{E_T} & \frac{1}{E_T} & 0 & 0 & 0 \\ 0 & 0 & 0 & \frac{1}{G_T} & 0 & 0 \\ 0 & 0 & 0 & 0 & \frac{1}{G_F} & 0 \\ 0 & 0 & 0 & 0 & 0 & \frac{1}{G_F} \end{bmatrix}^{-1} \tag{3.4}$$

3.2.2 Rotation Function

The fibre orientation is defined as a vector, $\boldsymbol{U} = (U_x, U_y, U_z)$. To evaluate the stiffness matrix of the microscale model with the fibre orientation $\boldsymbol{U}$, which is not aligned with the x axis, a local coordinate system, $x''y''z''$, in which the fibre orientation vector $\boldsymbol{U}$ can be written as $(U_{x''}, 0, 0)$, is introduced. In the $x''y''z''$ coordinate system, the stiffness matrix can easily be evaluated by Eq. (3.4). By transforming the local coordinate system twice, the stiffness matrix corresponding to the global coordinate system, xyz, can be evaluated. The coordinate system transformation illustrated in Fig. 3.1 is achieved by rotating the local coordinate system, $x''y''z''$, about the z'' axis and then rotating the transit coordinate system, $x'y'z'$, about the y' axis. The rotation

angles, θ and ϕ, can be written in terms of the components of $\boldsymbol{U}$ as

$$\begin{aligned}\theta &= \cos^{-1}\frac{\sqrt{U_x^2+U_z^2}}{\sqrt{U_x^2+U_y^2+U_z^2}}\\ \phi &= \cos^{-1}\frac{U_x}{\sqrt{U_x^2+U_z^2}}\end{aligned} \tag{3.5}$$

The stiffness matrix after first coordinate transformation can be written as $\boldsymbol{K} = \boldsymbol{T}\boldsymbol{K}^0\boldsymbol{T}^T$ where $\boldsymbol{T}$ is the transformation matrix (Clyne and Hull, 2019). Hence, the stiffness matrix of the microscale model after second coordinate transformation can be written as a function of the fibre volume fraction and the fibre orientation vector as

$$\boldsymbol{K}_e(V_f, \boldsymbol{U}) = \boldsymbol{T}_2[\boldsymbol{T}_1\boldsymbol{K}_e^0(V_f)\boldsymbol{T}_1^T]\boldsymbol{T}_2^T \tag{3.6}$$

where

$$\boldsymbol{T}_1 = \begin{bmatrix} \cos^2\theta & \sin^2\theta & 0 & 0 & 0 & -2\sin\theta\cos\theta \\ \sin^2\theta & \cos^2\theta & 0 & 0 & 0 & 2\sin\theta\cos\theta \\ 0 & 0 & 1 & 0 & 0 & 0 \\ 0 & 0 & 0 & \cos\theta & \sin\theta & 0 \\ 0 & 0 & 0 & -\sin\theta & \cos\theta & 0 \\ \sin\theta\cos\theta & -\sin\theta\cos\theta & 0 & 0 & 0 & \cos^2\theta-\sin^2\theta \end{bmatrix}$$

$$\boldsymbol{T}_2 = \begin{bmatrix} \cos^2\phi & 0 & \sin^2\phi & 0 & -2\sin\phi\cos\phi & 0 \\ 0 & 1 & 0 & 0 & 0 & 0 \\ \sin^2\phi & 0 & \cos^2\phi & 0 & 2\sin\phi\cos\phi & 0 \\ 0 & 0 & 0 & \cos\phi & 0 & \sin\phi \\ \sin\phi\cos\phi & 0 & -\sin\phi\cos\phi & 0 & \cos^2\phi-\sin^2\phi & 0 \\ 0 & 0 & 0 & -\sin\phi & 0 & \cos\phi \end{bmatrix}$$

Note that to ensure the vector represents a unique fibre orientation, the fibre orientation vector is constrained to be a unit vector, $\|\boldsymbol{U}\| = 1$, and the 2π ambiguity commonly seen in CFAO (Nomura et al., 2015) is avoided by evaluating sin and cos functions, Eq. (3.5), directly using the component of the fibre orientation vector. However, approaches using coordinate rotations

inevitably face a singular point problem. In this study, a potential singular point exists where the fibre orientation vector is aligned with the y axis, (0,1,0). This might raise a numerical instability issue of zero division in Eq. (3.5), and lead to a loss of sensitivity information with respect to the second rotation at this point. With a continuity constraint introduced in Secs. 3.4.1, the singular point problem is not encountered in the numerical examples demonstrated in this study. Readers are referred to Nomura et al. (2019) for a singular point free fibre orientation representation.

Microscale Model in 2D

In order to provide a clearer demonstration for cases and concepts, the microscale model simplified for 2D in xy plane is derived here as

$$\boldsymbol{K}_e(V_f, \boldsymbol{U}) = \boldsymbol{T}\boldsymbol{K}_e^0(V_f)\boldsymbol{T}^T \tag{3.7}$$

where only one coordinate transformation is needed

$$\boldsymbol{T} = \begin{bmatrix} \cos^2\theta & \sin^2\theta & -2\sin\theta\cos\theta \\ \sin^2\theta & \cos^2\theta & 2\sin\theta\cos\theta \\ \sin\theta\cos\theta & -\sin\theta\cos\theta & \cos^2\theta - \sin^2\theta \end{bmatrix} \tag{3.8}$$

and θ is determined as

$$\theta = \cos^{-1}\frac{U_x}{\sqrt{U_x^2 + U_y^2}} \tag{3.9}$$

given that $U_z = 0$.

3.3 Topology Optimisation

In order to gain a better performance through achieving lightweighting designs and optimised fibre orientation, topology optimisation is applied to combine with the microscale model. The most widely used density-based approach, SIMP, is applied in this framework to describe the topology. Parameter, p, is used to penalise the local material stiffness matrix as

$$\widehat{\boldsymbol{K}}_e(\rho, V_f, \boldsymbol{U}) = [\rho_{min} + (1 - \rho_{min})\rho^p]\boldsymbol{K}_e(V_f, \boldsymbol{U}) \tag{3.10}$$

where ρ is a dimensionless pseudo-density which provides a continuous interpretation of the existence of materials and ρ_{min} is a small number to ensure the stiffness matrix is positive definite.

Combining the penalisation with the microscale model, the pseudo-density, the fibre volume fraction and the fibre orientation can be subjected to different objective optimisation problems.

3.4 Manufacturing Constraints

The manufacturing issues discussed in Chapter 2 include sharp fibre turns, the degradation of mechanical properties and the loss of modelling accuracy due to the neglected reduction of the fibre volume fraction, and the difficulty of extracting sufficient information for slicing software from streamlines during post-processing of the optimisation results. As mentioned in Section 2.4, a potential manufacturing approach based on adjusting the amount of extruded matrix, which enables variable layer height printing, has been noted. By using in-situ impregnation and assuming the fibres are perfectly impregnated, the fibre volume fraction will vary correspondingly as the amount of extruded matrix changes while the amount of fibre remains constant. Continuity constraints and fibre path generation constraints are introduced to circumvent the corresponding issues based on the potential manufacturing approach.

3.4.1 Continuity Constraints

To overcome the manufacturing issue with regard to the fibre volume fraction and to keep the fibre orientation continuous, a continuity constraint is applied to ensure conservation of fibre mass in a control volume such that

$$\nabla \cdot \frac{\rho_F V_F}{V} \boldsymbol{U} = 0 \tag{3.11}$$

where $\rho_F V_F$ denotes the fibre mass within an element and V denotes the volume of the element. Equation (3.11) illustrates that the mass which enters and leaves the control volume is the same which is analogous to the continuity equation for the case of a steady state fluid. Note that in

order to avoid the magnitude of the fibre orientation vector involving in the mass variation, it is constrained to a unit vector. Removing the density of the fibre from the divergence operator since it is a constant and replacing the fraction of the fibre volume and the element volume by the fibre volume fraction gives the equation of the continuity constraint as

$$\nabla \cdot V_f \boldsymbol{U} = 0 \tag{3.12}$$

3.4.2 Fibre Path Generation Constraints

The fibre path generation constraints are inspired by field-based toolpath generation methods which ensure the gradient of the scalar field is orthogonal to the deposition direction to generate toolpaths (Fang et al., 2020; Chen et al., 2022). Here, the fibre path needs to be aligned with the fibre orientation vector to be consistent with the modelling result. By introducing two scalar fields , S_1 and S_2, as additional design variables and constraining the cross product of their gradients to be equal to the fibre orientation vector as

$$\nabla S_1 \times \nabla S_2 = \boldsymbol{U} \tag{3.13}$$

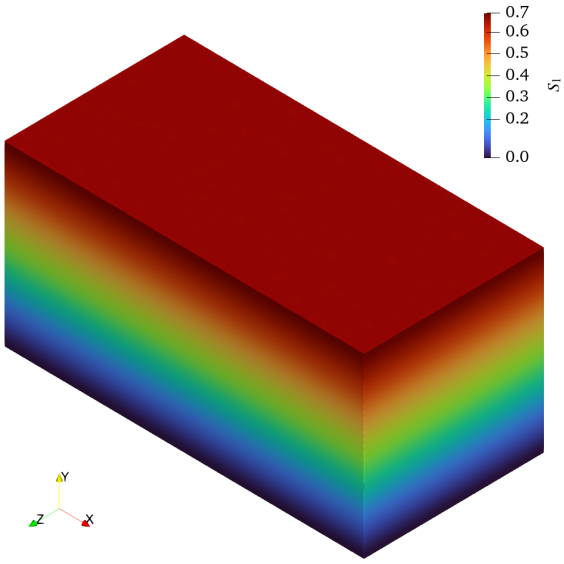
the fibre orientation vector $\boldsymbol{U}$ is orthogonal to ∇S_1 and ∇S_2 due to the orthogonality of cross products. In other words, the fibre orientation vector lies in the isosurfaces of both S_1 and S_2. Hence, by extracting the intersection curves of the isosurfaces, the fibre path is generated. An example is presented in Fig. 3.2 to illustrate the generation of the fibre path.

The variation of the fibre volume fraction needs to be considered in the fibre path generation. By scaling the fibre orientation vector $\boldsymbol{U}$ to $V_f\boldsymbol{U}$ and rewriting Eq. (3.13) as

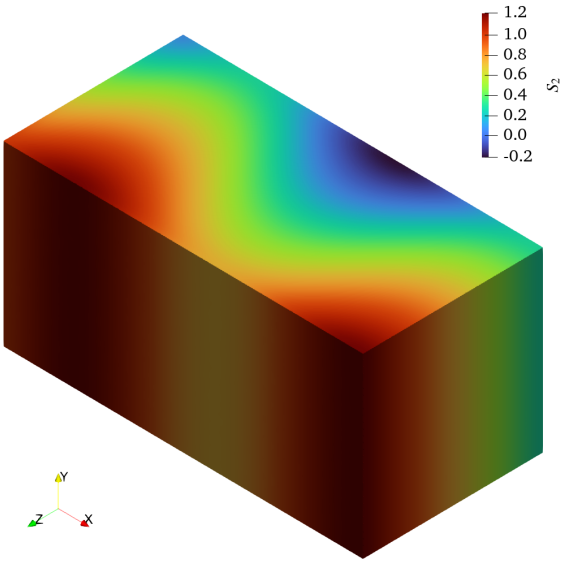
$$\nabla S_1 \times \nabla S_2 = V_f \boldsymbol{U} \tag{3.14}$$

the cross product of ∇S_1 and ∇S_2 is also able to describe the fibre volume fraction. The magnitude form of Eq. (3.14) can be written as

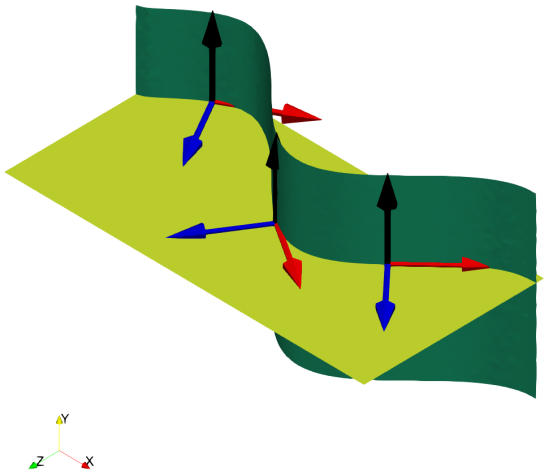
$$\|\nabla S_1\| \|\nabla S_2\| \sin\alpha = V_f \|\boldsymbol{U}\| \tag{3.15}$$



(a) $S_1 = y$



(b) $S_2 = 0.5 \sin 4x + z$



(c) The isosurfaces at $S_1 = 0.4$ and $S_2 = 0.3$



(d) The fibre path

Figure 3.2: Two scalar fields, $S_1 = y$ and $S_2 = 0.5 \sin 4x + z$, defined over a cuboid domain of size $2 \times 1 \times 1$ shown in (a) and (b), respectively, are used as an example. Isosurfaces are extracted at $S_1 = 0.4$ and $S_2 = 0.3$, and three locations ($x = \{0.25, 1, 1.75\}$) are selected to illustrate the fibre path generation. The arrows at these three locations denote ∇S_1 (black), ∇S_2 (blue) and $\nabla S_1 \times \nabla S_2$ (red). The fibre orientation aligns with intersection curve of the isosurfaces shown in (d) when $\nabla S_1 \times \nabla S_2$ is equal to $\boldsymbol{U}$, so that the intersection curve can be used to interpret the element-wise fibre orientation into continuous fibre path

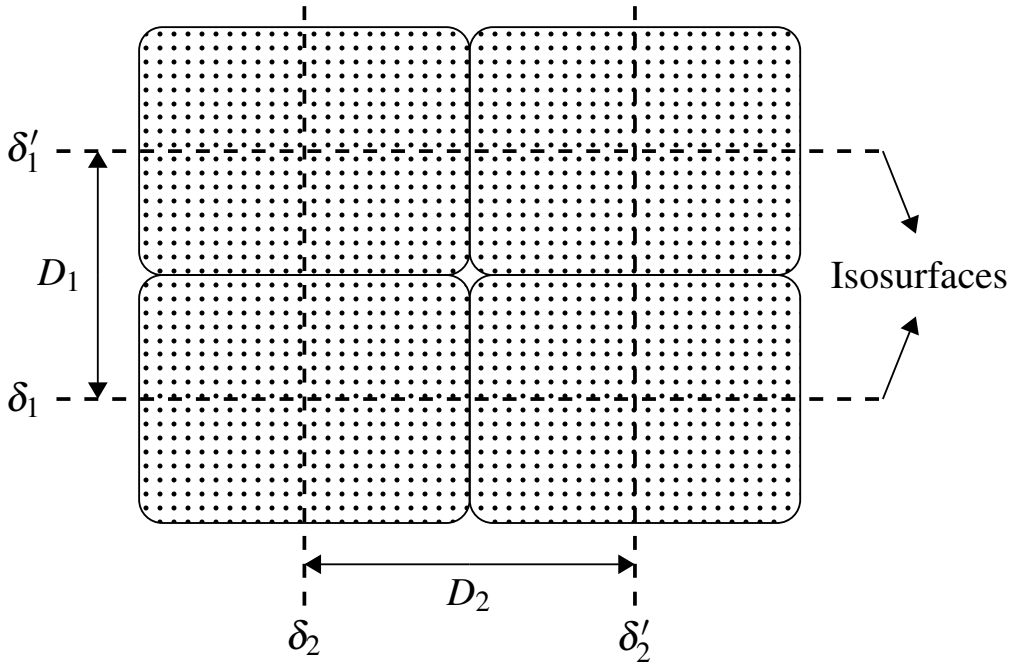


Figure 3.3: The cross section of deposited fibre bundles shows the aspect ratio of the bundles is controlled by the distances between isosurfaces, D_1 and D_2

where α is the angle between the gradients. To eliminate the influence of the varying angle, the gradients are constrained to be orthogonal by requiring

$$\nabla S_1 \cdot \nabla S_2 = 0 \tag{3.16}$$

Since $\sin\alpha$ becomes unitary due to the orthogonality constraint, Eq. (3.16), the product of the magnitudes of the gradients in Eq. (3.15) is equal to the fibre volume fraction. Specifically, the fibre volume fraction is interpreted by the magnitudes of the gradients. Fig. 3.3 shows the cross section of deposited fibre bundles where dashed lines denote the isosurfaces, subscripts 1 and 2 denote the value corresponding to S_1 or S_2 respectively, δ and δ' denote the scalar value of the isosurface and D denotes the distance between the isosurfaces. Assuming the voids are negligible, the fibre volume fraction can be derived as

$$V_f = \frac{n\pi r_f^2}{D_1 D_2} \tag{3.17}$$

where n denotes the number of fibres within a deposited bundle and r_f denotes the radius of a single strand of fibre. To extract the isosurfaces evenly, the segment values $\Delta\delta$ used to extract

isosurfaces should be the same such that

$$\Delta\delta = \delta_1' - \delta_1 = \delta_2' - \delta_2 \tag{3.18}$$

Equation (3.18) can be written as

$$\Delta\delta = \|\nabla S_1\| D_1 = \|\nabla S_2\| D_2 \tag{3.19}$$

Moving D_2 to the left hand side gives

$$\frac{D_1}{D_2} = \left\| \frac{\nabla S_2}{\nabla S_1} \right\| \tag{3.20}$$

The distances between isosurfaces can be evaluated by solving Eq. (3.17) and Eq. (3.19) such that

$$\begin{aligned} D_1 &= \sqrt{\frac{n\pi r_f^2}{V_f} \left\| \frac{\nabla S_2}{\nabla S_1} \right\|} \\ D_2 &= \sqrt{\frac{n\pi r_f^2}{V_f} \left\| \frac{\nabla S_1}{\nabla S_2} \right\|} \end{aligned} \tag{3.21}$$

Equation (3.20) illustrates the aspect ratios of the deposited bundles are controlled by the ratio of the gradients. In reality, the aspect ratio of deposited fibre bundles is restricted by the nozzle geometry and the pressure in the print head. Zelinski (2022) reported an approach applying a variable width rectangular nozzle and controlling the amount of deposited matrix to decouple the link of layer height and printing width. The magnitude of the gradients can be used to control the aspect ratio in the future when the rectangular nozzle is applied to the continuous fibre filament deposition modelling such as

$$\left\| \frac{\nabla S_1}{\nabla S_2} \right\| - AR = 0 \tag{3.22}$$

Fibre Path Generation in 2D

In 2D, only one scalar field is required since the fibre orientation lies in 2D plane. Assuming the fibre orientation is solely permitted to vary in the xy plane, the gradient of the second scalar field is equal to the z axis, (0,0,1), as a constant. Under this assumption, Eq. (3.14) can be rewritten as

$$\nabla S \times (0, 0, 1) = V_f \boldsymbol{U} \tag{3.23}$$

After vector operation, the fibre path generation constraint in 2D is written as

$$\begin{aligned} \nabla S &= (0, 0, 1) \times V_f \boldsymbol{U} \\ &= V_f \boldsymbol{U'} \end{aligned} \tag{3.24}$$

where $\boldsymbol{U'}$ can be evaluated using the components of the orientation vector as $(-U_y, U_x)$. The orthogonality criterion is naturally met because the gradient of the scalar field will always be orthogonal to the fibre orientation and z axis due to the rule of cross products. The aspect ratio is now neglected since the physical meaning of fibre volume fraction is directly transferred to the magnitude of the gradient of the scalar field.

3.5 Optimisation Formulation

In this chapter, the optimisation formulation for a traditional structural optimisation problem, minimum compliance subject to volume constraint, is described. The mechanical properties of the model are controlled by the fibre volume fraction, fibre orientation and pseudo-density, and the fibre path is described using the two scalar fields. By parameterising them as design variables, optimal designs can be achieved.

3.5.1 Variable Filter

In order to avoid potential checkerboard issues, the design variables are passed through a Helmholtz-type filter (Lazarov and Sigmund, 2011) prior to evaluate the mechanical properties such that

$$-r_h^2 \nabla^2 \overline{\chi} + \overline{\chi} = \chi \tag{3.25}$$

where χ denotes the set of the design variables, $\{\rho, V_f, \boldsymbol{U}, S_1, S_2\}$, r_h denotes the filter radius and $\overline{\chi}$ denotes the set of filtered design variables, $\{\overline{\rho}, \overline{V_f}, \overline{\boldsymbol{U}}, \overline{S_1}, \overline{S_2}\}$. By solving the partial differential equation, the filtered design variables are used to evaluate the rest of the optimisation problem. In order to avoid the boundary effect discussed in Clausen and Andreassen (2017), the boundary condition used to solve the filtered pseudo-density is the Robin boundary condition, which is consistent with the physical padding techniques (Wallin et al., 2020). The rest of the filtered design variables are solved using homogeneous Neumann boundary condition.

3.5.2 Constraints formulations

In order to ensure the manufacturability, the filtered scalar fields, $\overline{S_1}$ and $\overline{S_2}$, the continuity constraints, Eq. (3.12), and the fibre path generation constraints, Eq. (3.14), Eq. (3.16) and Eq. (3.22), are introduced to limit the variation of the parameters. Note that the implementation of multiple constraints may significantly narrow the design space, increasing the likelihood of the optimisation process falling into a local minimum. Employing a lamination parameters parameterisation approach could potentially mitigate this issue; however, as discussed in Section 2.2.4, an additional optimisation step is required to determine the element-wise FRC configuration. In this work, the constraints are implemented as inequality constraints, even though their original formulations are equality constraints, to address this issue. Implementing inequality constraints generally provides greater flexibility in managing constraint violations, making it easier for the optimisation process to identify a feasible design space.

By integrating the local constraint functional and implementing them as inequality constraints, the continuity constraints and the fibre path generation constraints can be written in two sets, C_1 and C_2, as

$$C_1 = \begin{cases} \displaystyle\int_\Omega \overline{\rho}(\nabla \cdot \overline{V_f \boldsymbol{U}})^2 dx \leq 0 \\ \displaystyle\int_\Omega \overline{\rho}(\|\overline{\boldsymbol{U}}\| - 1)^2 dx \leq 0 \end{cases} \tag{3.26}$$

$$C_2 = \begin{cases} \begin{cases} \int_\Omega \overline{\rho}(\nabla\overline{S_1} \times \nabla\overline{S_2} - \overline{V_f \boldsymbol{U}})^2 dx \leq 0 \\ \int_\Omega \overline{\rho}(\nabla\overline{S_1} \cdot \nabla\overline{S_2})^2 dx \leq 0 \\ \int_\Omega \overline{\rho}\left(\left\|\dfrac{\nabla\overline{S_1}}{\nabla\overline{S_2}}\right\| - AR\right)^2 dx \leq 0 \end{cases} & \text{In 3D} \\ \int_\Omega \overline{\rho}(\nabla\overline{S} - \overline{V_f \boldsymbol{U'}})^2 dx \leq 0 & \text{In 2D} \end{cases} \tag{3.27}$$

where Ω denotes the design domain. Note that all constraints are scaled by the filtered pseudo-density $\overline{\rho}$, which means constraints are only considered when material is present. It is also important to note that in this framework, the aspect ratio in Eq. (3.27) is constrained to 1 to satisfy the manufacturability requirement of current processes.

3.5.3 Sensitivity analysis

The finite element analysis and the evaluation of all constraints are implemented using the open-source Python library, FEniCS (Alnaes et al., 2015). The sensitivities are then solved using an automatic differentiation method performed by the compatible Python library, dolfin-adjoint (Mitusch et al., 2019).

As the implementation of the variable filter, a chain rule corresponding to the filter is applied to evaluate sensitivities with regards to the original design variables as

$$\frac{\partial}{\partial \chi} = \frac{\partial}{\partial \overline{\chi}} \frac{\partial \overline{\chi}}{\chi} \tag{3.28}$$

3.5.4 Optimisation formulation

The optimisation formulation with manufacturing constraints are written as

$$\begin{aligned} \min_{V_f, \boldsymbol{U}, \rho, S_1, S_2} \quad & J(V_f, \boldsymbol{U}, \rho) = \int_\Gamma \boldsymbol{f} \cdot \boldsymbol{u} dx \\ s.t. \quad & \boldsymbol{f} = \boldsymbol{K} \cdot \boldsymbol{u} \\ & g_v = \int_\Omega \overline{\rho} dx - V_0 \leq 0 \\ & C_1 \quad \text{Eq. (3.26)} \\ & C_2 \quad \text{Eq. (3.27)} \\ & 0 \leq V_f \leq 0.5 \\ & -1 \leq U_x, U_y, U_z \leq 1 \\ & 0 \leq \rho \leq 1 \end{aligned} \tag{3.29}$$

where the objective function J is defined as the global compliance, Γ denotes the boundary where external force is applied, $\boldsymbol{f}$ denotes the force, $\boldsymbol{u}$ denotes the displacement, $\boldsymbol{K}$ denotes the global stiffness matrix ,which is assembled from the local stiffness matrix, $\widehat{\boldsymbol{K}}_e$, in Eq. (3.10), g_v denotes the volume constraint and V_0 denotes the target volume of the optimised result. The bound of the fibre volume fraction is set from 0 to 0.5 which models the scenario from no fibre to the average maximum value of fibre-reinforced composites manufactured by filament deposition modelling.

The optimisation is performed using IPOPT, a primal-dual interior-point algorithm with a filter line-search method for nonlinear programming (Wächter and Biegler, 2005). IPOPT exploits the first and second order derivatives of the objective and constraint functions. The first order derivatives are evaluated using the adjoint method introduced in last section whilst the second order derivatives are approximated by IPOPT using L-BGFS (limited-memory Broyden–Fletcher–Goldfarb–Shanno algorithm). The advantage of using second-order optimisers is that second-order derivatives typically provide a better step size and search direction, enabling convergence in fewer iterations (Rojas-Labanda and Stolpe, 2015). The termination criteria are when the objective function decreases by less than 0.01% and the constraint violation is

less than 10^{-4} in five successive iterations.

3.6 Summary

This chapter presents a framework for optimising both topology and fibre orientation. It begins by establishing a constitutive law based on the linear elasticity theory. The microscale model of unidirectional fibre-reinforced composites is then detailed, along with the stiffness matrix derivation accounting for fibre volume fraction and orientation.

Topology optimisation using the SIMP approach is integrated with fibre orientation optimisation. A pseudo-density field controls local material stiffness, which is a interpolant of the fibre volume fraction and the fibre orientation. An optimisation problem is formulated to minimise compliance. In summary, this framework enables comprehensive optimisation of both topology and fibre orientation, allowing for the exploitation of anisotropic material properties for lightweighting.

Chapter 4

Fibre Orientation Optimisation Results

The optimisation framework developed in the Chapter 3 uses the microscale model and SIMP approach to describe the mechanical properties. In this chapter, two numerical design problems are presented considering the fibre orientation optimisation to validate the microscale model solely without the interaction between the fibre orientation and topology. The manufacturing constraints are also enabled in these 2D cases, where the visualisation of the fibre orientation is easier, to validate the generation of the fibre path. Note that the pseudo-density is assigned a value of 1 for the entire domain during the optimisation and the volume constraint is disabled to optimise only the fibre orientation. The optimisation formulation used in this chapter is written as

$$\begin{aligned} \min_{V_f, \boldsymbol{U}, S} \quad & J(V_f, \boldsymbol{U}) = \int_\Gamma \boldsymbol{f} \cdot \boldsymbol{u} dx \\ s.t. \quad & \boldsymbol{f} = \boldsymbol{K} \cdot \boldsymbol{u} \\ & C_1 \quad \text{Eq. (3.26)} \\ & C_2 \quad \text{Eq. (3.27)} \\ & 0 \leq V_f \leq 0.5 \\ & -1 \leq U_x, U_y \leq 1 \end{aligned} \tag{4.1}$$

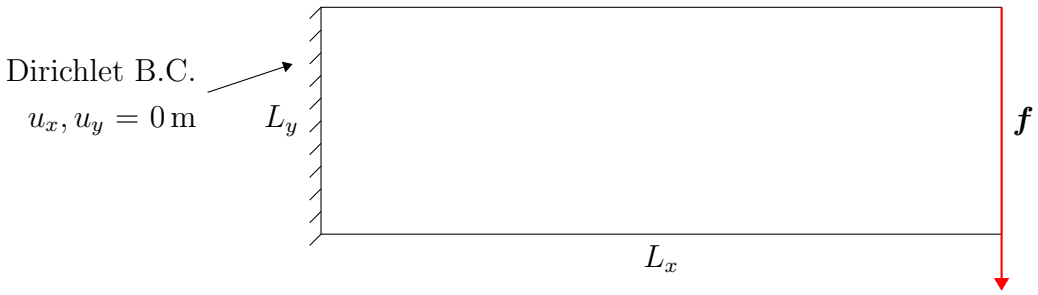


Figure 4.1: The design domain and the boundary condition of the 2D cantilever beam

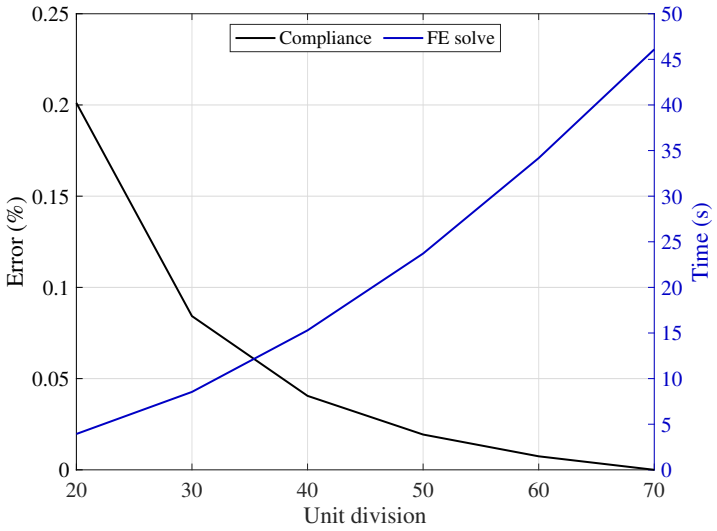


Figure 4.2: The mesh convergence study for the 2D cantilever beam problem. Note that the mesh convergence study was performed in series using one AMD EPYC 7316 processors operating at 3 GHz

4.1 Cantilever Beam (2D)

To better validate the microscale model, a simple 2D cantilever beam problem as shown in Fig. 4.1 is firstly solved. A uniform force, $\boldsymbol{f} = 1000\,\mathrm{N\,m^{-1}}$, is applied on the right edge whilst a Dirichlet boundary condition is applied on the left edge, resulting in a bending loading condition. A mesh convergence study has concluded that the error is less than 0.05% after the unit division is larger than 40 (see Fig. 4.2). Hence, the design domain is discretised into 150×50 quadrilateral elements, with 7,701 nodes, using an element size of 0.02 m. The problem setup is summarised in Tab. 4.1. Note that the selection of material properties is based on the potential in-situ manufacturing process, with the tensile Young's modulus of carbon fibre and the Young's modulus of epoxy chosen as E_f and E_m, respectively.

Table 4.1: The problem setup of the 2D cantilever beam

Mesh	
Element	2D Quadrilateral
L_x	3 m
L_y	1 m
Element size	0.02 m
Number of elements	7,500
Number of nodes	7,701
Number of design variables	38,505
Optimisation	
r_h (Helmholtz filter radius)	0.02 m
r_b (Helmholtz filter boundary radius)	N/A
p (SIMP parameter)	N/A
V_0 (target volume)	N/A
Initial guesses	
(U_x, U_y)	(1,0)
V_f	0.5
S	y
Material properties	
E_f	130 GPa
E_m	3.6 GPa
ν_f	0.3
ν_m	0.35

4.1.1 Design without Manufacturing Constraints

The fibre orientation optimisation of the cantilever beam without manufacturing constraints required 61 iterations before meeting the termination criteria (see Fig. 4.3). The optimised fibre orientation and fibre volume fraction are illustrated in Fig. 4.4.a. The fibre orientation visualised using short lines shows that the fibre orientation follows the principal stress direction (see Fig. 4.4.b and Fig. 4.4.c), forming a gradually converging fibre orientation from left to right. The fibre volume fraction reaches its upper bound all region to achieve the minimum compliance design with the exception of where the stresses are close to zero. The magnitude of the principal stress shows that the stress level at the region where the fibre volume fraction does not reach its upper bound is very low so that it is trivial when the optimisation achieve convergence.

To fabricate the fibre-reinforced composite, the fibre orientation needs to be interpreted into

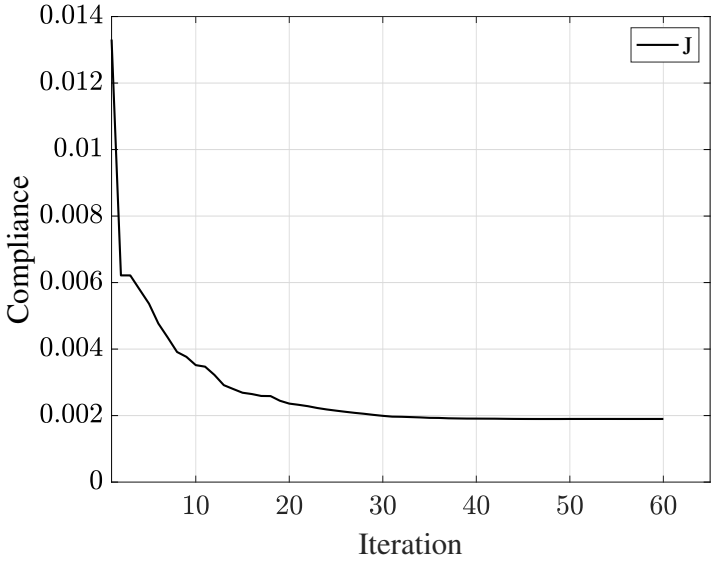
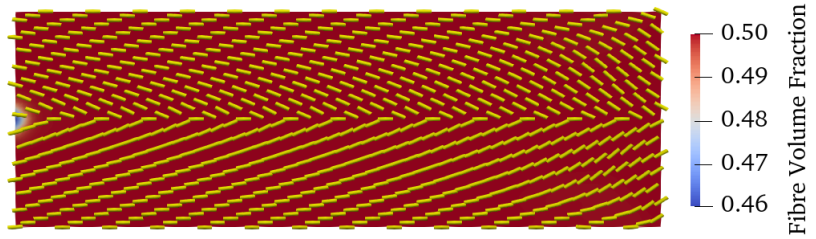


Figure 4.3: The convergence plot of the 2D cantilever beam optimisation without manufacturing constraint

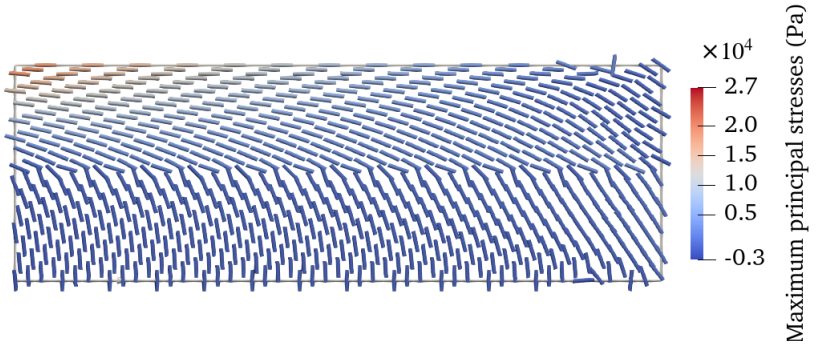
fibre paths. A simple approach of using streamlines of the fibre orientation field is illustrated in Fig. 4.5. Two seeding approaches are used: evenly seeding and randomly seeding. The seeds of the first approach are located at the left edge, whilst the seeds of the second approach are randomly distributed in the domain. The evenly seeded streamlines show denser fibres at the low fibre volume fraction area, and the randomly seeded streamlines have denser fibre at the top and bottom sides of the domain. This illustrates that streamlines are not able to represent the fibre paths with the corresponding fibre volume fraction. This proves that post-processing is typically needed to correctly represent the fibre paths with corresponding fibre volume fraction using streamlines. An example of the seed location selection can be found in Shafighfard et al. (2021). Additionally, in order to reach the required amount of fibre content, the gaps need to be filled by short and terminated fibres, resulting in gaps and resin-rich areas which increase the potential for structural failure. Hence, manufacturing constraints are needed to ensure continuous fibre orientation and to generate the fibre paths.

4.1.2 Design with Manufacturing Constraints

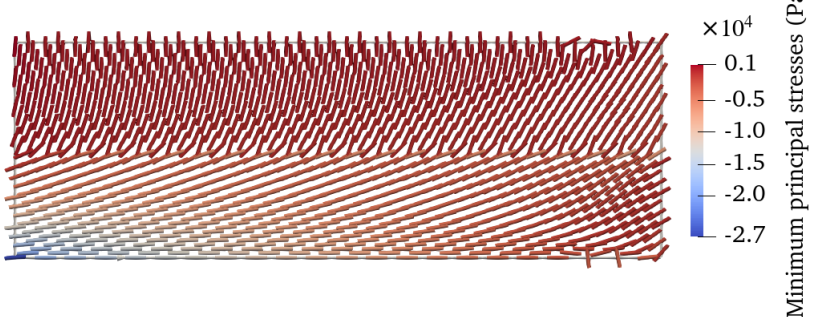
The optimisation with manufacturing constraints required 232 iterations before meeting the termination criteria (see Fig. 4.6) which is almost four times longer than the case without manufacturing constraints. It shows that it is more difficult for the objective functional to converge



(a)



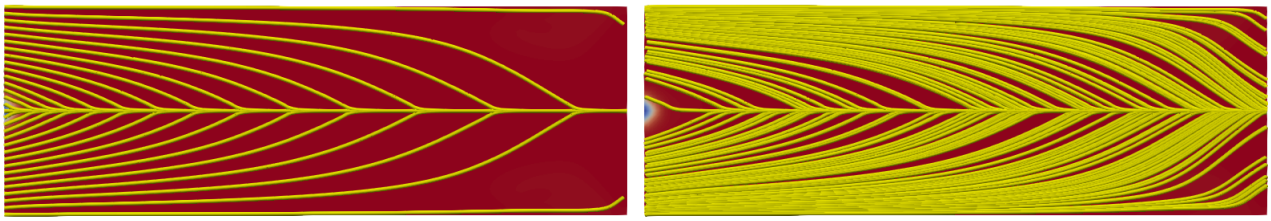
(b)



(c)

Figure 4.4: (a) The optimised fibre orientation and the fibre volume fraction of the cantilever beam without manufacturing constraints (b) The maximum principal stresses (c) The minimum principal stresses

whilst meeting the manufacturing constraints. The fibre orientation and fibre volume fraction are illustrated in Fig. 4.7. Comparing it to the design without manufacturing constraints, the fibre orientation remains horizontal on the right-hand side, whilst the fibre volume fraction reduces to 0 at the middle of the left-hand side. Due to the requirement of continuity enforced by the manufacturing constraints, the variation of the fibre orientation and the fibre volume fraction are linked. Tracing the variation from right to left, the fibre volume fraction at its upper bound starts to drop as the fibre orientation diverges along the diagonal towards the centre of the domain. This shows that, in order to maintain a large fibre volume fraction in



(a) (b)

Figure 4.5: The fibre paths generated using streamlines: (a) evenly-seeded (b) randomly-seeded

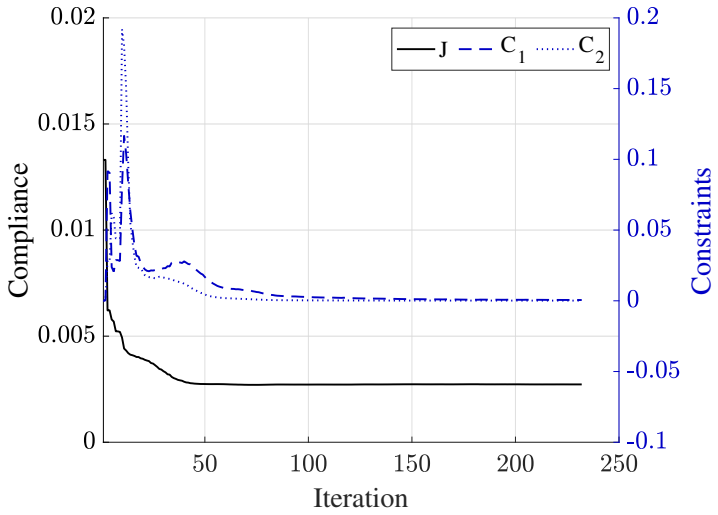


Figure 4.6: The convergence plot of the 2D cantilever beam optimisation with manufacturing constraints

most of the domain, the anisotropic characteristics are compromised, resulting in horizontal fibre orientation in some regions.

The fibre path illustrated in Fig. 4.8.a is generated using the iso-contours of the scalar field, S (see Fig. 4.8.b). It clearly demonstrates continuous fibre path with corresponding variation in the fibre volume fraction, where the distances between the fibre paths increase as the fibre volume fraction decreases. The manufacturing constraints successfully ensure the continuity and generate fibre path without the requirement of additional post-processing.

The compliance comparison shown in Tab. 4.2 indicates that the design without manufacturing constraints has a significant reduction of 35% compared to the straight fibres which the fibre orientation is horizontal and the fibre volume fraction is 0.5. The design with manufacturing constraints shows a 7% reduction in compliance compared to the straight fibres and a significant improvement in manufacturability by varying the fibre orientation whilst sacrificing part of the

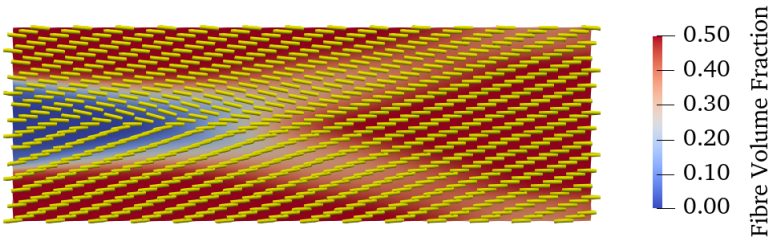
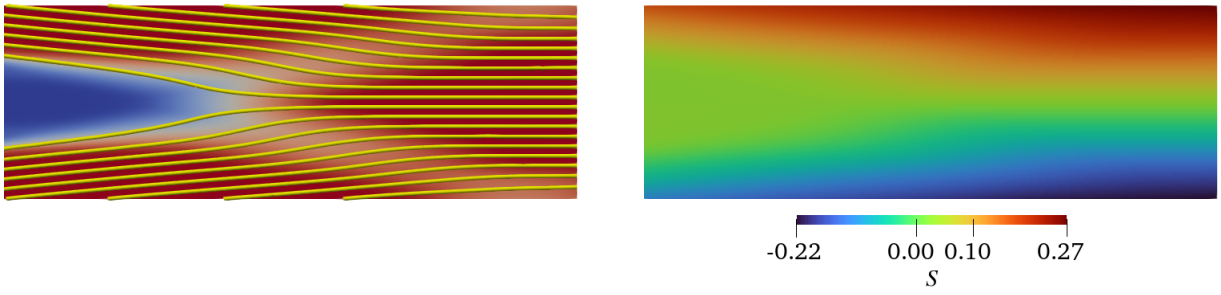


Figure 4.7: The optimised fibre orientation and the fibre volume fraction



(a) (b)

Figure 4.8: The fibre paths generated using iso-contours: (a) the extracted fibre paths (b) the scalar field (Note that the number of iso-countours is chosen as 20 instead of using Eq. 3.21 for a better visualisation)

fibre content at the low stress area. Although a 7% improvement might not be sufficient to justify changing the manufacturing process from simple straight fibres, it is important to note that the results presented in this chapter are intended to validate the microscale model and demonstrate the effectiveness of the manufacturing constraints, rather than to achieve the ultimate optimisation objective.

4.2 Beam with Open Holes (2D)

To demonstrate the ability of the manufacturing constraints to ensure continuous fibre path with a more challenging geometry, a 2D beam with open holes as shown in Fig. 4.9 is then

Table 4.2: The compliance comparison of the 2D cantilever beam

Case	Compliance (N m)
Straight fibres	2.93×10^{-3}
Design without manufacturing constraints	1.90×10^{-3}
Design with manufacturing constraints	2.73×10^{-3}

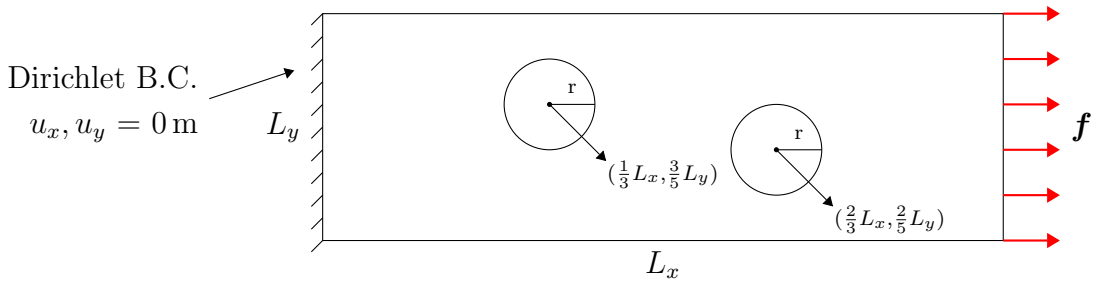


Figure 4.9: The design domain and the boundary condition of the 2D beam with open holes

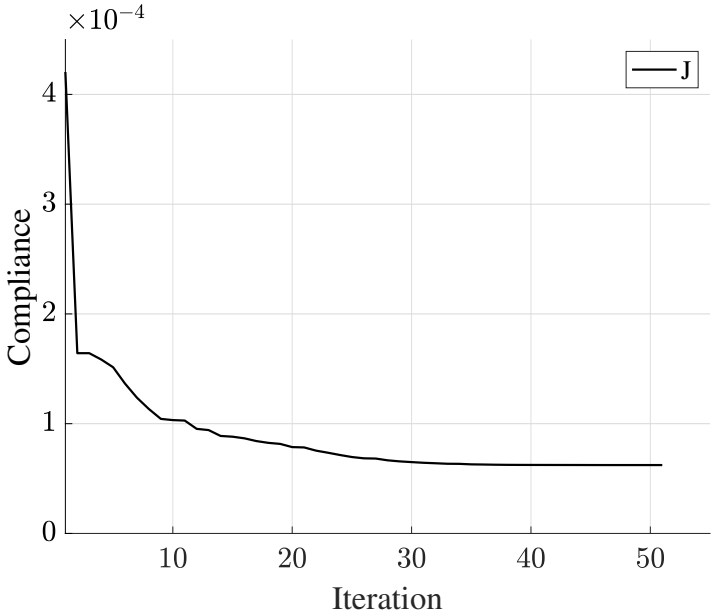


Figure 4.10: The convergence plot of the 2D beam with open holes optimisation without manufacturing constraints

solved. A uniform force, $\boldsymbol{f} = 1000\,\mathrm{N\,m^{-1}}$, is applied on the right edge whilst a Dirichlet boundary condition is applied on the left edge, resulting in a tensile loading condition. The design domain is discretised to 16,294 triangular elements, with 8,410 nodes, using an element size of 0.02 m. The problem setup is summarised in Tab. 4.3.

4.2.1 Design without Manufacturing Constraints

The convergence plot illustrated in Fig. 4.10 shows the optimisation required 51 iterations before meeting the termination criteria. The optimised design without manufacturing constraints illustrated in Fig. 4.11.a shows the fibre orientation follows the maximum principal stress direction (see Fig. 4.11.b) turns round the open holes to distribute the tensile stress which is similar to the well-known single open hole problem (Shafighfard et al., 2021). Whilst the fibre

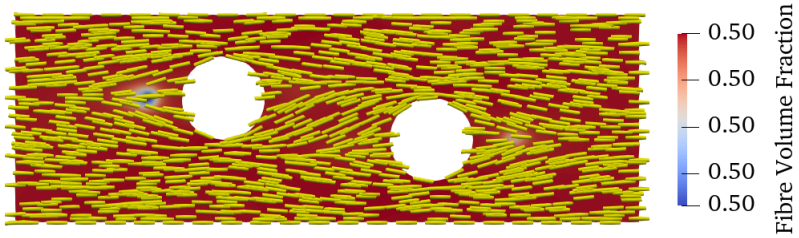
Table 4.3: The problem setup of the 2D beam with open holes

Mesh	
Element	2D Triangular
L_x	3 m
L_y	1 m
r	0.2 m
Element size	0.02 m
Number of elements	16,294
Number of nodes	8,410
Number of design variables	42,050
Optimisation	
r_h (Helmholtz filter radius)	0.02 m
r_b (Helmholtz filter boundary radius)	N/A
p (SIMP parameter)	N/A
V_0 (target volume)	N/A
Initial guesses	
ρ	1
(U_x, U_y)	(1,0)
V_f	0.5
S	y
Material properties	
E_f	130 GPa
E_m	3.6 GPa
ν_f	0.3
ν_m	0.35

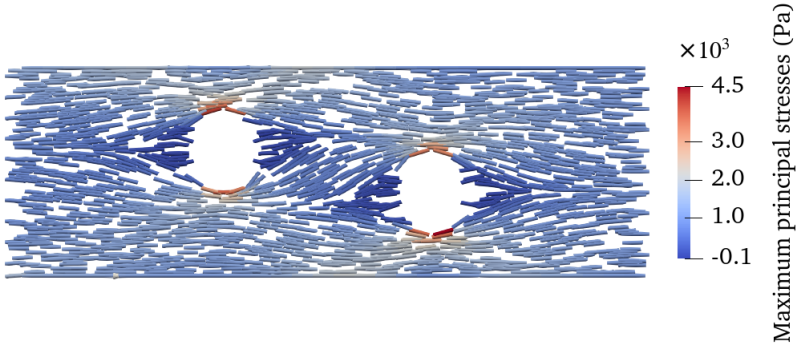
volume fraction is pushed to its upper bound to achieve the objective. The fibre path generated using randomly seeded streamlines is shown in Fig. 4.11.d which is not able to represent the corresponding fibre volume fraction. As discussed in the previous cantilever beam problem, post-processing is needed to seed the streamlines to successfully represent the correct fibre volume fraction, especially at the region close to the open holes.

4.2.2 Design with Manufacturing Constraints

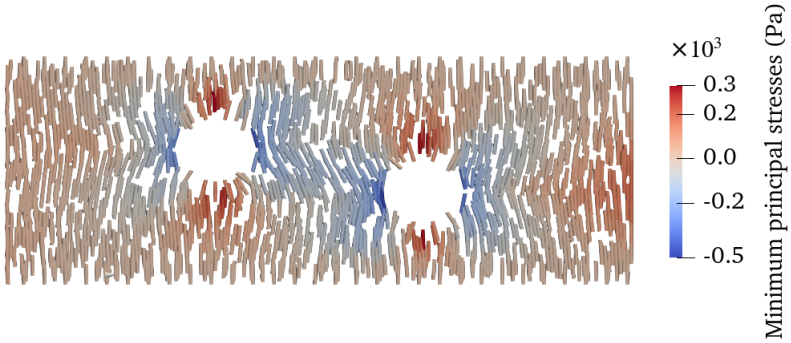
The optimisation required 249 iterations before meeting the termination criteria (see Fig. 4.12). The optimised design with manufacturing constraints, shown in Fig. 4.13, illustrates a similar pattern of fibre orientation, comparing to the design without manufacturing constraints, which turns around the holes and generates a more interesting result, compared to the single hole



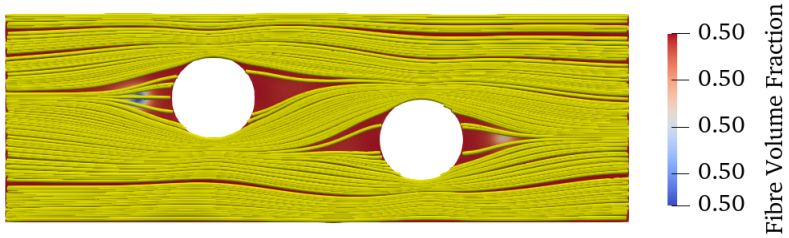
(a)



(b)



(c)



(d)

Figure 4.11: (a) The fibre orientation and fibre volume fraction of the design without manufacturing constraints (b) The maximum principal stresses (c) The minimum principal stresses (d) The fibre paths generated using randomly seeded streamlines

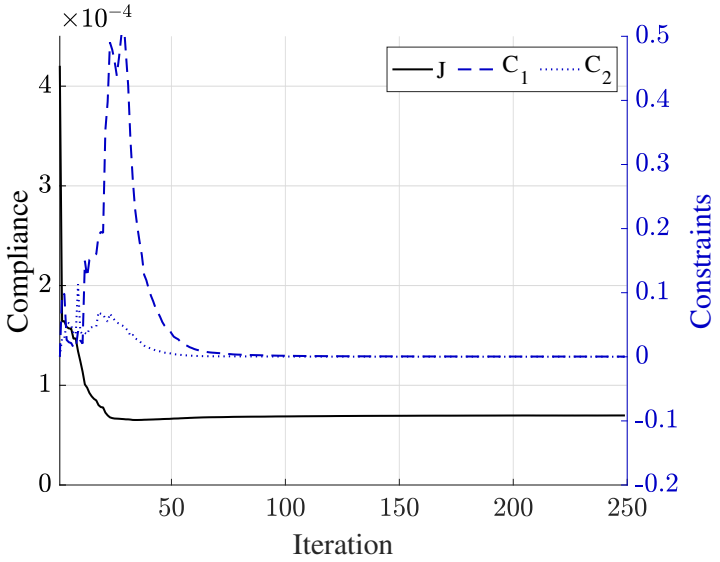


Figure 4.12: The convergence plot of the 2D beam with open holes optimisation with manufacturing constraints

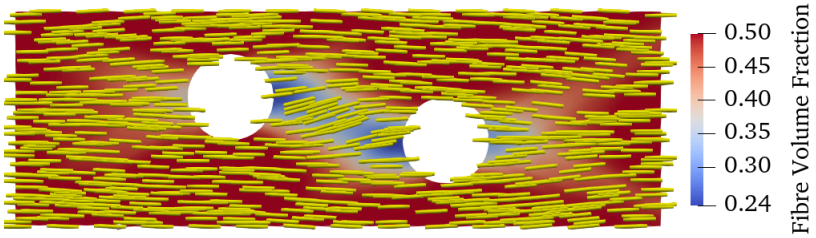
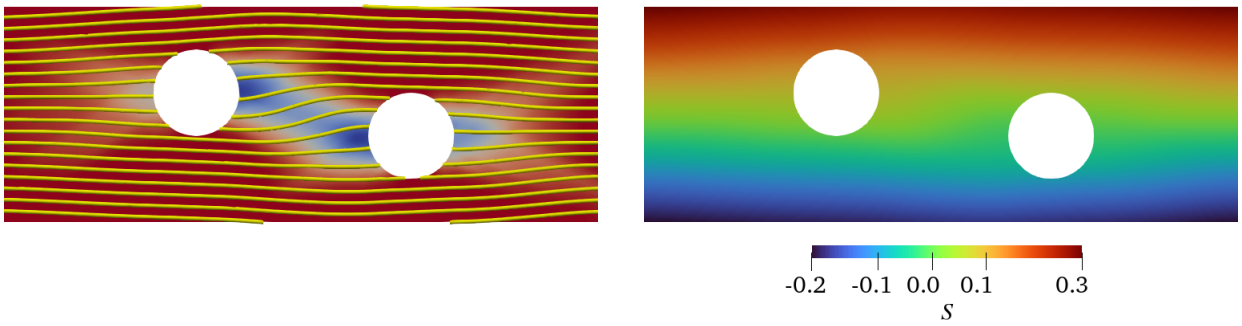


Figure 4.13: The optimised fibre orientation and the fibre volume fraction

problem. However, the fibre volume fraction drops at the region where the fibre orientation diverges or converges to meet the continuity constraints.

Fig. 4.14 depicts the fibre path extracted from the scalar field which shows the distance between the fibre paths increases when the fibre volume fraction decrease. This indicates that the manufacturing constraints successfully ensure the continuity and generate reasonable fibre paths without additional post-processing.

The comparison of compliance, as shown in Tab. 4.4, indicates a 15% reduction when the manufacturing constraints are disabled and a 5% reduction when they are enabled compared to the design of straight fibres with maximum fibre content. This indicates that routing the fibre orientation around the open holes helps to improve the structural performance. This also shows that the structural performance is still improved even when the design with manufacturing constraints sacrifices part of the fibre content at the region to route the fibre path around the



(a) (b)

Figure 4.14: The fibre paths generated using iso-contours: (a) the extracted fibre paths (b) the scalar field (Note that the number of iso-countours is chosen as 20 instead of using Eq. 3.21 for a better visualisation)

Table 4.4: The compliance comparison of the 2D beam with open holes

Case	Compliance (N m)
Straight fibres	7.30×10^{-5}
Design without manufacturing constraints	6.23×10^{-5}
Design with manufacturing constraints	6.97×10^{-5}

open holes whilst ensuring the manufacturability.

4.3 Summary

In this chapter, two numerical examples are presented to validate the microscale model and the manufacturing constraints. In both examples, the optimised designs without the manufacturing constraints possess the fibre orientation following the principal stress direction and the almost maximum fibre content to achieve the minimum compliance design. Meanwhile, the optimised designs with the manufacturing constraints shows continuous fibre path with reasonable fibre volume fraction.

The microscale model and the manufacturing constraints are clearly validated through the examples presented in this chapter. The designs from the combination of the topology and fibre orientation optimisation is demonstrated in the next chapter.

Chapter 5

Topology and Fibre Orientation Optimisation Results

In this chapter, three numerical design problems with different geometries and loading conditions are solved to demonstrate the ability of the developed framework to combine the topology and fibre orientation optimisation. Firstly, a cantilever beam subjected to bending is presented to illustrate the efficacy of the framework in optimising the topology and fibre orientation whilst ensuring manufacturability using five different scenarios. Subsequently, a twisted and compressed column problem and a more complex L-shape beam problem with mixed loading conditions are solved to demonstrate the ability to handle various loading conditions and complex geometries.

5.1 Cantilever Beam

In this section, a numerical design problem of a cantilever beam is presented to illustrate the spatially-optimised fibre-reinforced composites and the manufacturing constraints. Five scenarios based on different settings for the fibre volume fraction, the fibre orientation and the

Table 5.1: Scenarios for the numerical design problem. The design variables, V_f and $\boldsymbol{U}$, and additive manufacturing constraints are considered as control variables of the numerical design problem. The isotropic case uses homogeneous mechanical properties, E_s and ν_s, listed in Tab. 5.2 to represent a random-oriented short fibre-reinforced composite with a fixed 50% fibre volume fraction. In the unidirectional case, the fibre volume fraction is fixed to 50% and the fibre orientation is changed from spatially-varying vectors to a single vector to represent a unidirectional fibre-reinforced composite. Note that using the maximum fibre content, compared to other cases, in the first two cases is expected to illustrate the advantage of using spatially-varying fibre orientation more clearly. The continuity constraints are enabled in the last two cases, and the fibre path generation constraints are only enabled in the last case.

	Control variables of the numerical design problem			
Cases	V_f	$\boldsymbol{U}$	Continuity constraints C_1 Eq. (3.26)	Fibre path generation constraints C_2 Eq. (3.27)
Isotropic	$V_f = 0.5$	Random fibre orientation	Disabled	Disabled
Unidirectional	$V_f = 0.5$	Single vector	Disabled	Disabled
Spatially-optimised	$0 \leq V_f \leq 0.5$	Spatially-varying vectors	Disabled	Disabled
Continuity	$0 \leq V_f \leq 0.5$	Spatially-varying vectors	Enabled	Disabled
Fibre path generation	$0 \leq V_f \leq 0.5$	Spatially-varying vectors	Enabled	Enabled

manufacturing constraints are considered (see Tab. 5.1) using the optimisation formulation

$$
\begin{aligned}
\min_{V_f, \boldsymbol{U}, \rho, S_1, S_2} \quad & J(V_f, \boldsymbol{U}, \rho) = \int_\Gamma \boldsymbol{f} \cdot \boldsymbol{u} dx \\
s.t. \quad & \boldsymbol{f} = \boldsymbol{K} \cdot \boldsymbol{u} \\
& g_v = \int_\Omega \overline{\rho} dx - V_0 \leq 0 \\
& C_1 \quad \text{Eq. (3.26)} \\
& C_2 \quad \text{Eq. (3.27)} \\
& 0 \leq V_f \leq 0.5 \\
& -1 \leq U_x, U_y, U_z \leq 1 \\
& 0 \leq \rho \leq 1
\end{aligned}
\tag{5.1}
$$

The spatially-optimised case is firstly benchmarked against the isotropic case and unidirectional case to show the advantage of using fibre-reinforced materials and varying the fibre orientation spatially. Subsequently, the manufacturing constraints are enabled each by each in the last two

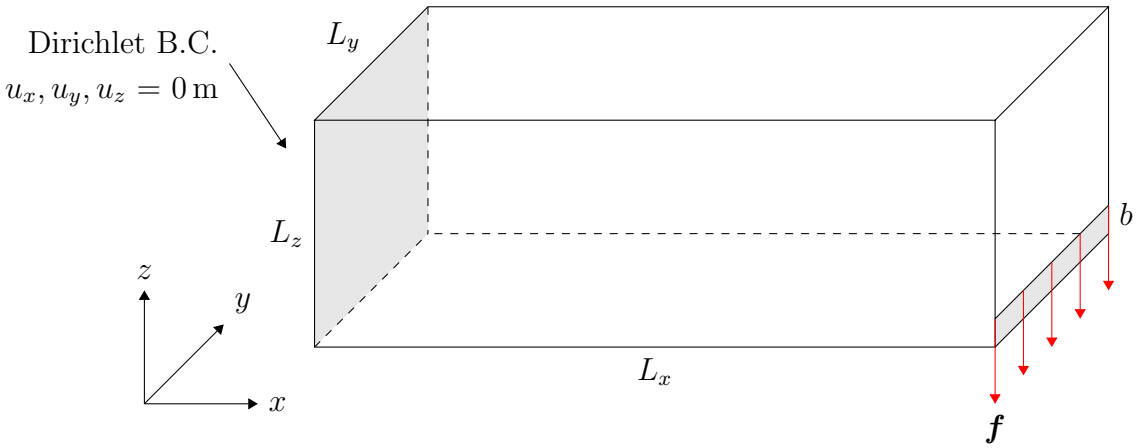


Figure 5.1: Geometry and boundary conditions of the cantilever beam

examples to show how the manufacturability is ensured step by step.

The design variables are spatially-varying within their bound constraints in the design domain except for the unidirectional case and isotropic case. For the unidirectional case, the fibre volume fraction is fixed to its upper bound and the fibre orientation is changed from spatially-varying vectors to a single vector to represent a unidirectional fibre-reinforced composite. Note that the mechanical properties are evaluated by substituting V_f and $\boldsymbol{U}$ into Eq. (3.6) except the isotropic case. The isotropic case is considered using conventional SIMP using homogeneous mechanical properties evaluated by the Cox-Krenchel model (Sanomura and Kawamura, 2003; Avanzini et al., 2022) to represent a random-oriented short fibre-reinforced composite with a fixed 50% fibre volume fraction. The continuity constraints are enabled in the last two cases, and the fibre path generation constraints are only enabled in the last case.

5.1.1 Problem Setup

The geometry of the cantilever beam is shown in Fig. 5.1. A uniform force, $\boldsymbol{f} = 1000\,\mathrm{N\,m^{-2}}$, is applied to the bottom-right as shown and the target volume of optimised results is set to the 12% volume of the design domain in order to achieve a lightweight structure and show small details in the optimised design. A mesh convergence study concluded that discretising the geometry into 365,673 tetrahedral elements using a mesh size of $1/30\,\mathrm{m}$ could achieve the balance between accuracy ($< 0.5\%$ error) and the computational cost (see Fig. 5.2). The material properties and the initial guesses of the design variables are listed in Tab. 5.2. Note that several initial

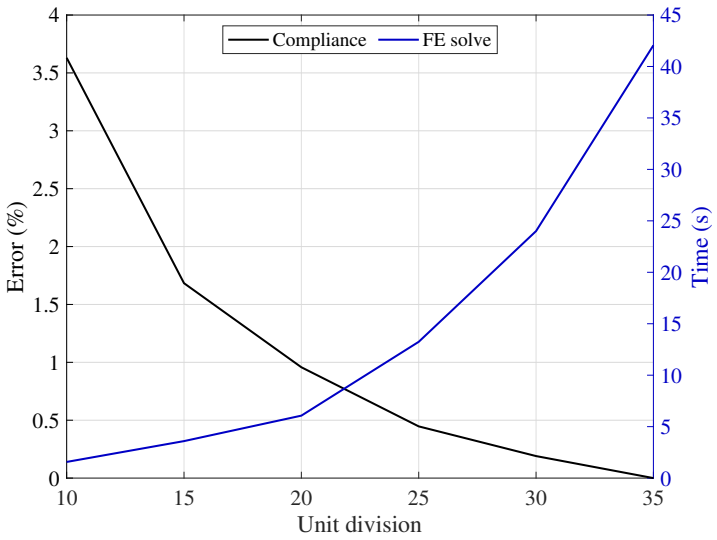


Figure 5.2: The mesh convergence study of the 3D cantilever beam problem. Note that the mesh convergence study was performed in serial using one AMD EPYC 7316 processors operating at 3 GHz.

guesses have been tested. The convergence performance is significantly quicker when the initial guesses of the design variables are located in feasible design space. The values listed in Tab. 5.2 avoid large constraint violation and keep the initial guesses in the feasible design space.

The penalisation factor is set to 3. The regularisation length scale of the Helmholtz filter radius, r_h, is equal to the mesh size to capture small details whilst reducing the intermediate pseudo-density. The boundary length scale for the Robin boundary condition, r_b, to solve the Helmholtz-type filter is equal to the filter radius. Note that all the present result geometry isosurfaces have threshold of 50% on ρ for a better visualisation. The fibre orientation is visualised by streamlines with random seed points and coloured in the magnitude of the fibre volume fraction.

5.1.2 Cases without Manufacturing Constraints

The manufacturing constraints, C_1 and C_2 are disabled in the cases presented in this section. The optimised topologies are shown in Fig. 5.3 where the isotropic case shows a typical result of topology optimisation for the cantilever problem, the topology of the unidirectional case is composed of a diagonal member and a horizontal member without holes (see Fig. 5.3b), and the spatially-optimised case is composed of several members with three holes at the bottom-right

Table 5.2: The problem setup of the 3D cantilever beam

Mesh	
Element	3D tetrahedral
L_x	3 m
L_y	1 m
L_z	1 m
b	0.1 m
Element size	1/30 m
Number of elements	365,67
Number of nodes	65,887
Number of design variables	461,209
Optimisation	
r_h (Helmholtz filter radius)	1/30 m
r_b (Helmholtz filter boundary radius)	1/30 m
p (SIMP parameter)	3
V_0 (target volume)	12%
Initial guesses	
ρ	0.12
(U_x, U_y, U_z)	(1,0,0)
V_f	0.5
S_1	y
S_2	z
Material properties	
E_f	130 GPa
E_m	3.6 GPa
E_s	9.1 GPa
ν_f	0.3
ν_m	0.35
ν_s	0.32

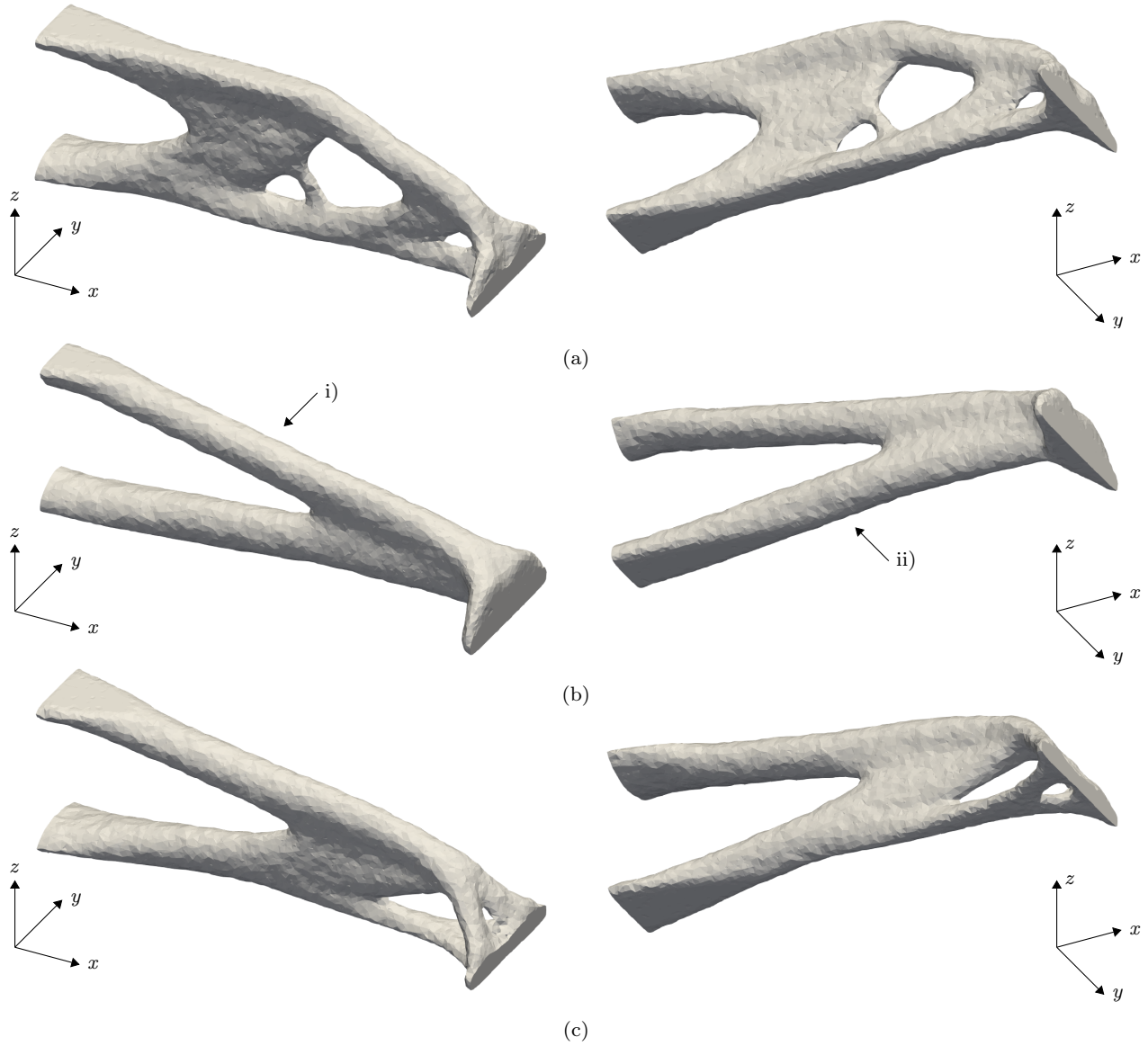


Figure 5.3: (a) Optimised topologies of the isotropic material case which has matrix only (b) The unidirectional case which is composed of a diagonal member i) and a horizontal member ii), and has a constant fibre volume fraction and a uniform fibre orientation, $(9.989, 0, -1.544)$ (c) The case in which the fibre orientation and the fibre volume fraction are spatially-optimised

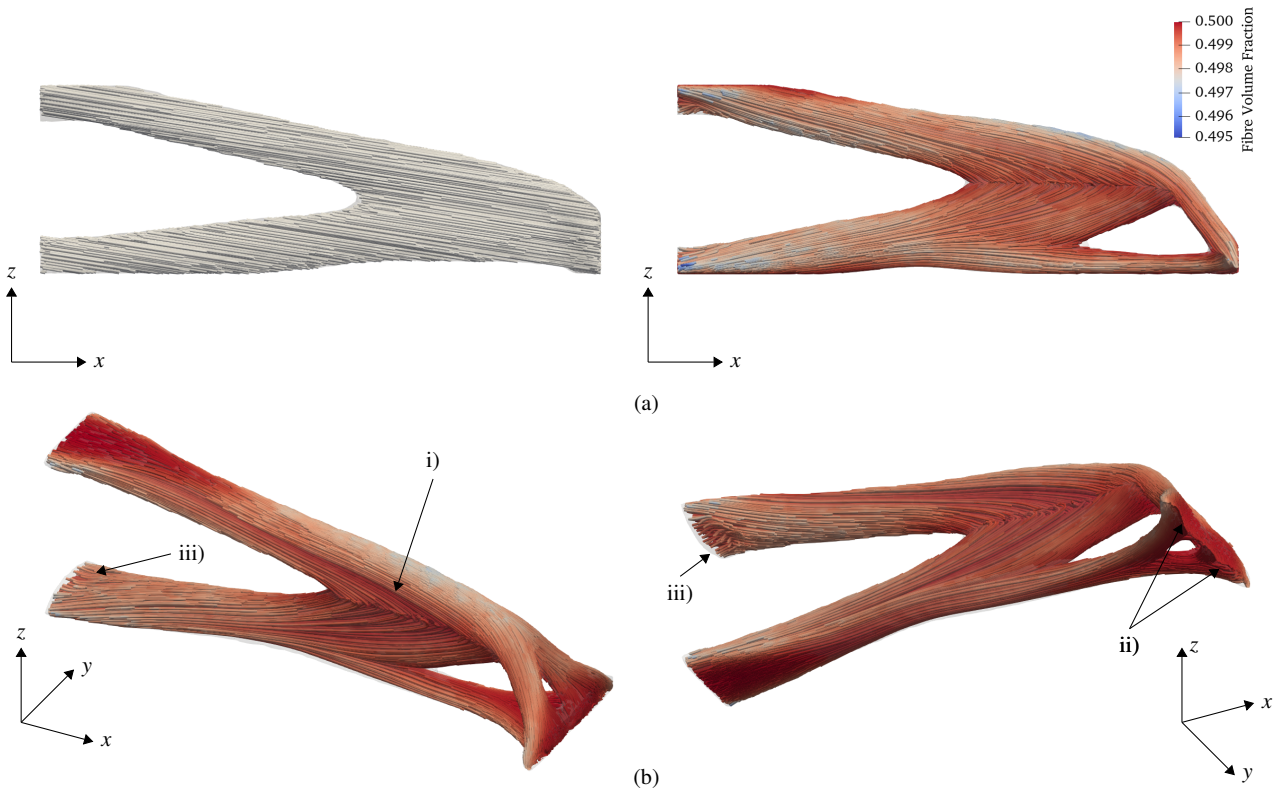


Figure 5.4: (a) Comparison of the constant fibre volume fraction unidirectional case and the spatially-optimised case (b) The different views of the spatially-optimised case where the labelled features are illustrated in Secs. 5.1.2

of the topology (see Fig. 5.3c). The comparison of the topologies shows that parameterising the fibre orientation change the topologies. The comparison of the fibre orientation presented in Fig. 5.4a shows that the unidirectional case has a uniform fibre orientation pointing to the direction $(9.989, 0, -1.544)$ and the spatially-optimised case presents a varying fibre orientation parallel to the topology layout. The fibre orientation is aligned with the principal stress direction (see Fig. 5.5). Due to the limitation of the single orientation, the fibre orientation is only aligned with the principal stress direction of the main diagonal member in the unidirectional case. To overcome the loss of not following the principal stress direction, the horizontal member is thicker than the diagonal member (see Fig. 5.3b.i and Fig. 5.3b.ii).

From the manufacturability point of view, the unidirectional case can be manufactured by layering up with support materials on the xz plane. In contrast, the spatially-optimised case shown in Fig. 5.4b has shown several issues that are not favourable for fabrication. First, sharp fibre turns are observed at the intersection area where the maximum principal stress direction

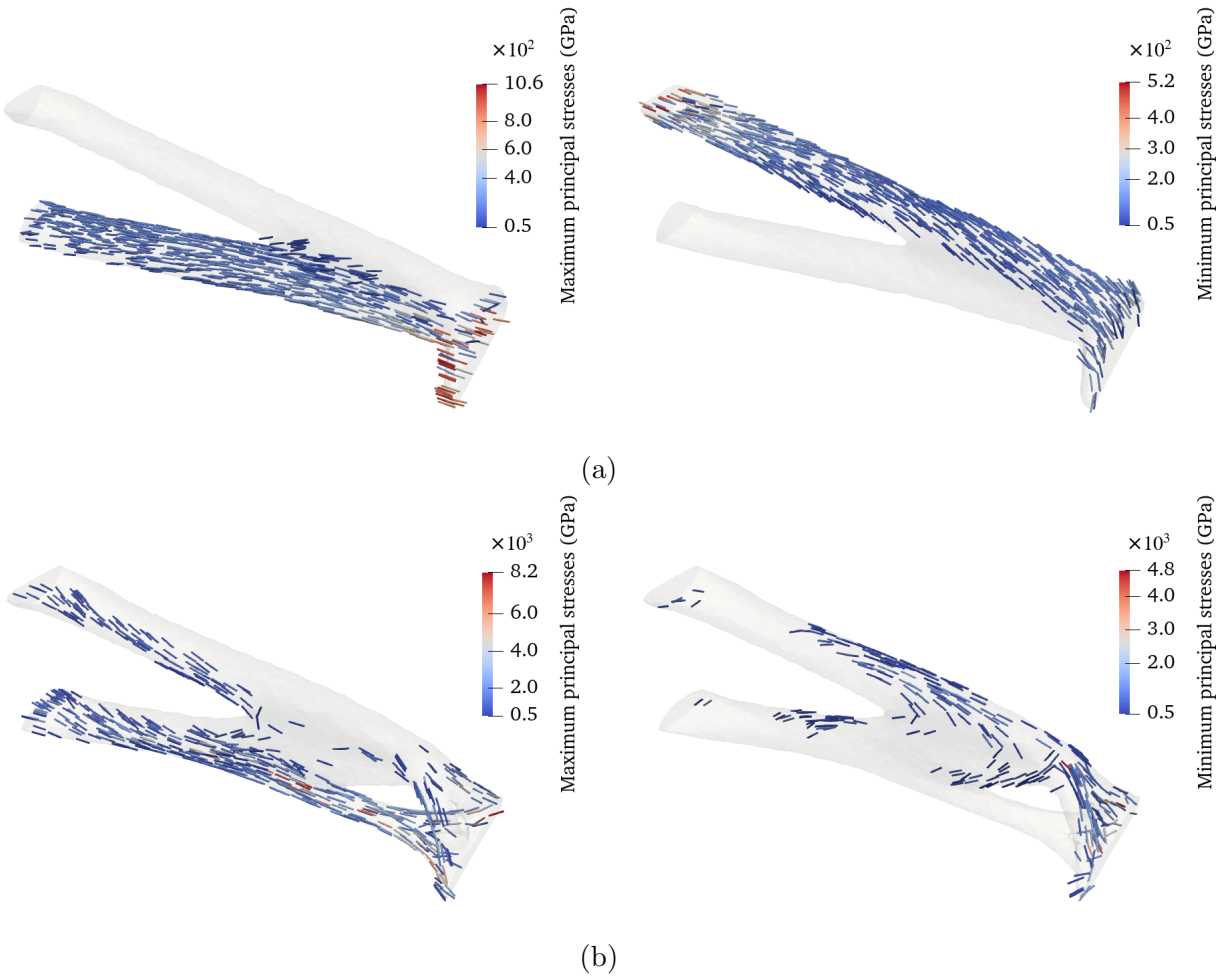


Figure 5.5: The maximum and minimum principal stresses of the (a) Unidirectional case and (b) Spatially-optimised case (Note that the stress magnitude lower than 0.5 GPa is not shown for a better visualisation)

changes. Some of the fibres connect together to form sharp turns (see Fig. 5.4b.i) and the rest of them result in discontinuous fibres (see Fig. 5.4b.ii). Second, gaps and the variation of distances between fibres can be observed (see Fig. 5.4b.iii) although the colour legend shows that the fibre volume fraction is almost constant. Furthermore, it is difficult to interpret the fibre volume fraction by these streamlines controlled by random seeding.

The convergence plots illustrated in Fig. 5.6 indicates that the required number of optimisation iterations is 173, 223 and 219 for the isotropic, unidirectional and spatially-optimised case, respectively. The unidirectional case took slightly more iterations to converge, compared to the other cases, possibly due to the the optimised single fibre orientation is sub-optimal in part of the design domain. Tab. 5.3 illustrates that the compliance shows significant improvements in the cases with fibres, compared to the isotropic material case. Furthermore,

the spatially-optimised case shows an extra 8.47% reduction in compliance, compared to the unidirectional case. Although the spatially-optimised case shows the best performance in terms of the compliance, the sharp fibre turns may result in the degradation of mechanical properties as discussed in previous section. These may also lead to fibre breakages which is a key factor leading the potential of composite failure. This comparison demonstrates the advantage of the fibre reinforcement and the need for the manufacturing constraints to discourage the problematic features and bridge the gap between optimal design with manufacturing.

5.1.3 Cases with Manufacturing Constraints

The first set of the manufacturing constraints considered is the continuity constraints (see Eq. (3.26)). The topology shown in Fig. 5.7a is composed of a diagonal member and a horizontal member which is similar to the unidirectional case. The fibre orientation shown in Fig. 5.8a illustrates that the fibre orientation is successfully constrained by the adapted continuity equation to form a smooth transition at the intersection area without the sharp fibre turns (see Fig. 5.8a.i). In addition, the fibre volume fraction variation is observed at the right of the topology where the fibre orientation varies significantly. This illustrates how the fibre volume fraction is linked with the fibre orientation by the continuity constraints.

As shown in Fig. 5.8a, the view in the xz plane shows the separation space between the fibres at the bottom right of the optimised topology decreases in the z direction while the view in the yz plane shows it increases in the y direction at the corresponding position. The decreased separation space between fibres in the z direction decreases the loss of the fibre volume fraction caused by the diverging fibres in the y direction (see Fig. 5.8a.ii). In addition, the fibre orientation in the main members before converging together is slightly oblique toward the boundary in the z direction instead of completely following the topology layout can be observed (see Fig. 5.8a.iii). This is caused by the feature of the continuity constraint that fibres cannot start or end inside the topology boundary so that fibre orientations oblique to enable extra fibres to join the structure. This illustrates the constraints for the fibre orientation fulfil the continuity equation and keep the fibre volume fraction as large as possible to minimise the compliance. As a result, a non-uniform fibre stacking in the transverse direction which is not

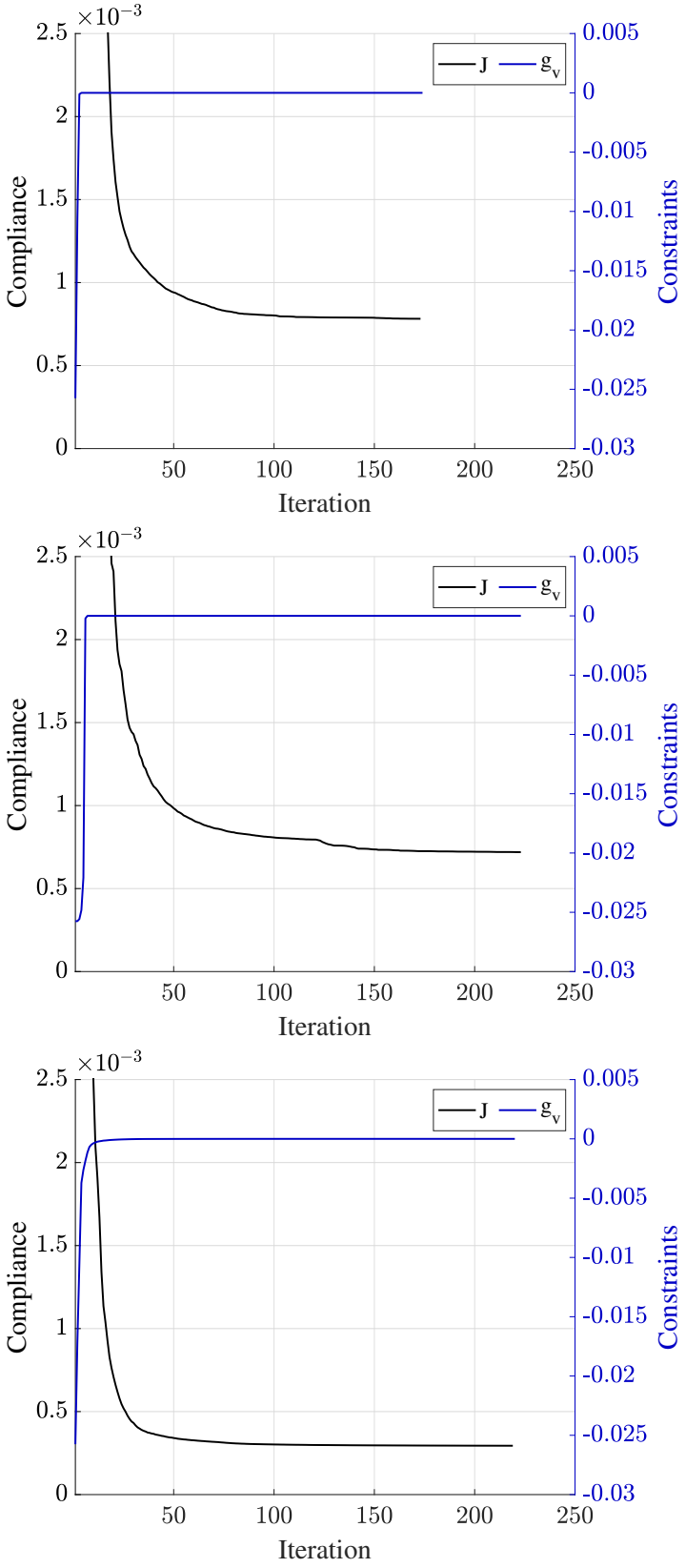


Figure 5.6: The convergence plots of the isotropic case (top), unidirectional case (middle) and unconstrained case (bottom)

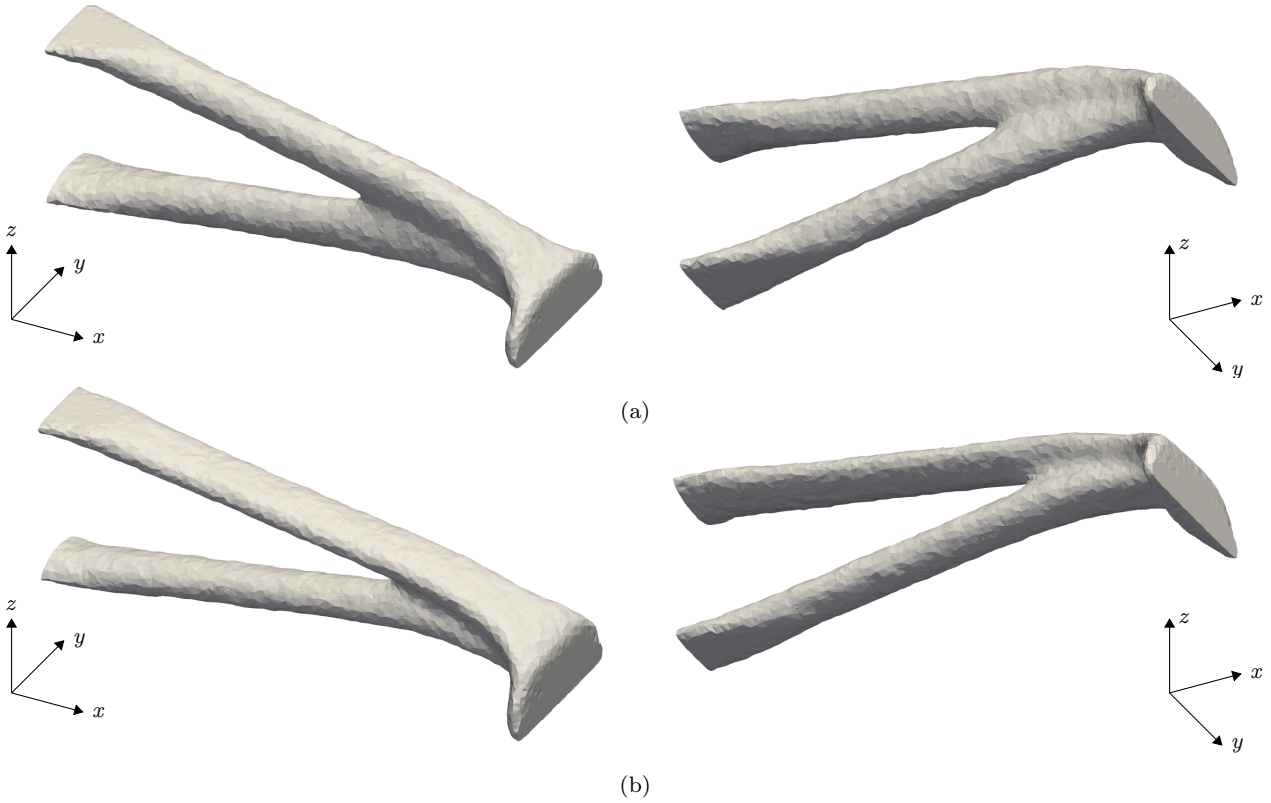


Figure 5.7: The optimised topologies of (a) the continuity case and (b) the fibre path generation case

able to be achieved while the width and thickness of the deposited fibre bundles are restricted by the nozzle geometry is generated. Despite the continuity constraints enforcing the smoothly varying fibre orientation and successfully capturing the variation of the fibre volume fraction, the manufacturability issue of non-uniform fibre stacking occurs and interpretation of the fibre path is needed.

The second set of the manufacturing constraints considered is the fibre path generation constraints (see Eq. (3.27)). It is expected to eliminate the non-uniform fibre stacking mentioned before since the aspect ratio and orthogonality constraints are restricting the shape, width and thickness of the deposited fibre bundles. The topology shown in Fig. 5.7b is thinner in the z direction and wider in the y direction, compared to the continuity case. The fibre orientation comparison in Fig. 5.8 shows that the fibre orientation at the right of the topology extends straight along x axis instead of diverging along the y axis (see Fig. 5.8b.i). This shows that the constraints for the aspect ratio and orthogonality discourage non-uniform fibre stacking, however, there may be a reduction in mechanical performance due to the fibre orientation no

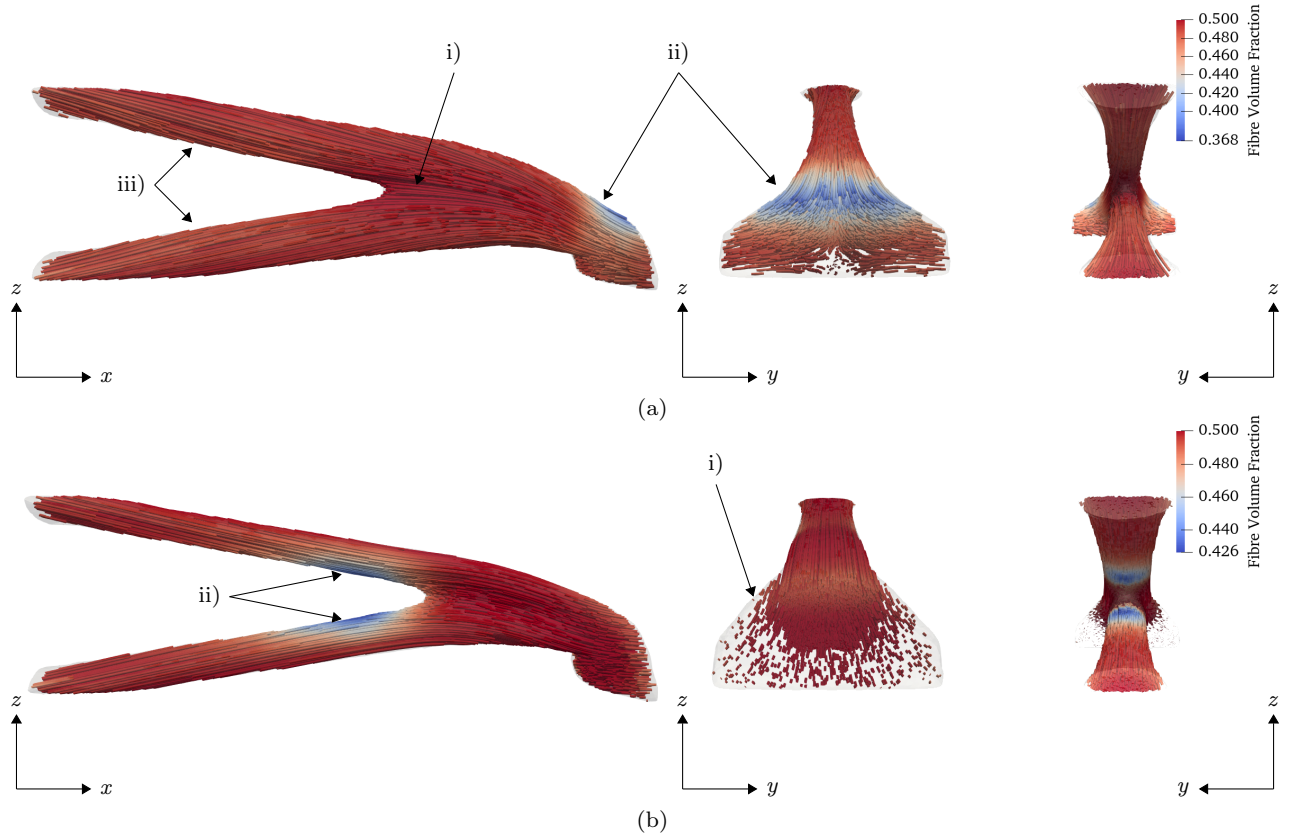


Figure 5.8: The fibre orientation of (a) the continuity case and (b) the fibre path generation case where the labelled features are illustrated and compared in Secs. 5.1.3

longer being fully aligned with the principal stress direction (see Fig. 5.9). The fibre volume fraction variation is observed at the bottom of the diagonal member and the top of the horizontal member where the fibre orientation turns to a closer direction before emerging together at the intersection area (see Fig. 5.8b.ii). Due to the curvature being larger at the outer side of the turning fibres which leads to an increase in the space between fibres, the fibre volume fraction decreases. This illustrates the decreased fibre volume fraction cannot be compensated by the oblique fibres or converging in the other transverse direction when the manufacturing constraints are considered.

From Fig. 5.8b and Fig. 5.10a, the streamlines which lie within the isosurfaces of S_1 and S_2 show the cross product of the scalar fields is aligned with the fibre orientation. Overlapping the isosurfaces of S_1 and S_2 gives Fig. 5.10b where the intersection curves are coincident with the fibre orientation. The cross section shown in Fig. 5.10b.i where the fibre volume variation is constant shows the isosurfaces form square grids. This illustrates that the orthogonality

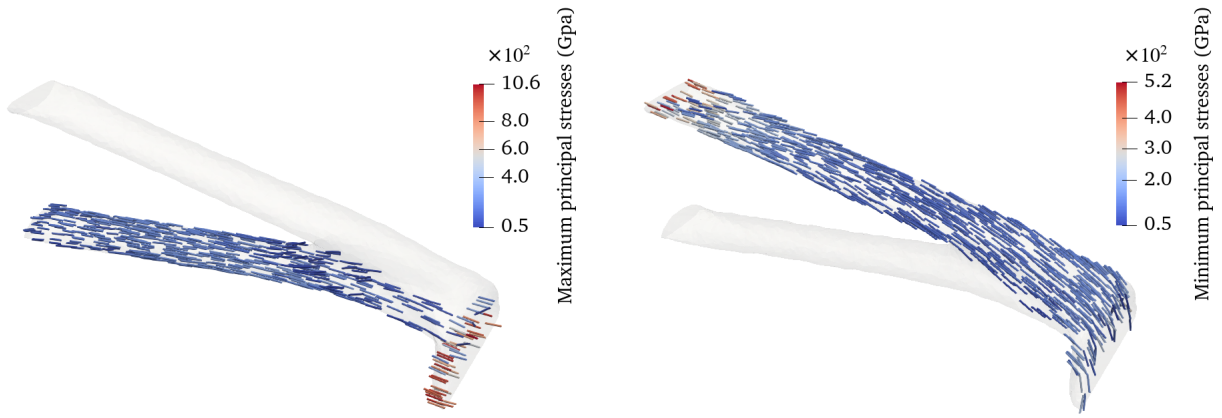


Figure 5.9: The principal stresses of the fibre path generation case (Note that the stress magnitude lower than 0.5 GPa is not shown for a better visualisation)

Table 5.3: Comparison of compliance

Case	compliance (N m)
Isotropic	7.82×10^{-4}
Unidirectional	7.15×10^{-4}
Spatially-optimised	2.94×10^{-4}
Continuity	3.99×10^{-4}
Fibre path generation	4.85×10^{-4}

of the gradients and the aspect ratio constraint are fulfilled. Another cross section shown in Fig. 5.10b.ii where the fibre volume fraction decreases from the top and bottom to the centre shows the distances between the isosurfaces increase as the fibre volume fraction decreases. This shows how the magnitude of the gradients successfully represent the fibre volume fraction. The cross section at $y = 0.5$ m shown in Fig. 5.10b.iii also provides an evidence that the distances between isosurfaces are varying with the fibre volume fraction. The intersection curves are then extracted as fibre paths shown as Fig. 5.10c. The coordinates of the curves give the paths for the print head and the gradients of the scalar fields provide the information about layer height and printing width for slicing software to generate printer toolpaths.

Comparing the convergence plots shown in Fig. 5.6 and Fig. 5.11, the optimisation ran for 205 iterations on average in the cases without manufacturing constraints; however, as the number of the manufacturing constraints increases, the number of optimisation iterations increases to 559 and 727 in the continuity case and the fibre path generation case, respectively. This indicates the optimisation took longer to find the feasible design space to meet the constraints

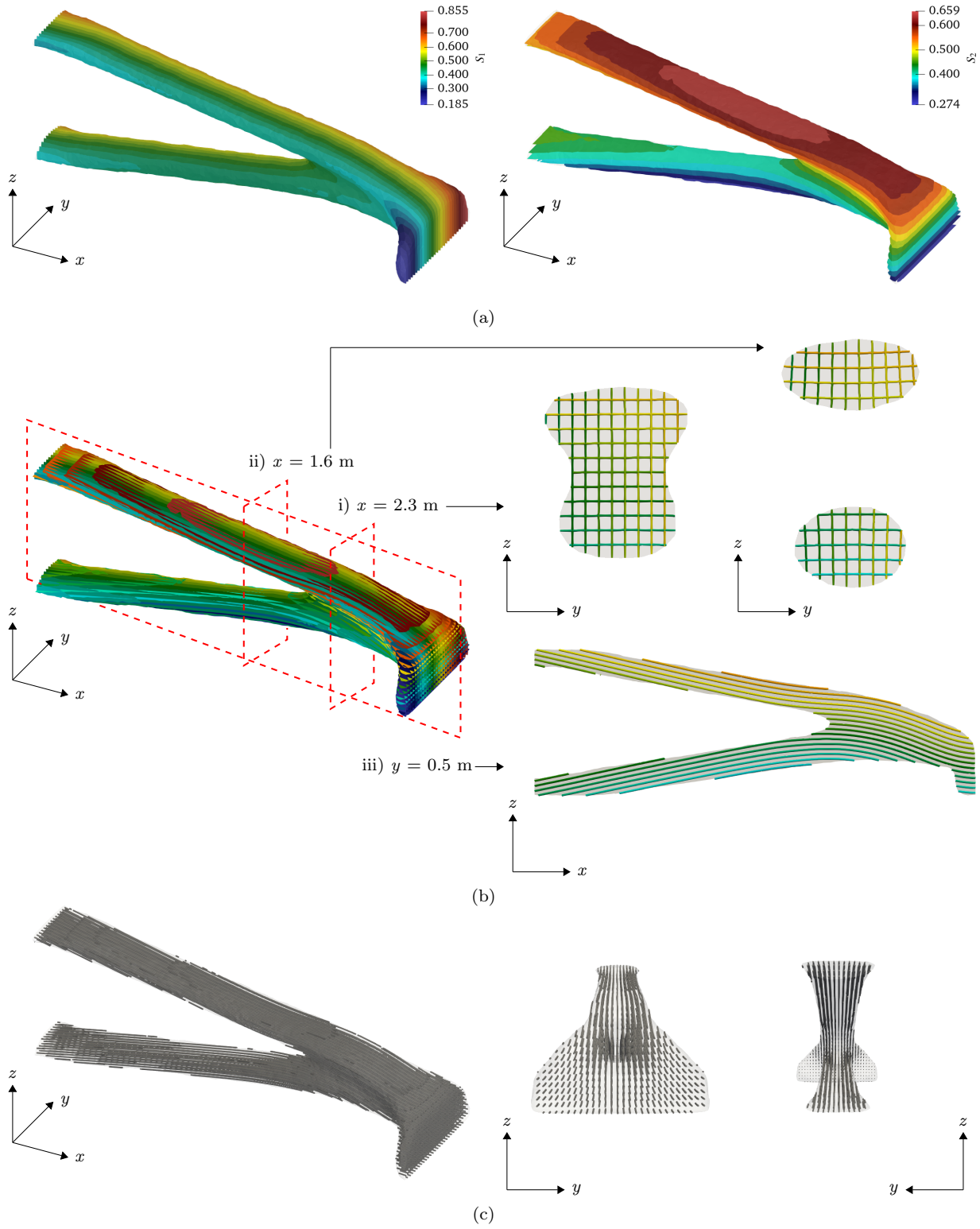


Figure 5.10: Fibre path generation: (a) the isosurfaces (b) the overlapped isosurfaces, the cross section of the overlapped isosurfaces at i) $x = 2.3$ m , ii) $x = 1.6$ m and iii) $y = 0.5$ m (c) the reconstructed fibres (Note that the numbers of isosurfaces extracted from S_1 and S_2 are chosen to be 30 and 16 respectively instead of being evaluated by Eq. (3.19) and Eq. (3.21) for a better visualisation)

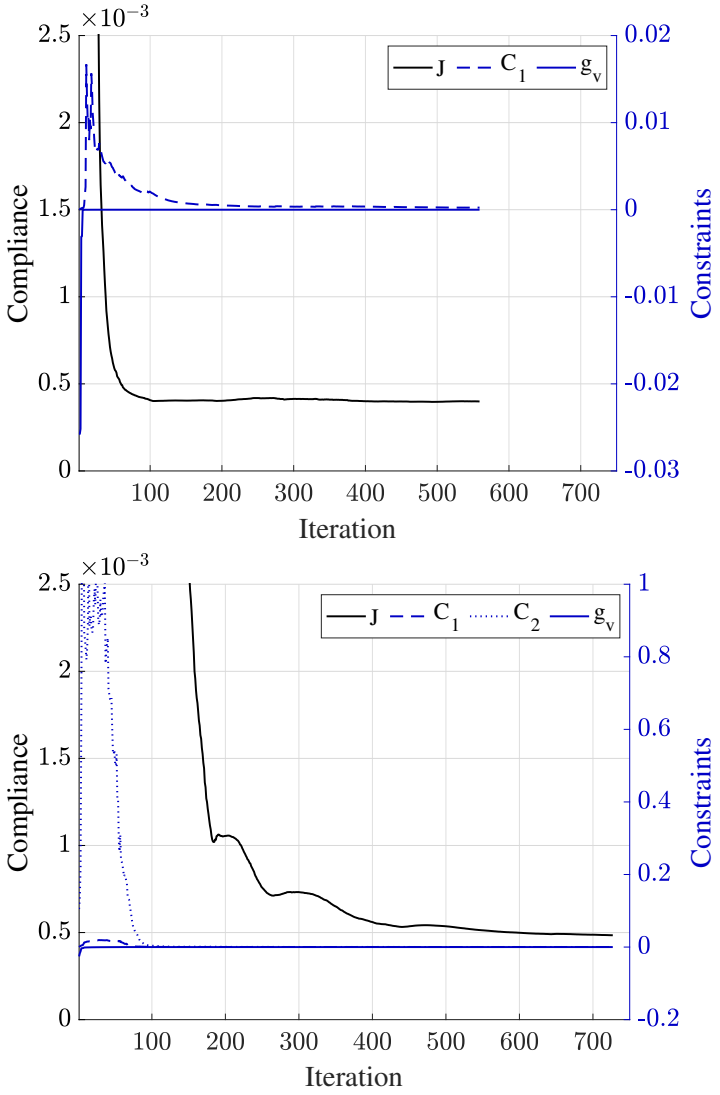


Figure 5.11: The convergence plots of the continuity case (top) and fibre path generation case (bottom)

while minimising the objective. It also reflects on the performance in terms of the compliance. The comparison of compliance shown in Tab. 5.3 indicates that the compliance increases as the number of the manufacturing constraints increases. Although the decrease in compliance is 35.69% in the continuity case and 64.65% in the fibre path generation case, compared to the spatially-optimised case, the constraints successfully avoid the manufacturing issues in the previous discussion such as sharp fibre turns and neglected variation of fibre volume fraction. Despite the compliance of the cases with manufacturing constraints being higher than the spatially-optimised case, they are still lower than the unidirectional case. This illustrates that although the variation of the fibre orientation is limited by the manufacturing constraints and the fibre volume fraction is lower at some part of the structure to fulfil them, the design from the present approach has a better performance than the unidirectional case in terms of the compliance when the manufacturability is ensured.

5.2 Twisted and Compressed Column

The optimisation of a twisted and compressed column problem is presented in this section. The problem setting is focused on the usage of the continuous fibre solely to demonstrate the ability of the developed framework to handle multiple loading condition, and the majority of the discussion is about the topology, the fibre orientation and the role of the manufacturing constraints.

5.2.1 Problem Setup

The design domain of the column is shown in Fig. 5.12. Uniform forces, $\boldsymbol{f} = 1\,\mathrm{N\,m^{-2}}$, are applied to the middle square on the top surface as shown to compress and twist the column. A Dirichlet boundary condition is applied on the bottom surface where $x = 0\,\mathrm{m}$. The design domain is discretised into 245,832 elements using the same mesh size of $1/30\,\mathrm{m}$ as determined from the mesh convergence study in the last example. The penalisation factor is set to 3. The regularisation length scale of the Helmholtz filter radius, r_h, is equal to the mesh size to capture small details whilst reducing the intermediate pseudo-density. The boundary length scale for the Robin boundary condition, r_b, to solve the Helmholtz-type filter is equal to the filter radius. The initial guesses and material properties are summarised in Tab. 5.4.

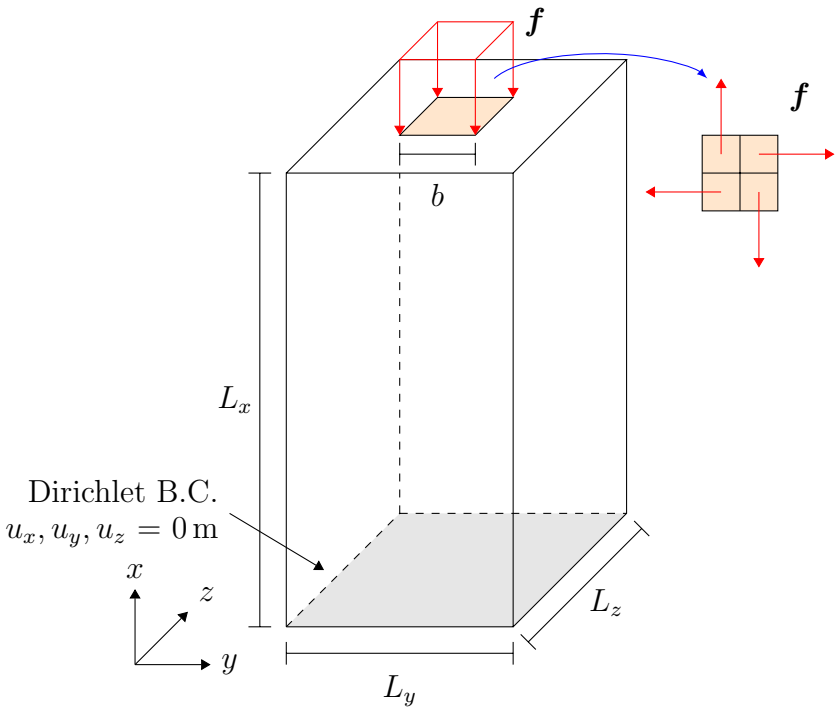


Figure 5.12: The design domain and the boundary condition of the twisted and compressed column

5.2.2 Design without Manufacturing Constraints

The manufacturing constraints, C_1 and C_2, are disabled in the results presented in this section. The optimisation required 152 iterations before meeting the termination criteria (see Fig. 5.13). The optimised design for the twisted and compressed column is shown in Fig. 5.14. The topology forms a hollow column with a slightly twisted layout due to the compressive and torsional loading condition. The fibre volume fraction is pushed to its upper bound to achieve the minimum compliance. The fibre path generated by randomly seeded streamlines shows a clockwise spiral from the top to the bottom. The curvature of the fibre path is greater close to the top as the width of the column become smaller. The twisted shape of the topology matches the spiral can also be observed. From the perspective of manufacturing, the inconsistent curvature of the fibre path with a constant fibre volume fraction may lead to non-realistic conservation of mass if the fibres are continuous and gaps between fibre paths are not allowed to be filled by short fibres. The spiral fibre orientation is fundamentally difficult to fabricate using the technology of 3D printing due to the concept of layer stacking in 3D printing. An example illustrated in Fig. 5.15 shows that a flipped over build plane is needed to deposit the fibre bundles. Hence,

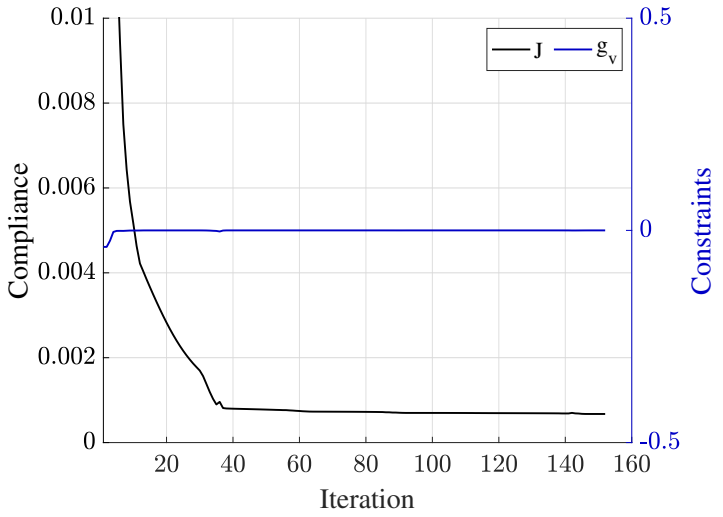
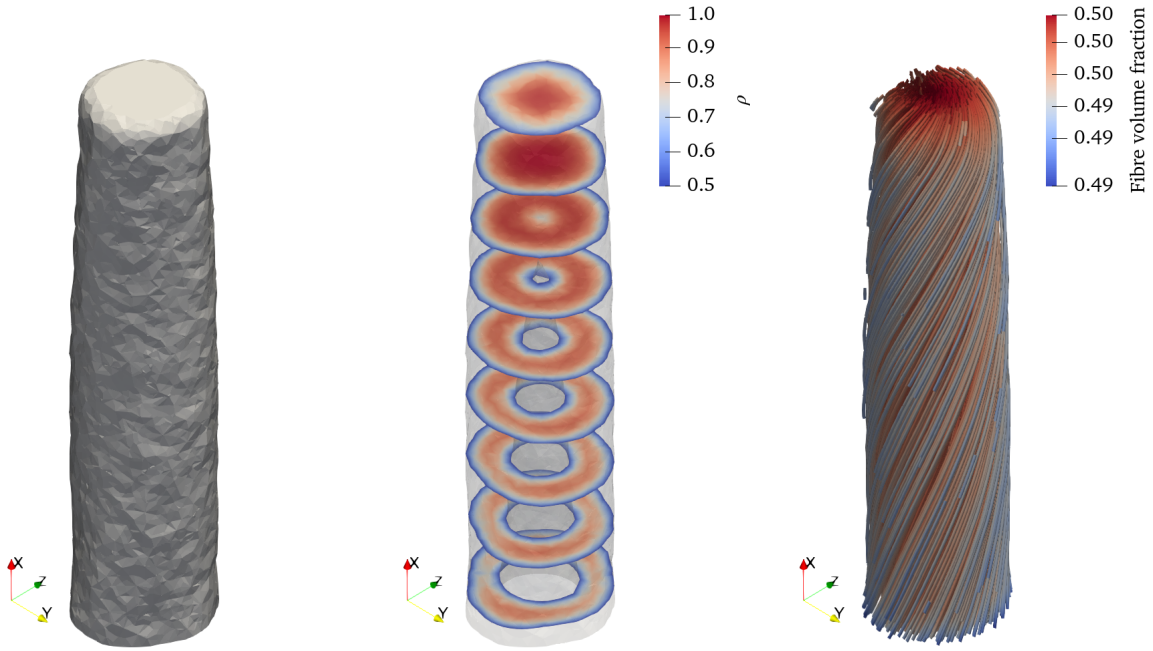


Figure 5.13: The convergence plot of the twisted and compressed column optimisation



(a) (b) (c)

Figure 5.14: The optimised design of the column without manufacturing constraints: (a) the topology (b) the slices of the topology (c) the fibre path



Figure 5.15: The build up plane example for the twisted and compressed column. Note that the fibre paths demonstrated are using streamlines seeded along the line between $(0, 0, 0.5)$ and $(0, 1, 0.5)$.

Table 5.4: The problem setup of the twisted and compressed column

Mesh	
Element	3D tetrahedral
L_x	2 m
L_y	1 m
L_z	1 m
b	0.2 m
Element size	1/30 m
Number of elements	245,832
Number of nodes	45,183
Number of design variables	316,281
Optimisation	
r_h (Helmholtz filter radius)	1/30 m
r_b (Helmholtz filter boundary radius)	1/30 m
p (SIMP parameter)	3
V_0 (target volume)	15%
Initial guesses	
ρ	0.12
(U_x, U_y, U_z)	(1,0,0)
V_f	0.5
S_1	y
S_2	z
Material properties	
E_f	200 Pa
E_m	10 Pa
ν_f	0.3
ν_m	0.3

the toolpath planing to avoid collision between deposited fibres, support materials and the print head will be very challenging. It may be more adequate to fabricate this design using filament winding technique. Although the difficulty may originate from the problem definition, it is still worth enabling the manufacturing constraints to demonstrate how they work to improve the manufacturability.

5.2.3 Design with Manufacturing Constraints

The manufacturing constraints, C_1 and C_2, are enabled in the results presented in this section. The optimisation required 302 iterations before meeting termination criteria (see Fig. 5.16) which is almost twice as long as than the optimisation without manufacturing constraints.

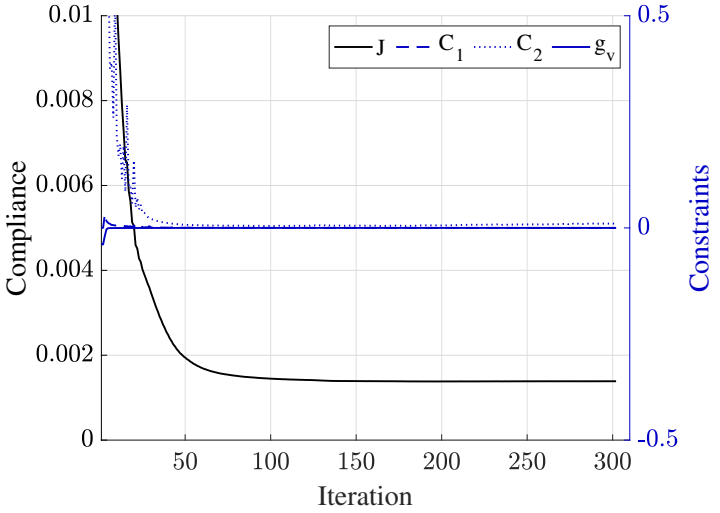


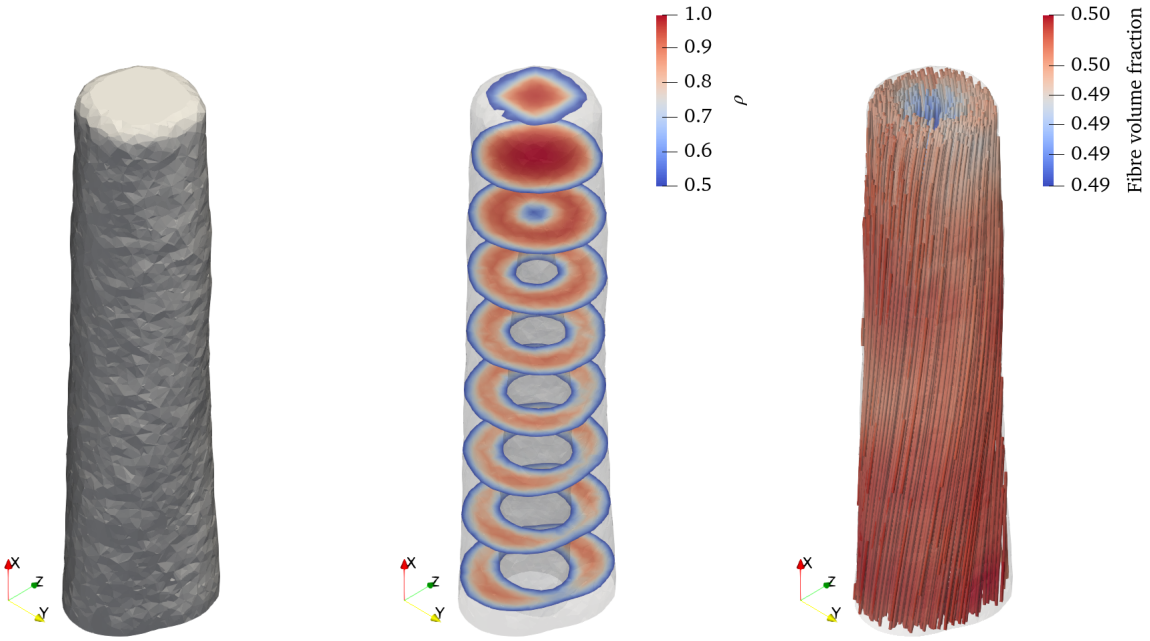
Figure 5.16: The convergence plot of the twisted and compressed column optimisation with manufacturing constraint

The optimised column with manufacturing constraints is illustrated in Fig. 5.17. The topology keeps the same pattern of forming a twisted hollow column. The fibre path generated using the streamlines shows that the curvature of the fibre path is lower whilst the fibre volume fraction stays approximately the same, compared to the design without the manufacturing constraints.

The isosurfaces of the scalar fields illustrated in Fig. 5.18a and Fig. 5.18b align with the fibre orientation in Fig. 5.17c shows that the cross product of the scalar fields aligns with the fibre orientation. By overlapping the isosurfaces and extracting the intersection curves, the fibre path is generated as illustrated in Fig. 5.18c.

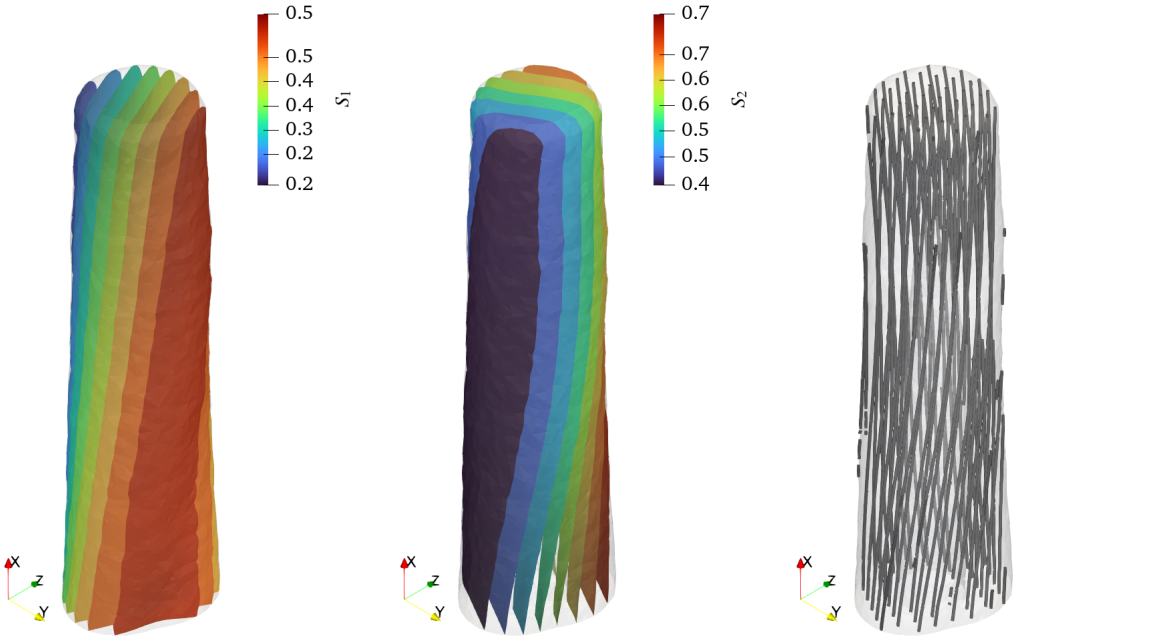
The curvature of the fibre path close to the top does not increase, indicating that the manufacturing constraints effectively ensure the continuity of the fibres and conservation of fibre mass. The curvature of the twisted fibre path is lower due to the limited variation in fibre orientation under the tight constraints of orthogonality and aspect ratio compared to the design without the manufacturing constraints. This reduces the difficulty of planning the toolpaths since the isosurfaces remain in planes without flipping over (see Fig. 5.18.a and Fig. 5.18.b), indicating an improvement in manufacturability.

The compliance comparison shown in Tab. 5.5 indicates that the compliance of the case when the manufacturing constraints are enabled is 106% higher. This shows a significant compromise between structural performance and manufacturability and that this can be quantified.



(a) (b) (c)

Figure 5.17: The optimised design of the column with manufacturing constraints: (a) the topology (b) the slices of the topology (c) the fibre path



(a) (b) (c)

Figure 5.18: The isosurfaces of (a) S_1 and (b) S_2; (c) The fibre paths extracted by the intersection curves if the isosurfaces

Table 5.5: The comparison of the compliance of the twisted and compressed column

Manufacturing constraints	Compliance (N m)
Disabled	6.74×10^{-4}
Enabled	1.39×10^{-3}

However, it is important to note that the non-realistic conservation of mass due to the over-estimated fibre volume fraction may also result in an over-estimated compliance.

5.3 L-shape Beam

The optimisation of a L-shape beam is presented in this section to demonstrate the ability of the developed framework to handle not only multiple loading condition but also a more complex geometry.

5.3.1 Problem Setup

The design domain of the L-shape beam is illustrated in Fig. 5.19. A uniform force, $\boldsymbol{f} = 1\,\mathrm{N\,m^{-2}}$, is applied to the middle rectangle area on the surface where $x = L_x + L_y$ as shown, resulting in torsion loading on the cylinder (region 1) and bending loading on the cuboid (region 2). A Dirichlet boundary condition is applied on the bottom-left surface where $z = L_z + L'_z$. The design domain is discretised into 346,272 elements using the same mesh size of $1/30\,\mathrm{m}$ as the conclusion from the mesh convergence study in the last example. The penalisation factor is set to 3. The regularisation length scale of the Helmholtz filter radius, r_h, is equal to the mesh size to capture small details whilst reducing the intermediate pseudo-density. The boundary length scale for the Robin boundary condition, r_b, to solve the Helmholtz-type filter is equal to the filter radius. The initial guesses and material properties are summarised in Tab. 5.6

5.3.2 Design without Manufacturing Constraints

The manufacturing constraints, C_1 and C_2, are disabled in the results presented in this section. The optimisation required 138 iterations before meeting the termination criteria (see Fig. 5.20). The optimised L-shape beam illustrated in Fig. 5.21 demonstrates an effective response to the

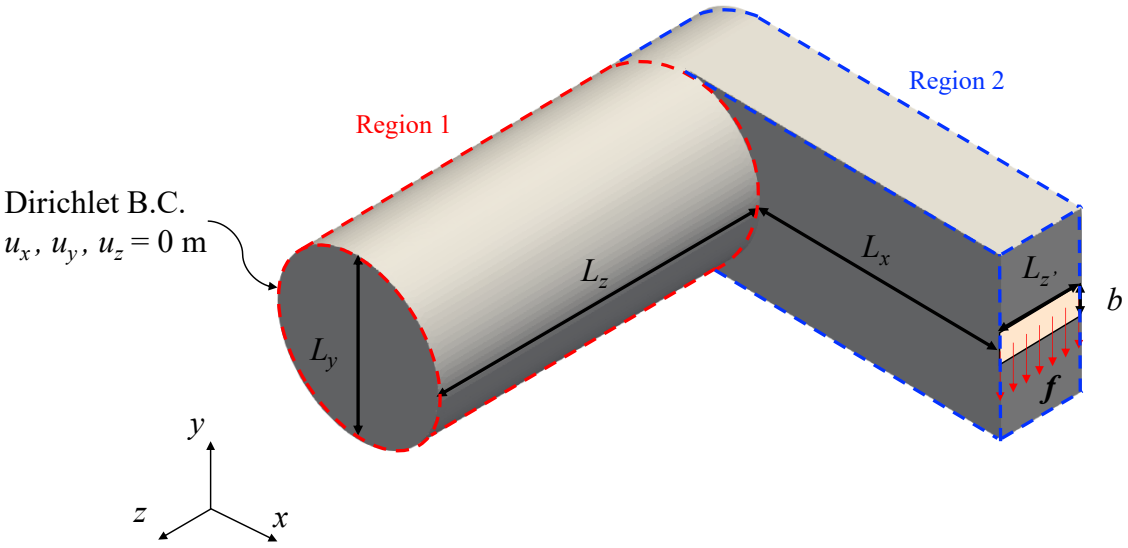


Figure 5.19: The design domain of the L-shape beam

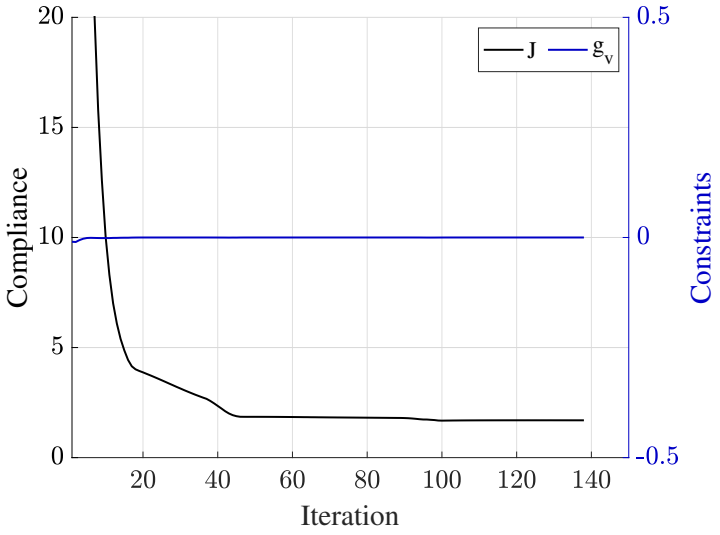


Figure 5.20: The convergence plot of the L-shape beam optimisation without the manufacturing constraints

loading conditions. The topology in the cuboid (region 2) is composed of two members to withstand the bending load. In the cylinder (region 1), to withstand torsional loading, the materials are distributed close to the boundary, forming a shell structure with several holes. When viewed in the xz plane from the top where $y > 0$, three major members at each side align with each other, following the maximum principal stress direction and the support members connect the major members orthogonally following the minimum principal stress direction (see Fig. 5.23). Note that the alignment of the fibre orientation and the principal stresses is opposite for the bottom half of the model.

Tiny holes located at the cylinder (region 1) can be observed from the view of the yz plane in Fig. 5.21b.i due to the Robin boundary condition of the Helmholtz filter and insufficient penalisation. The maximum permitted value of the pseudo-density at the boundary is 0.5 under the filter boundary radius setup in this case. This discourages material distribution close to the boundary; however, in the torsion loading condition, distributing materials closer to the boundary results in a stiffer design. Consequently, a competition between distributing and removing materials arises, leaving severe intermediate pseudo-density due to insufficient penalisation. Using the continuation penalisation and threshold projection are possible approaches to address this issue.

The fibre orientation shown in Fig. 5.22 mostly follows the boundary of the topology apart from the support members in the cylinder region. The fibre orientation exhibits a smooth transition at the connected region of the cuboid (region 2) and the cylinder (region 1), due to the implementation of the Helmholtz filter. However, at the regions on the cylinder (region 1) where the fibre orientation changes direction (see Fig. 5.22b.i and Fig. 5.22d.i), terminated fibres and resin-rich areas may exist, increasing the potential for composite failure speculation. It is observed that the randomly seeded streamlines cannot accurately represent the fibre volume fraction when it is pushed to the upper bound to achieve the minimum compliance design.

5.3.3 Design with Manufacturing Constraints

The manufacturing constraints, C_1 and C_2, are enabled in the results presented in this section. The optimisation required 262 iterations before meeting the termination criteria (see Fig. 5.24).

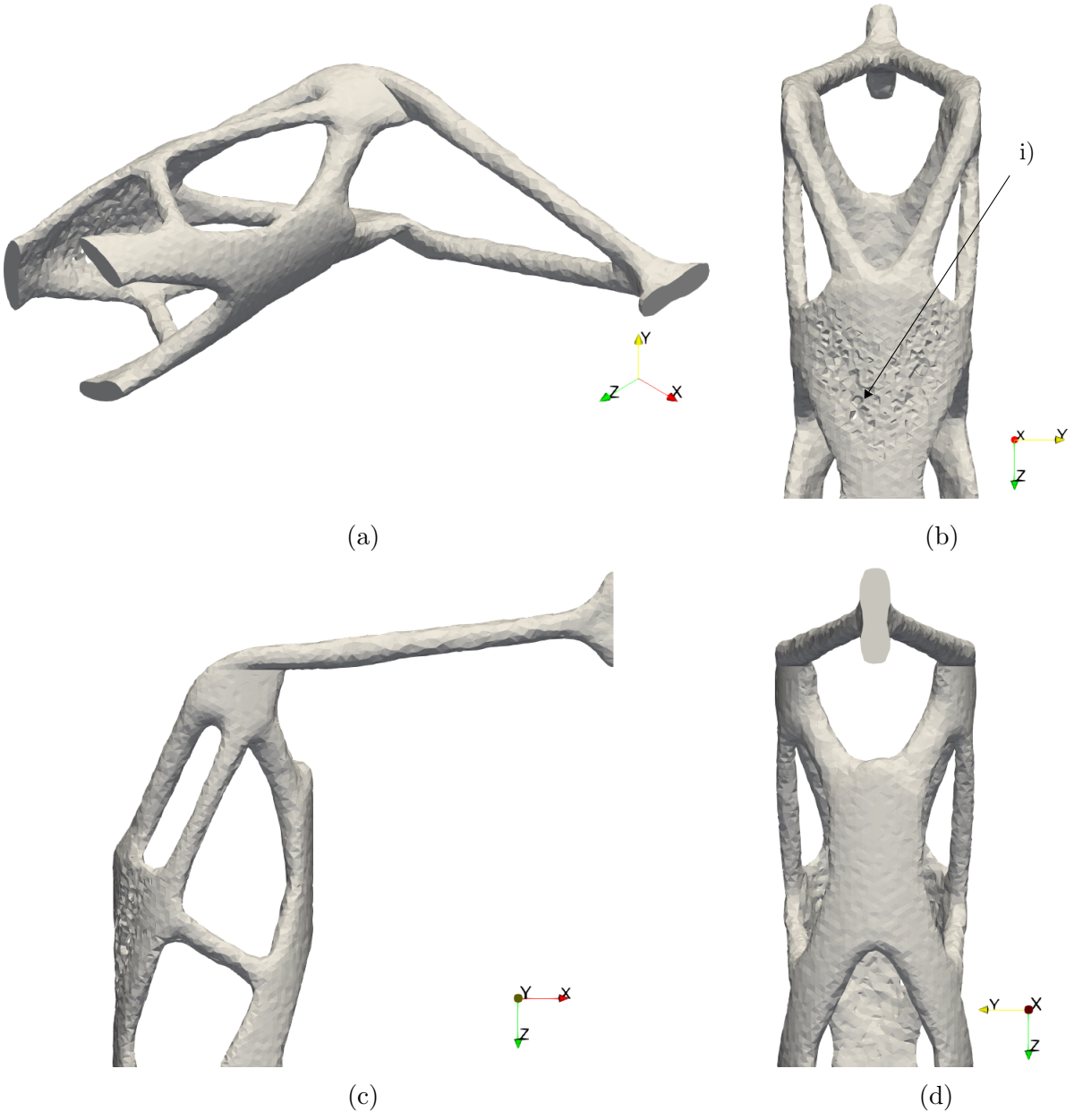


Figure 5.21: The optimised topology of the L-shape beam without manufacturing constraints: (a) The isometric view (b) The orthogonal view on the $y-z$ plane (c) The orthogonal view on the $x-y$ plane (c) The orthogonal view on the $z-y$ plane

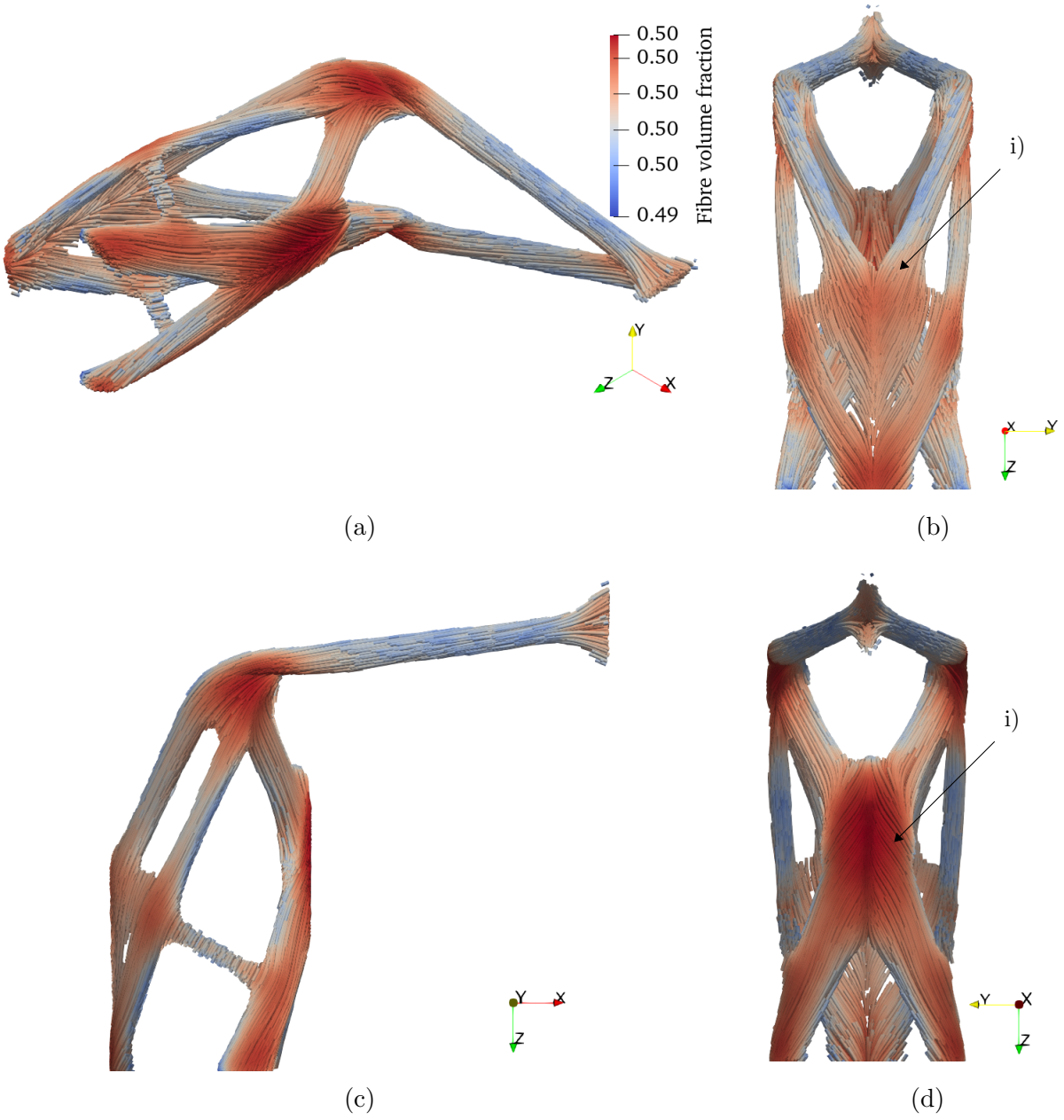
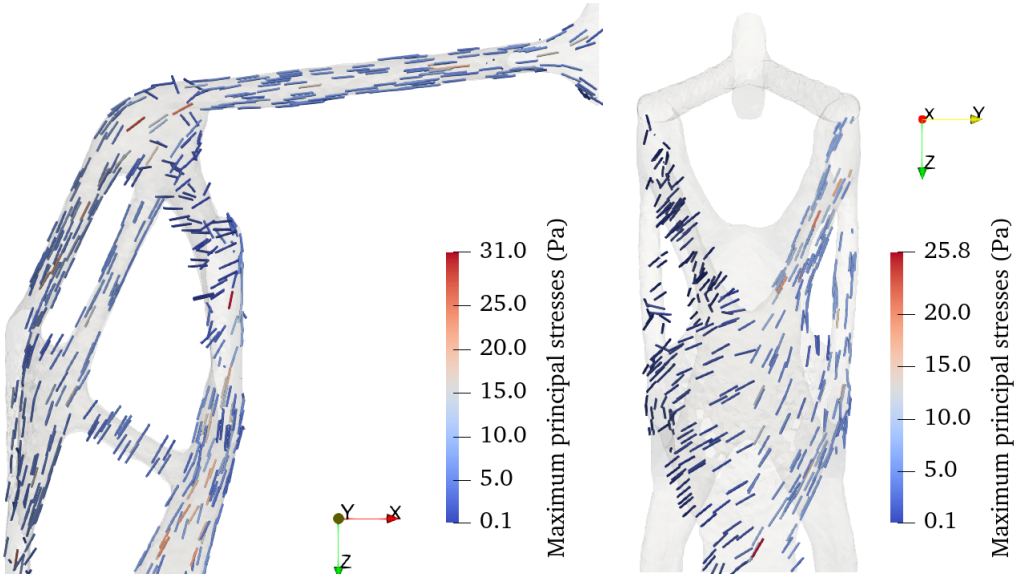
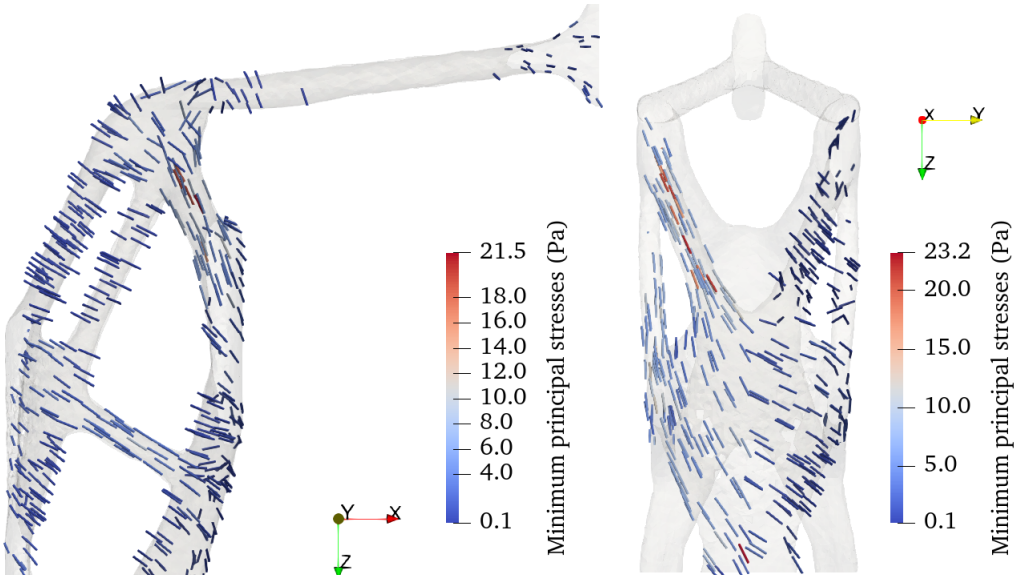


Figure 5.22: The optimised fibre orientation of the L-shape structure without manufacturing constraints: (a) The isometric view (b) The orthogonal view on the $x-y$ plane (c) The orthogonal view on the $y-z$ plane



(a)



(b)

Figure 5.23: The principal stresses of the L-shape structure without manufacturing constraints: (a) The maximum principal stress (b) The minimum principal stresses

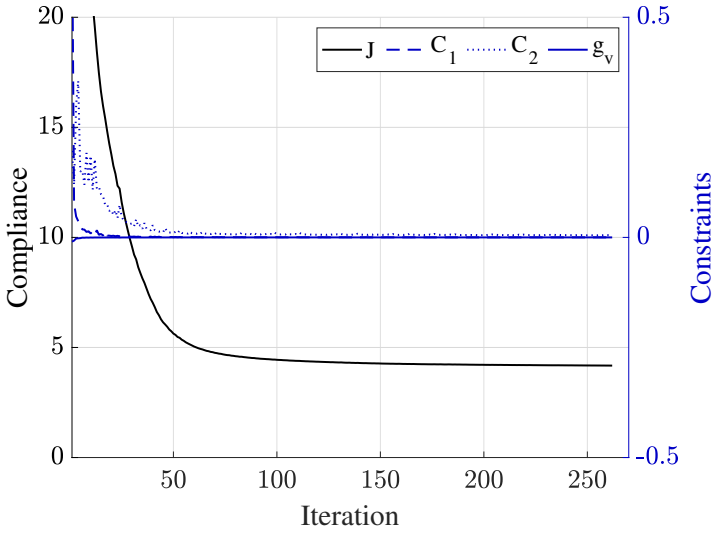
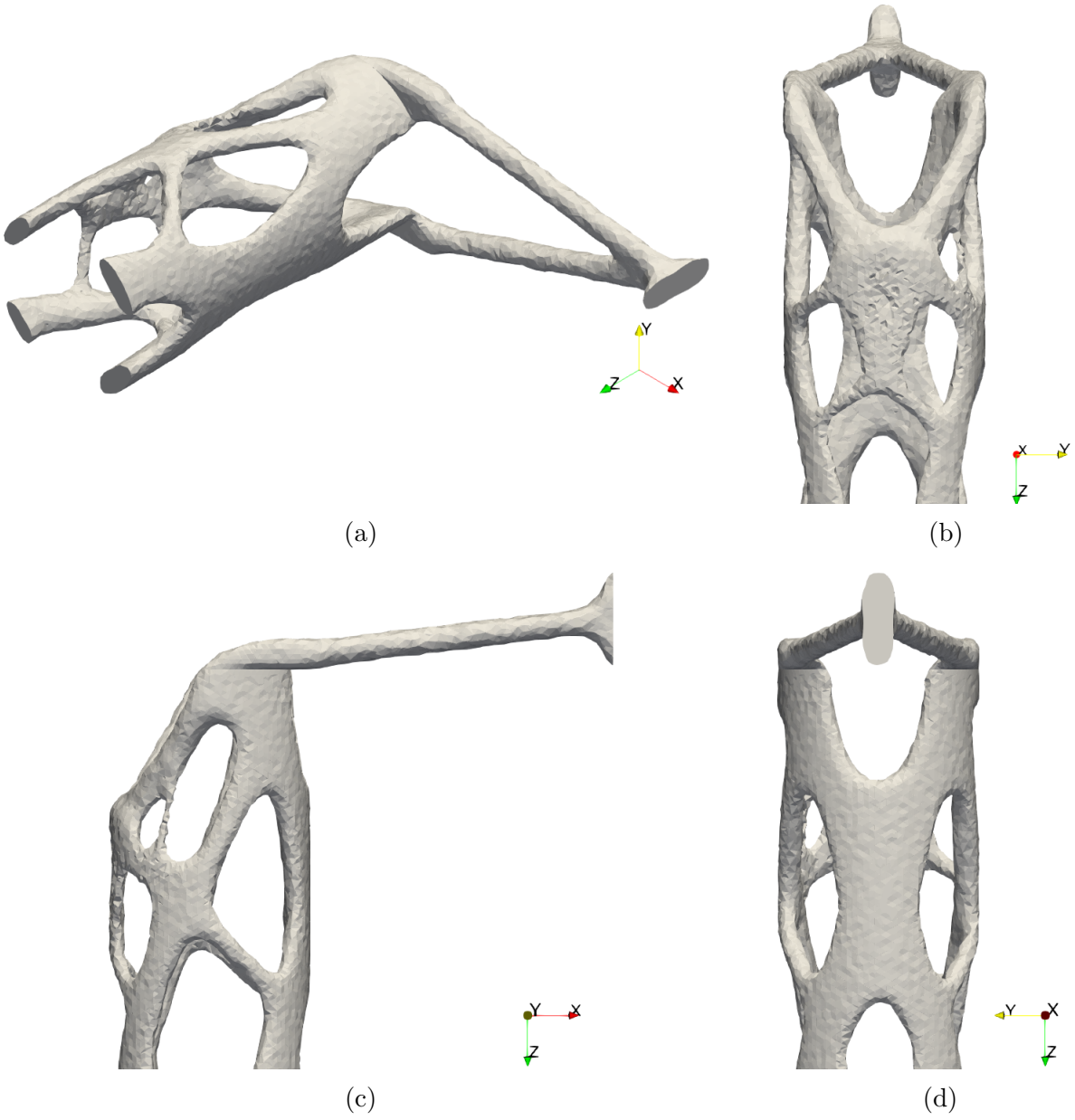


Figure 5.24: The convergence plot of the L-shape beam optimisation with the manufacturing constraints

The design with manufacturing constraints is illustrated in Fig. 5.25. The optimal topology is similar to the design without the manufacturing constraints, except that more holes are generated in the cylinder (region 1). The bottom of the shell splits into two members with support members attached, and the top of the shell moves further in the negative z direction compared to the design without manufacturing constraints (see Fig. 5.25b). The variation of the structure layout in x and y direction is not as much as the design without manufacturing constraints due to the constrained fibre orientation.

The optimal fibre orientation and fibre volume fraction is shown in Fig. 5.26. The diverged fibre orientation close to the region where the loading is applied, is replaced by straight fibres with a maximum fibre content in this case. The fibre orientation shows a smooth turn with a corresponding fibre volume fraction variation at the transition region between the cuboid (region 2) and cylinder (region 1). The intensity of the divergence and convergence trends of fibre orientation in the cylinder region is much less compared to the design without manufacturing constraints. This coincides with the variation of the structure layout. Although the fibre orientation only has a very slight variation, a reasonable fibre volume fraction variation can still be observed.

The fibre volume fraction is pushed to its upper bound almost everywhere in the design domain to achieve the minimum compliance design. This shows that maximising the fibre content is



(a) (b)

(c) (d)

Figure 5.25: The optimised fibre orientation of the L-shape structure with manufacturing constraints: (a) The isometric view (b) The orthogonal view on the $x-y$ plane (c) The orthogonal view on the $y-z$ plane

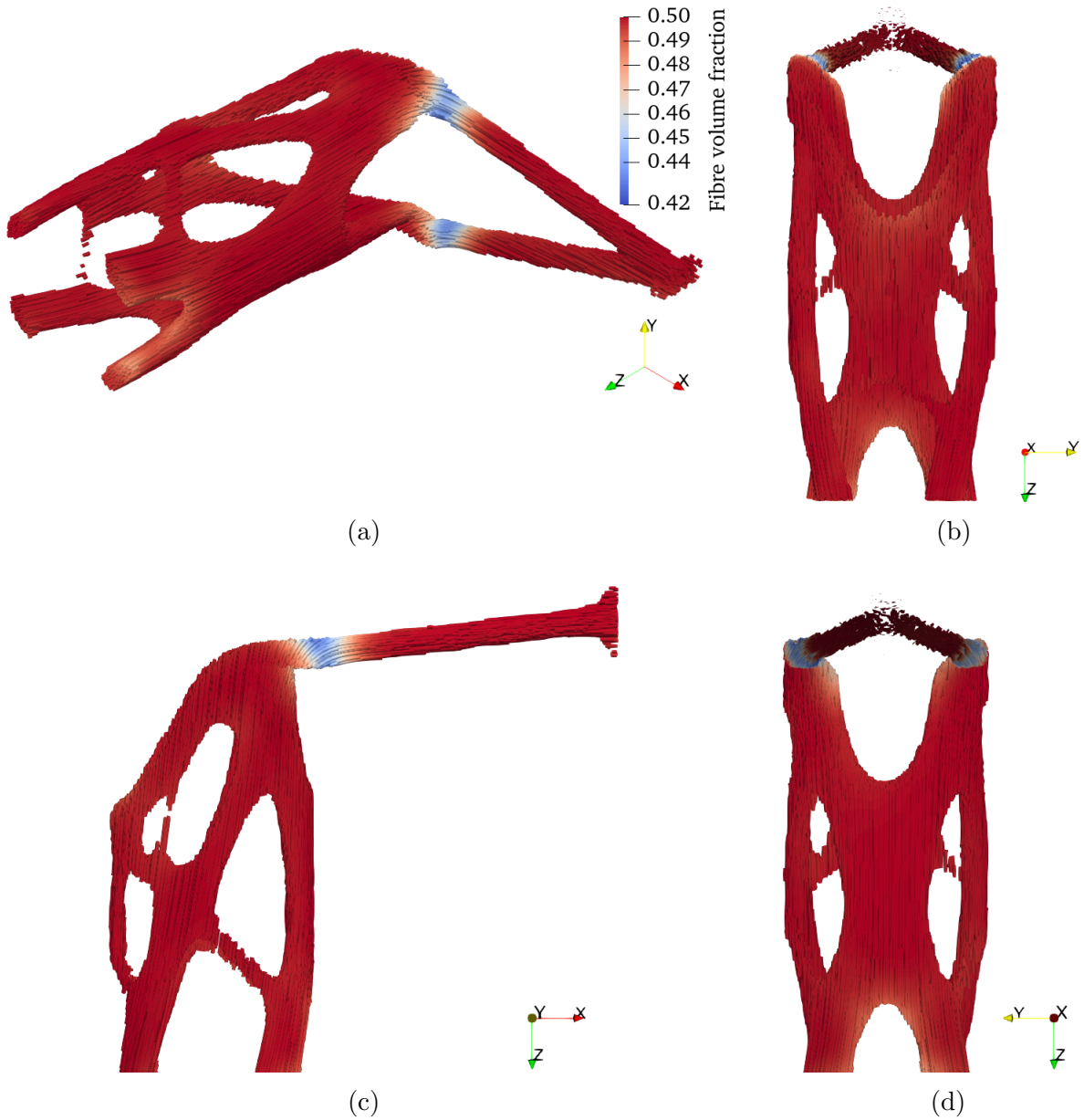
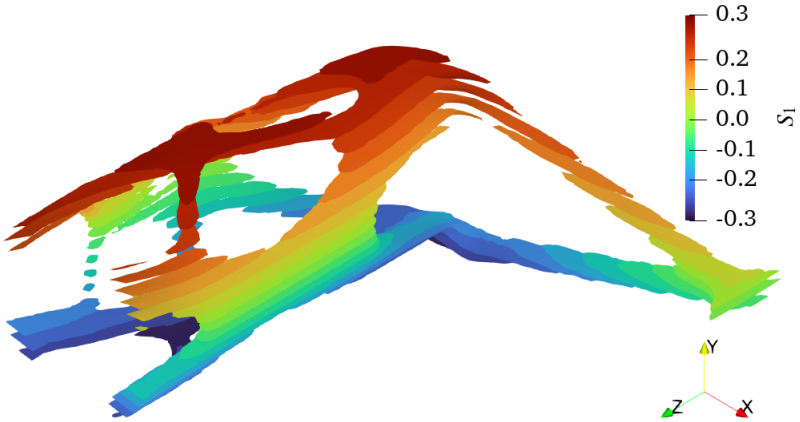
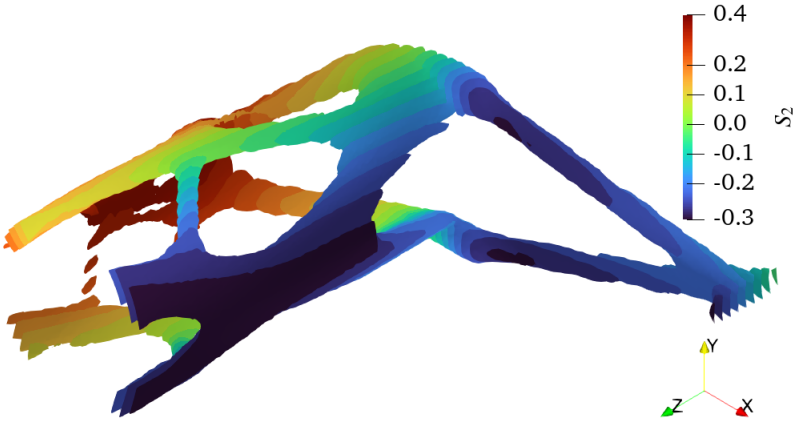


Figure 5.26: The optimised fibre orientation of the L-shape structure with manufacturing constraints: (a) The isometric view (b) The orthogonal view on the $x-y$ plane (c) The orthogonal view on the $y-z$ plane



(a)



(b)

Figure 5.27: The isosurfaces extracted from (a) S_1 and (b) S_2

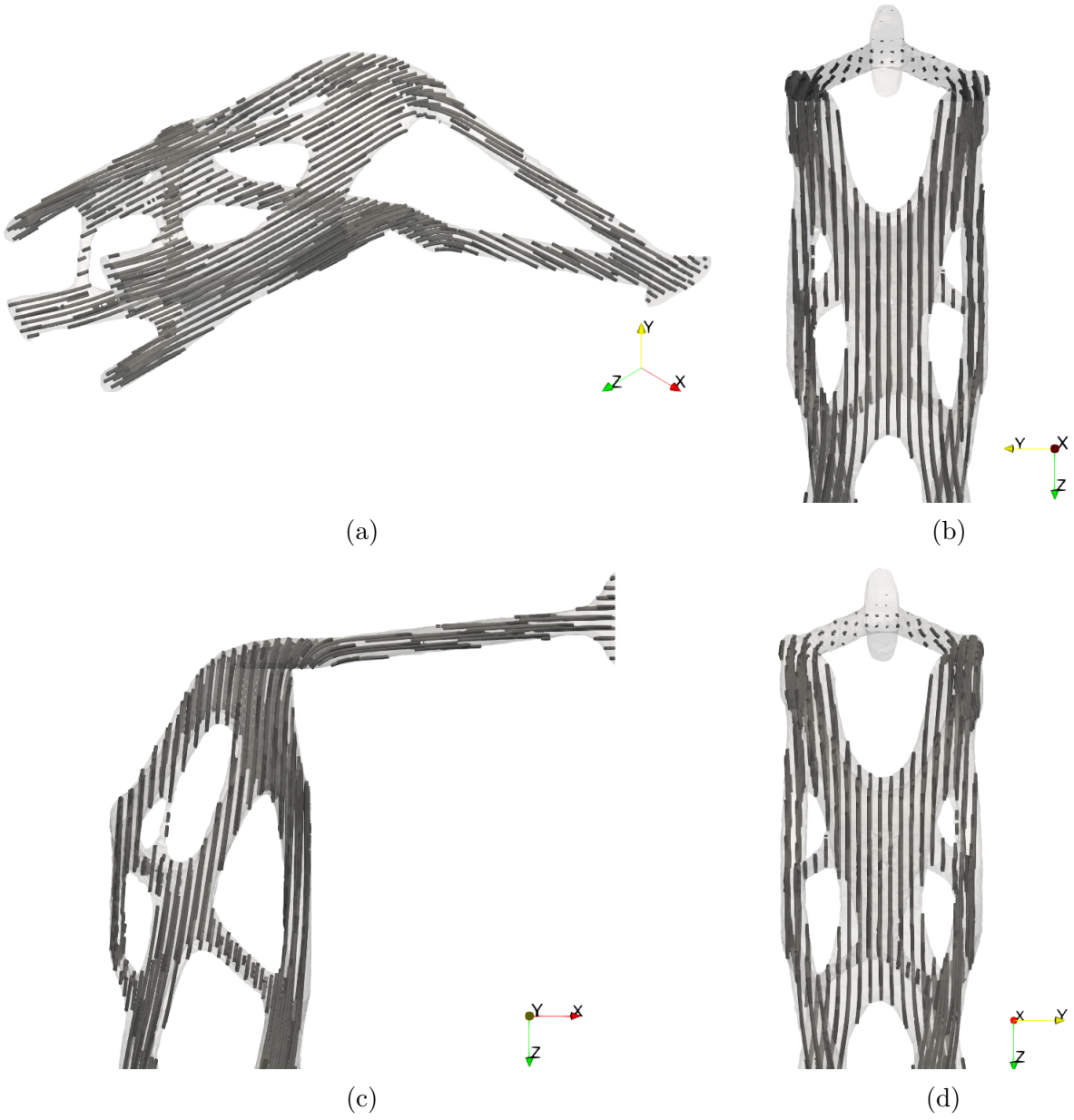


Figure 5.28: The fibre path extracted from the intersection curves of S_1 and S_2

more important than utilising the anisotropic characteristics through varying the fibre orientation in this case.

The isosurfaces extracted from the scalar fields demonstrated in Fig. 5.27 coincide with the optimal fibre orientation. They also show promising manufacturability if the xz plane is chosen as the build up plane. By overlapping the isosurfaces and extracting the intersection curves, the fibre path is generated as shown in Fig. 5.28. The fibre path coincides with the fibre orientation visualised using randomly seeded streamlines in Fig. 5.26 and more importantly, the fibre path reflects the fibre volume fraction variation through the distances between the isosurfaces.

The compliance of the design with manufacturing constraints is 141% higher than the design without manufacturing constraints (see Tab. 5.7). This shows a compromise in term of stiffness when accounting for manufacturability.

5.4 Buckling Analysis of Optimal Design

As noted in the literature review, buckling failure may occur in optimal designs when slender and compressive structural members exist. Buckling analyses with regards to the optimised twisted and compressed column and L-shape beam are presented.

The first buckling modes of the designs are illustrated in Fig. 5.29. For the twisted and compressed column, the optimised design consists of a slender column under axial compression, resulting in a flexural buckling. The optimised design of the L-shape beam exhibits two slender members at the cuboid (region 1) under bending. More precisely, the upper member is in tension and the bottom member is compressed, resulting in a flexural-torsional buckling. The buckling load factors are 0.99 and 0.5, respectively, indicating that a significant potential of buckling failure.

5.5 Summary

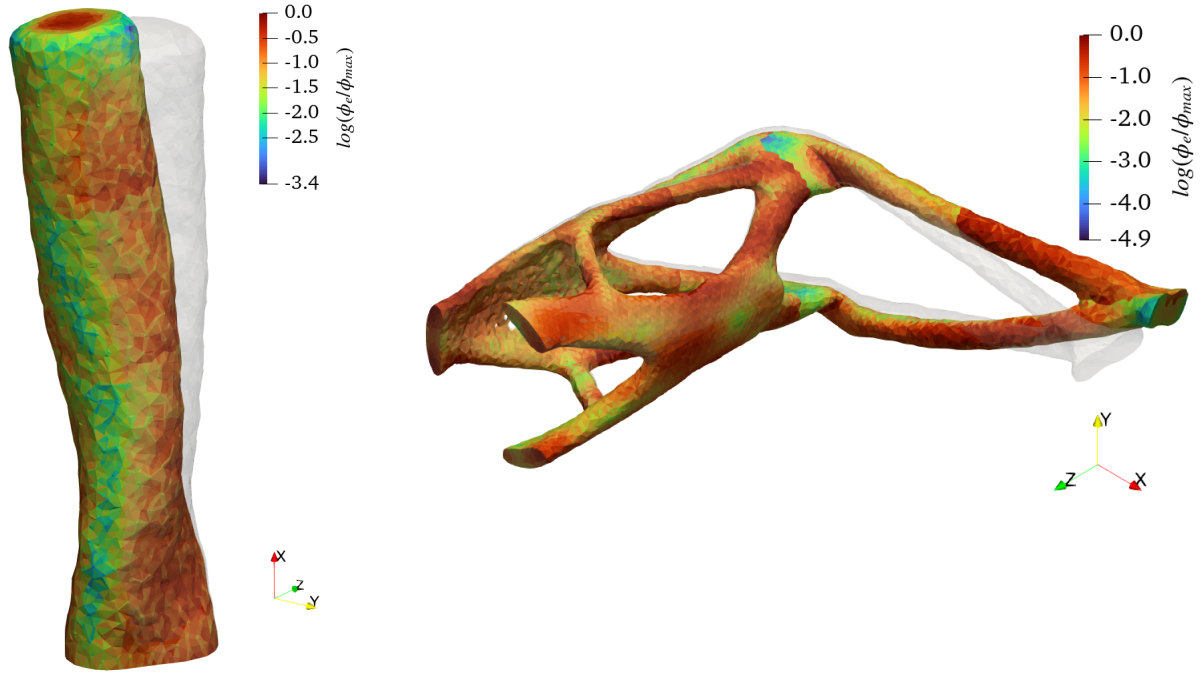
This chapter demonstrated the optimised designs combining topology and fibre orientation optimisation for the cantilever beam, twisted and compressed column and L-shape beam in 3D.

Table 5.6: The problem setup of the L-shape beam

Mesh	
Element	3D tetrahedral
L_x	1.5 m
L_y	1 m
L_z	2 m
L'_z	0.5 m
L_b	0.2 m
Element size	1/30 m
Number of elements	346,272
Number of nodes	63,225
Number of design variables	442,575
Optimisation	
r_h (Helmholtz filter radius)	1/30 m
r_b (Helmholtz filter boundary radius)	1/30 m
p (SIMP parameter)	3
V_0 (target volume)	12%
Initial guesses	
ρ	0.12
(U_x, U_y, U_z)	(-1,0,0) if $z \leq 0.5$ (0,0,1) if $z > 0.5$
V_f	0.5
S_1	y
S_2	-z if $z \leq 0.5$ -x if $z > 0.5$
Material properties	
E_f	200 Pa
E_m	10 Pa
ν_f	0.3
ν_m	0.3

Table 5.7: The comparison of the compliance of the twisted and compressed column

Manufacturing constraints	Compliance (N m)
Disabled	1.66
Enabled	4.01



(a) (b)

Figure 5.29: The first buckling mode of the optimised designs (Note that the buckling modes are coloured by the strain energy density, ϕ_e, using the scale of $\log(\phi_e/\phi_{max})$)

In the cantilever beam example, the compliance of the spatially-optimised case is 1.65 times smaller than the isotropic case which indicates the effectiveness of the continuous fibres against the short random-oriented fibres using the same amount of fibre content. The fibre path generation case successfully ensures the manufacturability though the continuous fibre path and controllable distances between the iso-surfaces. Although there is 65% compromise in compliance compared to the spatially-optimised case, the structural performance is still better than the unidirectional case.

The twisted and compressed column example shows the developed framework is capable to deal with the multiple loading condition (torsion and compression). The design without the manufacturing constraints has manufacturing issues originate from the problem itself; however, the design with the manufacturing constraints significantly improve the manufacturability of fabricating through the 3D printing technique.

The L-shape beam example illustrates the developed framework's ability to handle not only the multiple loading condition but also the complex geometry. The optimised designs demonstrate effective topology layout to withstand different loading condition in the corresponding regions.

The manufacturability is also ensured in the design with the manufacturing constraints.

One common observation from the optimisation results presented in this chapter is that the optimisation iterations become longer when the manufacturing constraints are enabled. Although another observation in common is that the compromise in the structural performance always exists when accounting for the manufacturability, the promising manufacturability brings the designs closer to the practical implementation.

The buckling analysis of the optimised twisted and compressed column and L-shape beam clearly demonstrates the potential of the buckling failure in these topological optimised structures is high which leads to the methodology of design for the buckling resistance presented in the next chapter.

Chapter 6

Design for Buckling Resistance

This chapter contains a detail breakdown of the methodology of design for buckling resistance. Linear buckling analysis for optimisation is introduced, and strategies to avoid mode switching and spurious modes are detailed. Sensitivities with respect to buckling load factor are derived. Optimisation formulations are presented to maximise buckling resistance while ensuring manufacturability and meeting volume and compliance constraints.

6.1 Buckling Analysis

To account for buckling resistance within the optimisation process, stability analysis for buckling is required for each optimisation iteration. To formulate the buckling problem, the Green-Lagrange strain is introduced to capture the geometrically nonlinearity such that

$$\begin{aligned} e_{ij}(\boldsymbol{u}) =& \frac{1}{2}\left(\frac{\partial u_i}{\partial x_j} + \frac{\partial u_j}{\partial x_i} + \frac{\partial u_k}{\partial x_j}\frac{\partial u_k}{\partial x_i}\right) \\ =& \epsilon(\boldsymbol{u}) + \frac{1}{2}\nabla \boldsymbol{u}^T \nabla \boldsymbol{u} \end{aligned} \tag{6.1}$$

where $\boldsymbol{u}$ denotes the displacement field, ϵ denotes the small strain introduced in Eq. 3.2. The stability analysis aims to find a equilibrium displacement field as a function of a loading parameter, λ. The potential energy functional of a loaded structure which consists of the strain

energy and the work of the loading reads

$$\Pi = \int_{\Omega} \frac{1}{2} e(\boldsymbol{u}) : \boldsymbol{K_e} : e(\boldsymbol{v}) dx - \int_{\Gamma} \boldsymbol{T}(\lambda) \cdot \boldsymbol{u} dS \tag{6.2}$$

where Π denotes the potential energy, $\boldsymbol{K}_e$ denotes the elemental stiffness tensor and $\boldsymbol{T}(\lambda)$ denotes the external forces. The condition of the equilibrium equation requires the first variation of the potential energy functional to vanish such that

$$\partial_{\boldsymbol{u}} \Pi[\delta \boldsymbol{u}] = \int_{\Omega} e(\boldsymbol{u}) : \boldsymbol{K}_e : \delta e[\delta \boldsymbol{u}] dx - \int_{\Gamma} \boldsymbol{T}(\lambda) \cdot \delta \boldsymbol{u} dS = 0 \tag{6.3}$$

where $\delta \boldsymbol{u}$ is any admissible perturbation and

$$\delta e[\delta \boldsymbol{u}] = \epsilon(\delta \boldsymbol{u}) + \nabla \boldsymbol{u}^T \nabla \delta \boldsymbol{u} \tag{6.4}$$

According to the Lagrange-Dirichlet theorem, the stability conditions of an equilibrium state require the second variation of the potential energy functional to be positive such that

$$\partial_{\boldsymbol{uu}} \Pi[\delta \boldsymbol{u} \delta \boldsymbol{v}] = \int_{\Omega} \left(\delta e[\delta \boldsymbol{v}] : \boldsymbol{K}_e : \delta e[\delta \boldsymbol{u}] + e(\boldsymbol{u}) : \boldsymbol{K}_e : \delta^2 e[\delta \boldsymbol{u} \delta \boldsymbol{v}] \right) dx > 0 \tag{6.5}$$

where

$$\delta^2 e[\delta \boldsymbol{u} \delta \boldsymbol{v}] = \nabla \delta \boldsymbol{v}^T \nabla \delta \boldsymbol{u} \tag{6.6}$$

The bifurcation points are found for some bifurcation modes, $\delta \boldsymbol{u}$, and bifurcation load factors, λ, when the second variation equals to zero as

$$\int_{\Omega} \left((\epsilon(\delta \boldsymbol{v}) + \nabla \boldsymbol{u}^T \nabla \delta \boldsymbol{v}) : \boldsymbol{K}_e : (\epsilon(\delta \boldsymbol{u}) + \nabla \boldsymbol{u}^T \nabla \delta \boldsymbol{u}) + e(\boldsymbol{u}) : \boldsymbol{K}_e : \nabla \delta \boldsymbol{v}^T \nabla \delta \boldsymbol{u} \right) dx = 0 \tag{6.7}$$

In this thesis, linear buckling analysis is used to find the bifurcation points due to its efficiency compared to nonlinear buckling analysis. Linear buckling analysis finds the fundamental branch of bifurcation points under the assumption of small strain. Hence, in Eq. 6.7, the Green-Lagrange strain can be replaced by the small strain and the quadratic terms of displacements are negligible.

The pre-buckling equilibrium linear elastic problem is solved as

$$\boldsymbol{f} = \boldsymbol{K}\boldsymbol{u}_0 \tag{6.8}$$

where $\boldsymbol{f}$ denotes the applied force, $\boldsymbol{K}$ denotes the global stiffness matrix and $\boldsymbol{u}_0$ denotes the displacement field. Under the small strain assumption, when the applied force is linear to the loading factor, the displacement field is linear to the loading factor as well such that

$$\boldsymbol{u} = \lambda\boldsymbol{u}_0 \tag{6.9}$$

Substituting $\boldsymbol{u}$ with $\lambda\boldsymbol{u}_0$ and replacing the Green-Lagrange strain with small strain in Eq. 6.7 yield

$$\int_\Omega \left(\epsilon(\delta\boldsymbol{v}) : \boldsymbol{K}_e : \epsilon(\delta\boldsymbol{u}) + \lambda\epsilon(\boldsymbol{u}_0) : \boldsymbol{K}_e : \nabla\delta\boldsymbol{v}^T\nabla\delta\boldsymbol{u}\right) dx = 0 \tag{6.10}$$

Transforming the variational form into the matrix notation yields

$$\left[\boldsymbol{K} + \lambda\boldsymbol{G}(\boldsymbol{u}_0)\right]\boldsymbol{\psi} = 0 \tag{6.11}$$

where $\boldsymbol{G}(\boldsymbol{u}_0)$ denotes the global stress stiffness matrix and $\boldsymbol{\psi}$ denotes the bifurcation modes. By solving the eigenvalue problem, Eq. 6.11, a set of eigenvalues and the corresponding eigenvectors, $\{\lambda_i, \boldsymbol{\psi}_i\}$ for $i \in \gamma$, can be obtained where γ denotes the number of considered eigenpairs. The eigenpairs obtained by solving the eigenvalue problem represent the buckling load factors and the buckling modes. The positive smallest eigenvalue within the solved eigenvalues, $\lambda_c = \min_{i\in\gamma} \lambda_i$ is defined as critical buckling load factor. The structural stability can therefore be increased by maximising the critical buckling load factor.

6.2 Strategy for Mode Switching

According to Dunning et al. (2016), the effect of mode switching can be alleviated and generate smooth convergence by considering more than 10 buckling modes during the optimisation process.

To account for several buckling modes, the KS aggregation equation (Kreisselmeier and Steinhauser, 1979) is applied as

$$\mu_{KS} = \mu_1 + \frac{1}{q} \ln \left(\sum_{i \in \gamma} e^{q(\mu_i - \mu_1)} \right) \tag{6.12}$$

where $\mu_i = \frac{1}{\lambda_i}$, q denotes the aggregation parameter and μ_{KS} provides an approximation of the greatest inverse buckling load factor, $\max_{i \in \gamma} \mu_i$. As a result, an approximation for the lower-bound of the buckling load factor is naturally obtained by (6.12) so that minimising (6.12) results in the maximising the buckling resistance. It is important to note that as the aggregation parameter increases, the approximation approaches the actual critical buckling load factor.

To evaluate μ_i directly, the linear buckling problem Eq. (6.11) is re-written as

$$[\boldsymbol{G}(\boldsymbol{u}_0) + \mu_i \boldsymbol{K}]\, \boldsymbol{\psi}_i = 0 \tag{6.13}$$

6.3 Spurious Modes Reduction

For TO problems which aim to increase buckling resistance, spurious buckling modes are commonly observed at low pseudo-density regions where strain energy is predicted to be high, compared to the total strain energy, and high pseudo-density regions where the magnitude of the stresses fluctuates severely. A filter and projection method proposed by Ferrari and Sigmund (2023) is adopted to avoid the occurrence of the spurious modes. The method describes the stiffness and stress matrix using the suggested formulation from Bendsøe and Sigmund (2004). To avoid the spurious modes in the low pseudo-density regions, different projection parameters for the pseudo-density fields are used such that

$$\begin{aligned} \widehat{\boldsymbol{K}}_e &= \left[\rho_{min} + (1 - \rho_{min})\widehat{\rho}_k^p\right] \boldsymbol{K}_e(\widehat{\rho}_k, \overline{V_f}, \overline{\boldsymbol{U}}) \\ \widehat{\boldsymbol{G}}_e &= \widehat{\rho}_\sigma^p \boldsymbol{G}_e(\widehat{\rho}_\sigma, \overline{V_f}, \overline{\boldsymbol{U}}, \widehat{\sigma}) \end{aligned} \tag{6.14}$$

where $\widehat{\rho}_k$ and $\widehat{\rho}_\sigma$ is projected by

$$\widehat{\rho} = \frac{\tanh \beta\eta + \tanh \beta(\overline{\rho} - \eta)}{\tanh \beta\eta + \tanh \beta(1 - \eta)} \tag{6.15}$$

using different parameter, η_k and η_σ. Note that β and η are parameters which control the no-linearity and the threshold of the projection. To reduce the occurrence of spurious modes in solid regions where the magnitude of the stresses fluctuation is severe, the stress field used to evaluate the stress stiffness matrix is regularised by a Helmholtz PDE filter

$$-R_\sigma^2 \nabla^2 \widehat{\sigma}_j + \widehat{\sigma}_j = \widehat{\rho}_k \sigma_j \tag{6.16}$$

where R_σ denotes the stress filter radius, $\widehat{\sigma}$ denotes the filtered stress field. The original stresses, σ_j for $j \in \{1, 2, 3\}$, are multiplied by the stiffness pseudo-density, $\widehat{\rho}_k$, before the filtered stresses, $\widehat{\sigma_j}$, are solved. A homogeneous Dirichlet boundary condition is applied on the boundary of the design domain apart from the loading and supporting regions. Note that the PDE-type filter is an alternative to the original implementation using distance decaying weight filter in Ferrari and Sigmund (2023).

6.4 Sensitivity Analysis

As noted in Chapter 3, the sensitivities with respect to the compliance, volume constraint and manufacturing constraints are evaluated by the automatic differentiation method implemented using the open-source Python package dolfin-adjoint (Mitusch et al., 2019). The sensitivities with respect to the buckling load factors are evaluated by the following equations as the Python package is unable to easily solve sensitivities during the evaluation of the eigenvalues. The sensitivities of the aggregated inverse buckling load factors are written as (Raspanti et al., 2000; Ferrari et al., 2021)

$$\frac{\partial \mu_{KS}}{\partial \overline{\chi_j}} = \frac{\sum_{i \in \gamma} e^{q(\mu_i - \mu_1)} \frac{\partial \mu_i}{\partial \overline{\chi_j}}}{\sum_{i \in \gamma} e^{q(\mu_i - \mu_1)}} \tag{6.17}$$

where $\frac{\partial \mu_i}{\overline{\chi_j}}$ can be evaluated by (Rodrigues et al., 1995; Ferrari and Sigmund, 2019)

$$\frac{\partial \mu_i}{\overline{\chi_j}} = -\left[\boldsymbol{\psi}_i^T \left(\frac{\partial \widehat{\boldsymbol{G}}(\boldsymbol{u})}{\partial \overline{\chi_j}} + \mu_i \frac{\partial \widehat{\boldsymbol{K}}}{\partial \overline{\chi_j}} \right) \boldsymbol{\psi} - \boldsymbol{v}_i^T \frac{\partial \widehat{\boldsymbol{K}}}{\partial \overline{\chi_j}} \boldsymbol{u} \right] \tag{6.18}$$

where $\overline{\chi}_j$ denotes the filtered design variables in the set of $\{\widehat{\rho}, \overline{V_f}, \overline{\boldsymbol{U}}\}$, and $\boldsymbol{v}_i$ denotes adjoint displacement fields which can be evaluated by solving

$$\widehat{\boldsymbol{K}}\boldsymbol{v}_i = \boldsymbol{\psi}_i^T(\nabla_{\boldsymbol{u}}\widehat{\boldsymbol{G}})\boldsymbol{\psi}_i \tag{6.19}$$

The partial differentials of stress stiffness matrix and stiffness matrix with respect to each design variable are written as

$$\begin{aligned}
\frac{\partial\widehat{\boldsymbol{G}}}{\partial\widehat{\rho}_\sigma} &= \epsilon(\boldsymbol{u}_0) : p\widehat{\rho}_\sigma^{(p-1)}\boldsymbol{K}_e : \nabla\delta\boldsymbol{v}^T\nabla\delta\boldsymbol{u} \\
\frac{\partial\widehat{\boldsymbol{G}}}{\partial\overline{V_f}} &= \epsilon(\boldsymbol{u}_0) : \frac{\partial\widehat{\boldsymbol{K}}_e}{\partial\overline{V_f}} : \nabla\delta\boldsymbol{v}^T\nabla\delta\boldsymbol{u} \\
\frac{\partial\widehat{\boldsymbol{G}}}{\partial\overline{\boldsymbol{U}}} &= \epsilon(\boldsymbol{u}_0) : \frac{\partial\widehat{\boldsymbol{K}}_e}{\partial\overline{\boldsymbol{U}}} : \nabla\delta\boldsymbol{v}^T\nabla\delta\boldsymbol{u} \\
\frac{\partial\widehat{\boldsymbol{K}}}{\partial\widehat{\rho}_k} &= \epsilon(\delta\boldsymbol{v}) : p\widehat{\rho}_k^{(p-1)}\boldsymbol{K}_e : \epsilon(\delta\boldsymbol{u}) \\
\frac{\partial\widehat{\boldsymbol{K}}}{\partial\overline{V_f}} &= \epsilon(\delta\boldsymbol{v}) : \frac{\partial\widehat{\boldsymbol{K}}_e}{\partial\overline{V_f}} : \epsilon(\delta\boldsymbol{u}) \\
\frac{\partial\widehat{\boldsymbol{K}}}{\partial\overline{\boldsymbol{U}}} &= \epsilon(\delta\boldsymbol{v}) : \frac{\partial\widehat{\boldsymbol{K}}_e}{\partial\overline{\boldsymbol{U}}} : \epsilon(\delta\boldsymbol{u})
\end{aligned} \tag{6.20}$$

where $\frac{\partial\widehat{\boldsymbol{K}}_e}{\partial\overline{V_f}}$ and $\frac{\partial\widehat{\boldsymbol{K}}_e}{\partial\overline{\boldsymbol{U}}}$ are then solved using automatic differentiation. It is important to note that the implementation of aggregation function provides a smooth and unique expression of the sensitivities even when the eigenvalues are repeated (Seyraniant et al., 1994; Gravesen et al., 2011).

An extra chain rule evaluation is needed to give the derivative with respect to the pseudo-density, compared to Eq. 3.28, due to the implementation of the threshold projection so that the derivative can be written as

$$\frac{\partial}{\partial\rho} = \frac{\partial}{\partial\widehat{\rho}}\frac{\partial\widehat{\rho}}{\partial\overline{\rho}}\frac{\partial\overline{\rho}}{\partial\rho} \tag{6.21}$$

6.5 Optimisation Formulations

Prior to carry out the buckling resistance maximisation, a compliance minimisation is performed using the following formulation

$$\begin{aligned} \min_{\rho,V_f,\boldsymbol{U},S_1,S_2} \quad & J(\rho,V_f,\boldsymbol{U}) = \int_\Omega \boldsymbol{f}\boldsymbol{u}dx \\ s.t. \quad & \boldsymbol{f} = \boldsymbol{K}\boldsymbol{u} \\ & g_v = \int_\Omega \frac{\widehat{\rho}_k}{V}dx - V_0 \leq 0 \\ & 0 \leq \rho \leq 1 \\ & 0 \leq V_f \leq 0.5 \\ & -1 \leq U_x, U_y \leq 1 \end{aligned} \tag{6.22}$$

where J denotes the compliance, Ω denotes the design domain, $\boldsymbol{K}$ is the global stress stiffness matrix which is assembled using $\widehat{\boldsymbol{K}}_e$ in Eq. 6.14, g_v denotes the volume constraint, V denotes the volume of the design domain, V_0 denotes the targeting structure volume fraction.

An optimisation problem considering maximum buckling resistance and manufacturability subject to volume and compliance constraints by parameterising the pseudo density, the fibre orientation and the fibre volume fraction is then considered, as described by

$$\begin{aligned} \min_{\rho,V_f,\boldsymbol{U},S_1,S_2} \quad & \mu_{KS}(\rho,V_f,\boldsymbol{U}) \\ s.t. \quad & \boldsymbol{f} = \boldsymbol{K}\boldsymbol{u} \\ & \big[\boldsymbol{G}(\boldsymbol{u}) + \mu_i\boldsymbol{K}\big]\boldsymbol{\psi}_i = 0, \quad i \in \alpha \\ & g_c = \frac{J}{cJ_0} - 1 \leq 0 \\ & g_v = \int_\Omega \frac{\widehat{\rho}_k}{V}dx - V_0 \leq 0 \\ & C_1 \quad \text{Eq. (3.26)} \\ & C_2 \quad \text{Eq. (3.27)} \\ & 0 \leq \rho \leq 1 \quad ; \quad 0 \leq V_f \leq 0.5 \quad ; \quad -1 \leq U_x, U_y \leq 1 \end{aligned} \tag{6.23}$$

where $\boldsymbol{G}$ is global stress stiffness matrix which is assembled using $\widehat{\boldsymbol{G}}_e$ in Eq. 6.14, g_c denotes the

compliance constraint, J_0 denotes the compliance value obtained from the minimum compliance design, c denotes a constant used to scale the minimum compliance and C_1, C_2 denote the manufacturing constraints. The purpose of implementing the compliance constraint is to keep the optimisation in the feasible space and avoid the competition between the stiffness and buckling resistance. The update of the design variables are determined by the method of moving asymptotes (Svanberg, 1987).

6.6 Summary

The methodology of optimisation accounting for buckling resistance is detailed in this chapter. To capture the buckling characteristics, linear buckling analysis is firstly introduced. The buckling characteristics obtained by the linear buckling analysis are approximated through the aggregation formulation to achieve smooth convergence. A method is adopted to erode and regularise the stress fields to reduce the occurrence of the spurious buckling modes. To perform gradient-base optimisation, the sensitivities which can not easily evaluated using adjoint method are derived. The optimisation formulation for maximising the buckling resistance whilst considering the manufacturability is presented.

In summary, the methodology introduced in this chapter extends the optimisation framework to reduce the potential of buckling failure for the lightweighting topological optimised designs by improving the buckling resistance.

Chapter 7

Design for Buckling Resistance Results and Discussion

Three classic buckling resistance problem, a compressed column, a stubby cantilever and an MBB beam, are firstly presented in this chapter to validate the optimisation framework. The twisted and compressed column problem solved in Secs. 5.2 is solved again with additional buckling requirements. The discussion is focused on the responses of the topology and fibre orientation while maximising the buckling resistance. The performance of the optimal structure is benchmarked against an isotropic case using random oriented short fibres in the compressed column problem. The compromise between the buckling resistance and manufacturability is also discussed.

7.1 Parameters Setup

The material properties of the fibre and matrix are assumed to be $E_f = 200\,\text{Pa}$, $E_m = 10\,\text{Pa}$, and $\nu_f = \nu_m = 0.3$. Note that the Young's modulus of the isotropic case, $E_s = 30\,\text{Pa}$, represented by random oriented short fibres is evaluated by the Cox-Krenchel model (Sanomura and Kawamura, 2003; Avanzini et al., 2022) using the same parameters of fibre and matrix material properties and a fibre volume fraction of 0.5. Note that although the 2D mesh convergence study has shown the computational error is less than 0.05% when the unit division is greater

than 40 (see Fig. 4.2), the mesh size in the following 2D problems are chosen to 1/120 m to generate small details of topology. The Helmholtz filter radius is chosen to be twice as the mesh size to avoid discontinuous topology due to the competition between stiffness and buckling resistance. The boundary length scale of the Robin boundary condition for filtering the pseudo-density is the same as the Helmholtz filter radius. The threshold projection parameters follow the proposed values from Ferrari and Sigmund (2023) as $\eta_k = 0.5$ and $\eta_\sigma = 0.75$. The number of the eigenpairs considered, γ, is set to 12 which is greater than the parameter used in Dunning et al. (2016) to achieve smooth convergence behaviour. The aggregation parameter, q, is set to a large number, 160, to capture the first three buckling modes. The optimisation process uses a continuation approach so that the penalisation parameter, p, starts from 3 and increases by 0.25 every 25 iterations to 6, and the projection parameter, β, starts from 2 and increases by 1 every 25 iterations to 16 after iteration 400 to minimise the intermediate materials. The optimisation runs for 750 iterations in total as the continuation of β reaches 16 at the last 25 iterations from iteration 726. The continuation scheme follows Ferrari and Sigmund (2023) due to the adoption of the stress regularisation approach. This continuation scheme has been proved robust in their cases. To prove the convergence of the optimisation problems in this work, it has been confirmed that the objective function decreases by less than 0.01% and the constraint violations are less than 10^{-4} in the last five iterations. The parameters setup of the problems are summarised in Tab. 7.1.

7.2 Compressed Column (2D)

The design domain of the compressed column shown in Fig. 7.1a where the domain is discretised to 120×240 structured first-order quadrilateral elements. The dimensions of the domain are $L_y = 2L_x = 2\,\mathrm{m}$ and $b = L_y/15$. A Dirichlet boundary condition is applied at the bottom edge and a uniform load, $\boldsymbol{f} = 1\,\mathrm{N\,m^{-1}}$, is evenly distributed on the middle of the top edge. The volume constraint, V_0, is set to 30% of the design domain, consistent with literature, to have better comparison.

The examples in this section involve the optimisation of anisotropic continuous fibre and isotropic short random-oriented FRCs. In both cases, compliance minimisation is initially

Table 7.1: The problem setup of the 2D buckling resistance problems

	Compressed column	Stubby cantilever	MBB beam
Mesh			
Element	2D Quadrilateral		
L_x	1 m	0.9 m	2 m
L_y	2 m	2 m	1 m
b	2/15 m	2/12.5 m	2/15 m
Element size	0.01 m		
Number of elements	28,800	25,920	28,800
Number of nodes	29,161	26,269	29,161
Number of design variables	145,444	130,996	145,444
Optimisation			
r_h (Helmholtz filter radius)	0.02 m		
r_b (Helmholtz filter boundary radius)	0.02 m		
p (SIMP parameter)	$3 \rightarrow 6$ (continuation)		
β (Projection parameter)	$2 \rightarrow 16$ (continuation)		
V_0 (target volume)	30%	20%	30%
c (compliance constraint constant)	10	2	1.5
Initial guesses			
ρ	0.3	0.2	0.3
(U_x, U_y)	(0,1)	(1,0)	(1,0)
V_f	0.5	0.5	0.5
S	x	y	y
Material properties			
E_f	200 Pa		
E_m	10 Pa		
E_s	30 Pa		
ν_f	0.3		
ν_m	0.3		
ν_s	0.3		

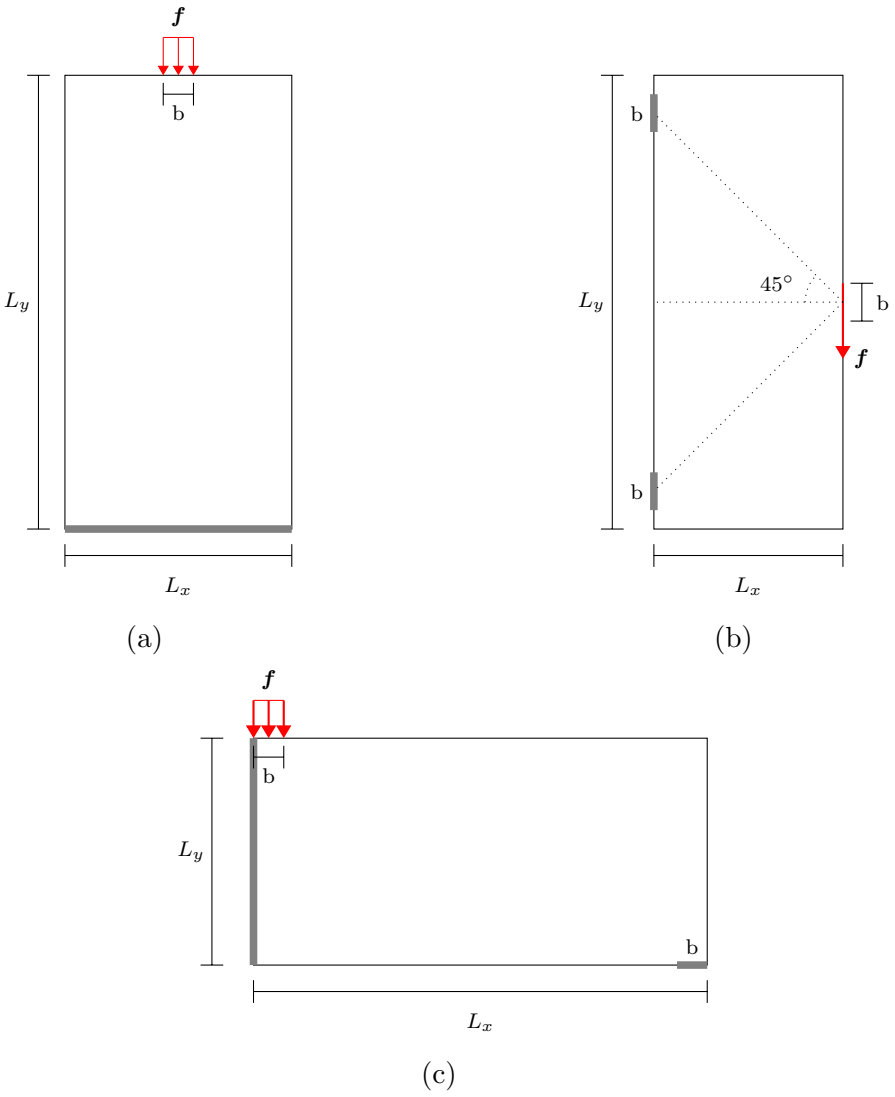
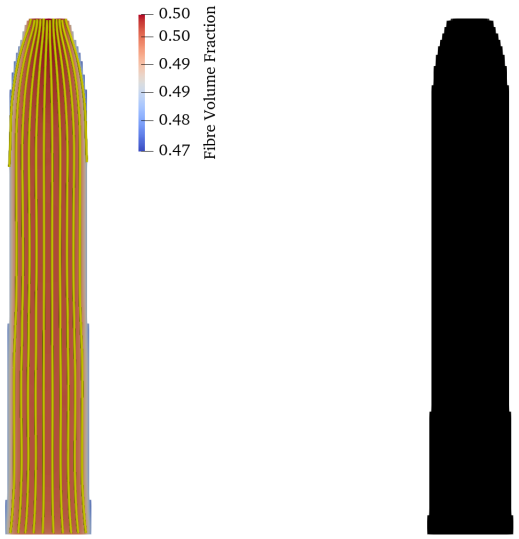


Figure 7.1: The design domain of the (a) Compressed column and (b) Stubby cantilever (c) Half MBB beam

performed, and the compliance value is later utilised as a constraint in the maximisation of buckling resistance.

The minimum compliance designs are illustrated in Fig. 7.2, where the topology forms a straight column with a thinner head and a wider bottom in both cases. In the continuous fibre case, the fibre orientation follows a topology that diverges from the top to the bottom, while the middle part remains almost straight. The fibre volume fraction is naturally pushed close to its upper bound to achieve the minimum compliance design. This raises a manufacturing issue that the fibre volume fraction does not reflect the variation of the fibre orientation when the fibre paths diverged, leading to a infeasible design. The buckling load factors are 1.74 and 0.87, and the



(a) (b)

Figure 7.2: The minimum compliance designs of the (a) continuous fibre (b) short random-oriented fibre. (Note that the fibre paths are visualised by randomly seeded streamlines)

Case	Material	Manufacturing constraints
A	Continuous fibre	Disabled
B	Continuous fibre	Enabled
C	Short-random fibre	Disabled

Table 7.2: The material and manufacturing constraints setup for the compressed column cases

compliance values are 1.2×10^{-3}N m and 4.1×10^{-3}N m, respectively. Although both cases have almost the same fibre volume fraction and a similar topology, the continuous fibre case fully utilises the anisotropic properties by aligning the fibre orientation with the force direction. This results in an increased stiffness along the force direction; thus, the continuous fibre case performs better in both stiffness and buckling resistance.

The compliance of the minimum compliance design is used as a constraint in the subsequent buckling resistance maximisation problems. The compliance constraint parameter, c, is set to 10. The optimisation setup for the following cases is listed in Tab. 7.2.

The buckling designs illustrated in Fig. 7.3 depict the configurations for continuous fibre without manufacturing constraints (Case A), continuous fibre with manufacturing constraints (Case B), and short random-oriented fibre (Case C). These designs consist of two tilted major members and additional bracing members which have a similar topology layout compared with the designs demonstrated in previous studies using isotropic materials (Gao and Ma, 2015; Ferrari and

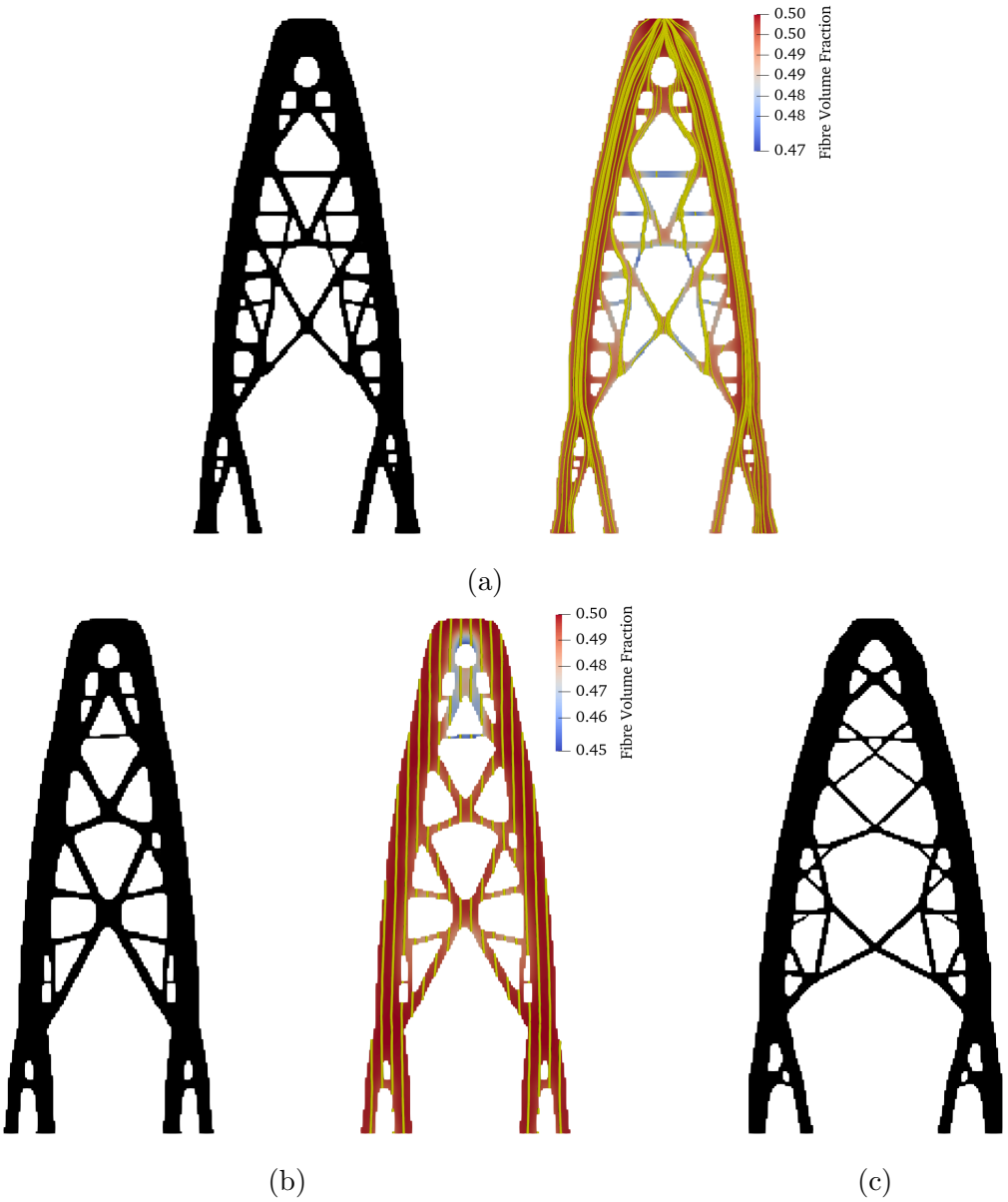


Figure 7.3: The topology, the fibre orientation and the fibre volume fraction of (a) Case A (continuous fibre without manufacturing constraints) and (b) Case B (continuous fibre with manufacturing constraints)(c) The topology of Case C (short random-oriented fibre)

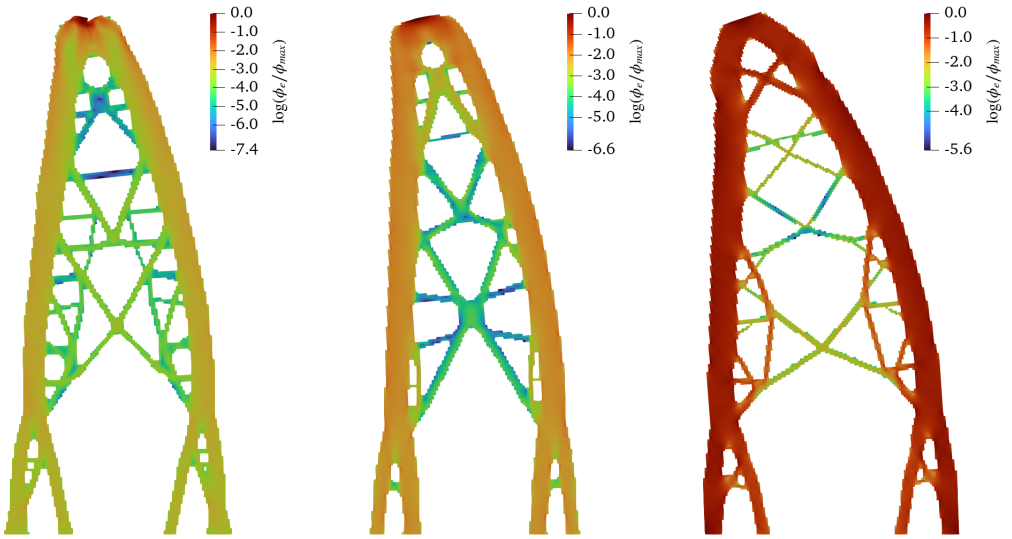
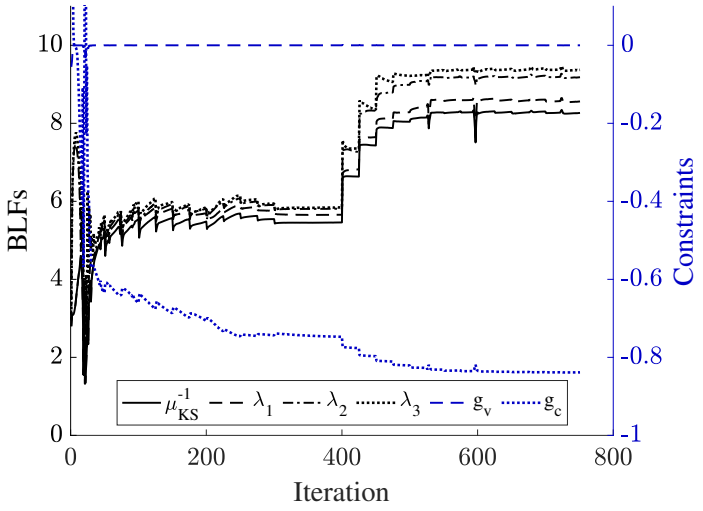


Figure 7.4: The first buckling mode of the cases (Note that the buckling modes are coloured by the strain energy density ($\phi_e = \boldsymbol{\psi}_e^T \widehat{\boldsymbol{K}}_e \boldsymbol{\psi}_e$) using the scale of $\log(\phi_e/\phi_{max})$)

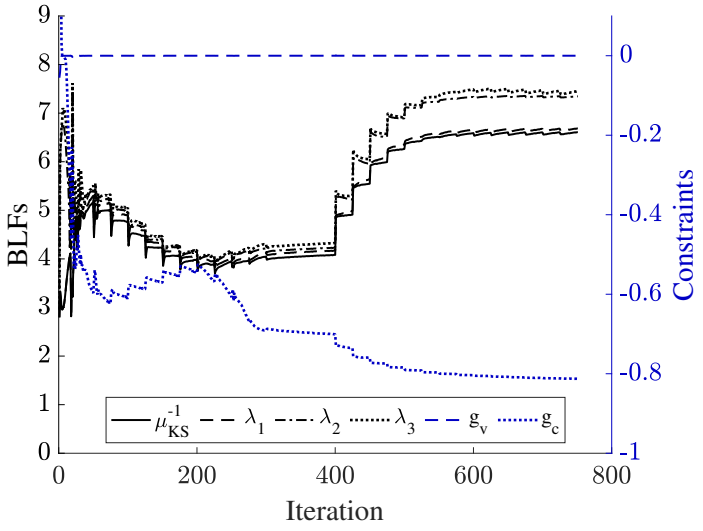
Sigmund, 2023; Xu et al., 2023). The tilted members enhance the second moment of area, while the bracing members provide support. The first buckling mode of each case is shown in Fig. 7.4.

The buckling load factors for designs A, B, and C are 8.56, 6.69, and 4.01, respectively, with the compliance constraint not active in any of the cases (see Fig. 7.5). The buckling resistance increases by 4.92, 3.84, and 4.61 times, respectively, compared to the minimum compliance designs. From a topological perspective, Case C possesses the widest base, which has the greatest second moment of area, which theoretically should have resulted in better buckling resistance. However, the continuous fibre cases perform better than the short random-oriented fibre case due to the alignment between fibre orientation and loading direction.

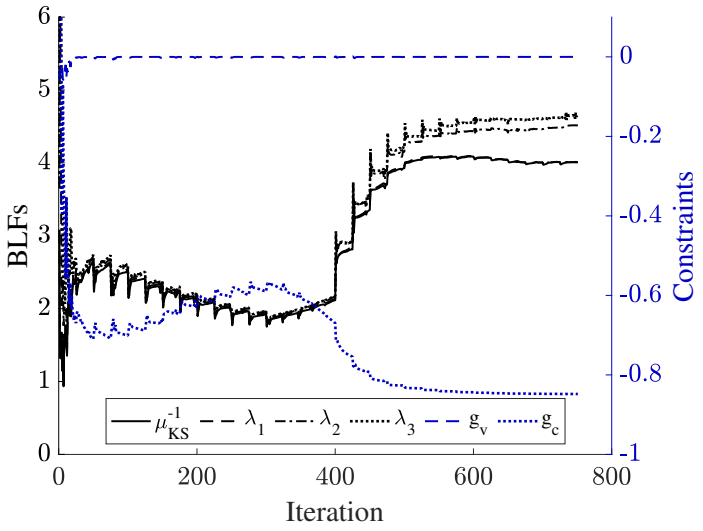
In Case A, the fibre paths visualised by randomly seeded streamlines mostly follow the topology, except for some horizontal bracing members, owing to the implementation of Helmholtz filter that avoids large fibre orientation variations. Without manufacturing constraints, the streamlines are again proved to be not evenly spaced as required for the fibre paths with a correct variation of the fibre volume fraction, leading to terminated short fibres and resin-rich areas. Constructing the fibre paths correctly requires additional effort in post-processing to choose the seed locations of the streamlines. However, the issue of the terminated short fibres and resin-rich areas is not guaranteed to be resolved. In Case B, the fibre paths, represented



(a)



(b)



(c)

Figure 7.5: The convergence plots of (a) Case A, (b) Case B and (c) Case C

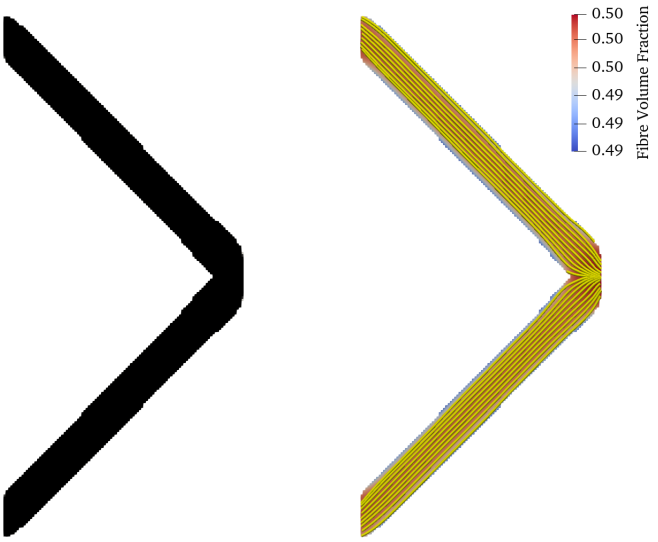


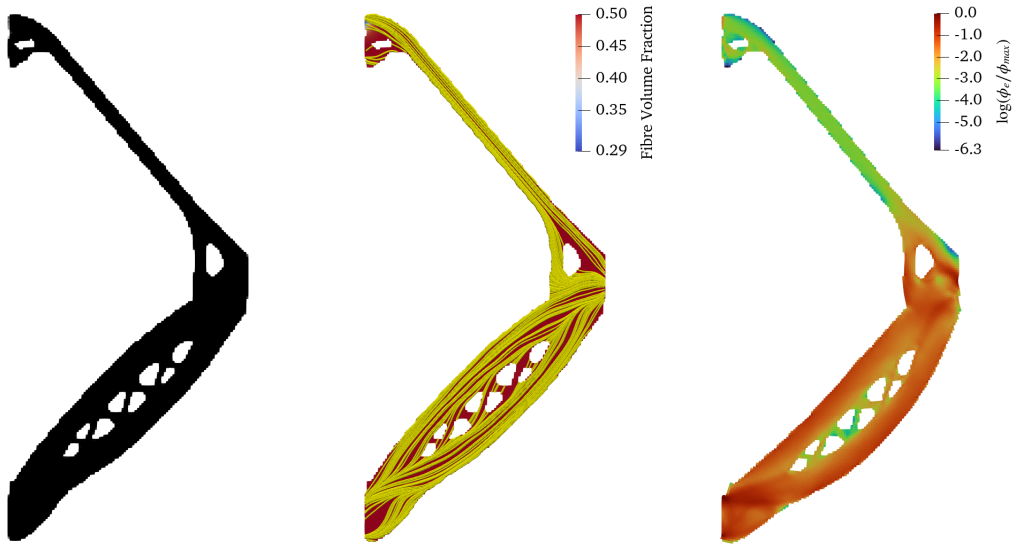
Figure 7.6: The topology and the fibre orientation of the stubby cantilever minimum compliance design

by iso-contours, diverge slightly from the top to the bottom. The distances between fibre paths correspond to variations in the fibre volume fraction in this case. This shows that it is more important that the fibre volume fraction is close to its upper bound using almost straight fibres than redistributing the compression stress by diverging the fibre paths in this case. The base of the topology is narrower, and the fibre orientation is almost straight due to tight manufacturing constraints, resulting in a lower buckling resistance compared to Case A, Case B is a more manufacturable design and still outperforms the minimum compliance design.

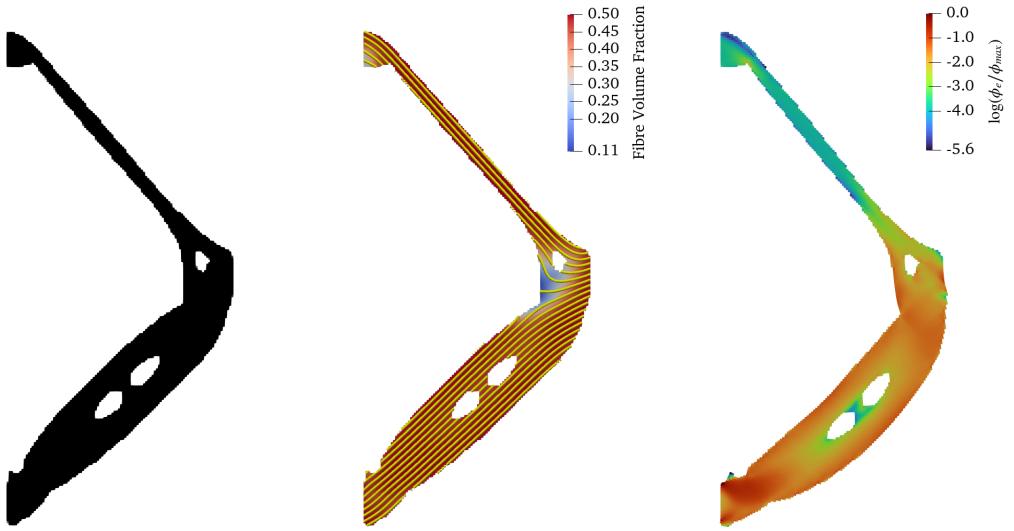
The comparison of the compressed column cases indicates that using anisotropic continuous fibre results in better performance not only in minimum compliance design but also in buckling design. The subsequent discussion will focus solely on continuous fibre cases.

7.3 Stubby Cantilever (2D)

The design domain of the stubby cantilever is defined as shown in Fig. 7.1b where the domain is discretised to 108×240 structured first-order quadrilateral elements. The dimensions of the domain are $L_y = 2\,\mathrm{m}$, $L_x = 0.9\,\mathrm{m}$ and $b = L_y/12.5$. A Dirichlet boundary condition is applied on the left edge marked by grey and a uniform load, $\boldsymbol{f} = 1\,\mathrm{N\,m^{-1}}$, is evenly distributed on the middle of the right edge with a length of b. The volume constraint, V_0, is set to 20% of the design domain.

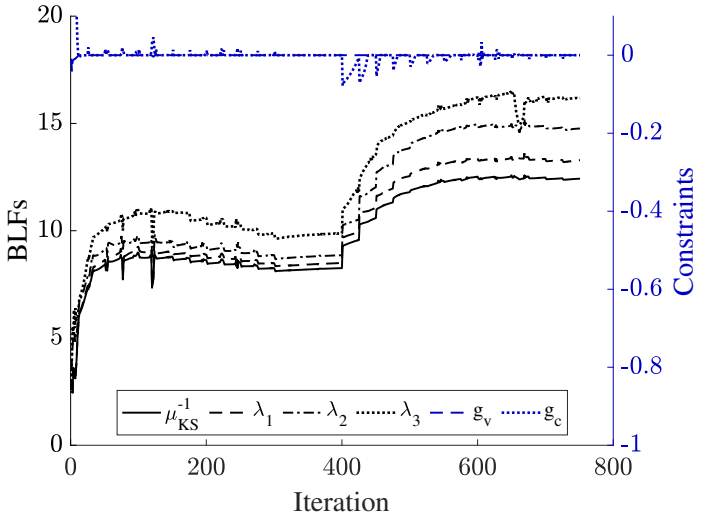


(a)

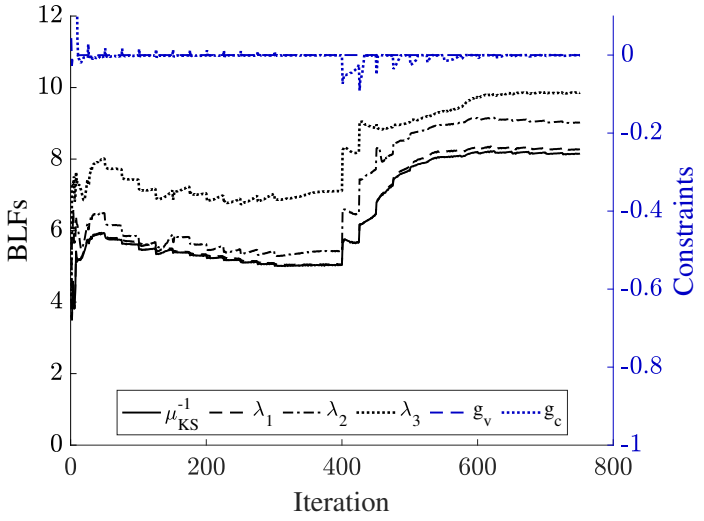


(b)

Figure 7.7: The stubby cantilever buckling design of (a) Case D and (b) Case E (Left: the topology; Central: the fibre orientation and fibre volume fraction; Right: the first buckling mode)



(a)



(b)

Figure 7.8: The convergence plots of (a) Case D and (b) Case E

The minimum compliance design shown in Fig. 7.6 consists of two straight members, with the upper one in tension and the bottom one in compression. The fibre orientation mostly follows the topology, except in the region where the members intersect, causing the fibre orientation to converge. The buckling load factor is 3.99 and the compliance is 2.17×10^{-3} for the design where only compliance is considered. In this case, the compliance constraint constant is set to $c = 2$ for the buckling design.

The buckling designs illustrated in Fig. 7.7 are considered under the setup with manufacturing constraints disabled (Case D) and enabled (Case E). Both buckling designs share a similar topology, with material being removed from the tensioned member and added to the compressed

member compared to the minimum compliance design. An additional member linking the two members near the intersection area is generated to stabilise the compressed member. The compressed member splits to form two arch members to increase the second moment of area, and bracing members are generated to support them. The buckling load factors are 13.28 and 8.27, representing an increase of 3.33 and 2.07 times compared to the minimum compliance design. The compliance constraint is active in both cases (see Fig. 7.8). In Case D, the upper member exhibits a competition between buckling resistance and compliance, leading to a topology that is only supported at the boundary with few elements, and the fibre volume fraction reduces to 0.29 near supported boundary of the tensioned member. Conversely, in Case E, these effects are not observed, as the manufacturing constraints enforce the continuity of the fibre orientation, preventing local stress fluctuations. This is evidenced by the smooth variation in strain energy density shown in Fig. 7.7b.

In Case D, with unconstrained fibre orientation, compression stress is effectively redistributed, and the unconstrained fibre volume fraction naturally reaches the upper bound to enhance stiffness and buckling resistance. Conversely, the design under manufacturing constraints (Case E) results in straight fibre paths to maximise the fibre volume fraction at the compressed member and a variation in fibre volume fraction at the region where the members intersect.

7.4 MBB Beam (2D)

The design domain of a half MBB beam is defined as shown in Fig. 7.1c where the domain is discretised to 240×120 structured first-order quadrilateral elements. The dimensions of the domain are $L_x = 2L_y = 2\,\mathrm{m}$ and $b = L_x/15$. A Dirichlet boundary condition ($\boldsymbol{u}_x = 0\,\mathrm{m}$) is applied on the left edge marked by grey label and another Dirichlet boundary condition ($\boldsymbol{u}_x = 0\,\mathrm{m}$) is evenly distributed on the right of the bottom edge with a length of b. Note that the boundary condition imposes the symmetric condition to model a full MBB beam. A uniform force, $\boldsymbol{f} = 1\,\mathrm{N\,m^{-1}}$, is loading on the left of the top edge with a length of b. The volume constraint, V_0, is set to 30% of the design domain.

The minimum compliance design of the MBB beam is shown in Fig. 7.9. The topology comprises several long and thin members, indicating a high potential for buckling. The fibre orientation

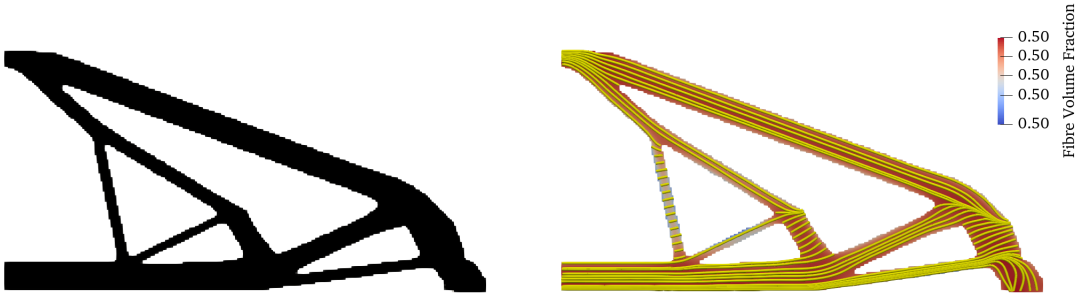


Figure 7.9: The topology and the fibre orientation of the MBB beam minimum compliance design

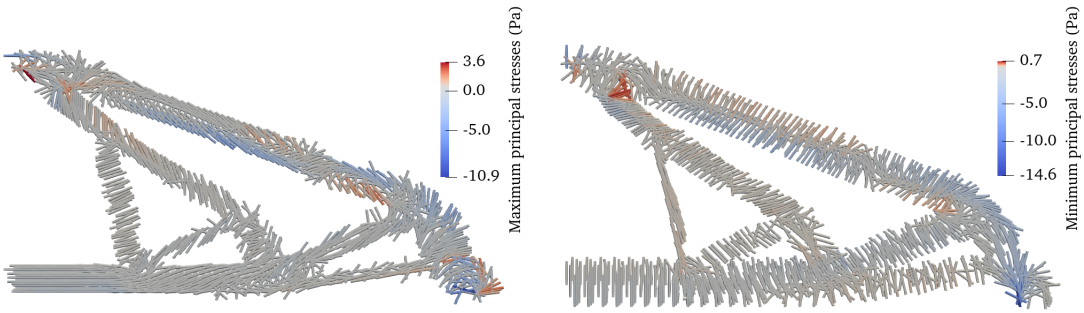
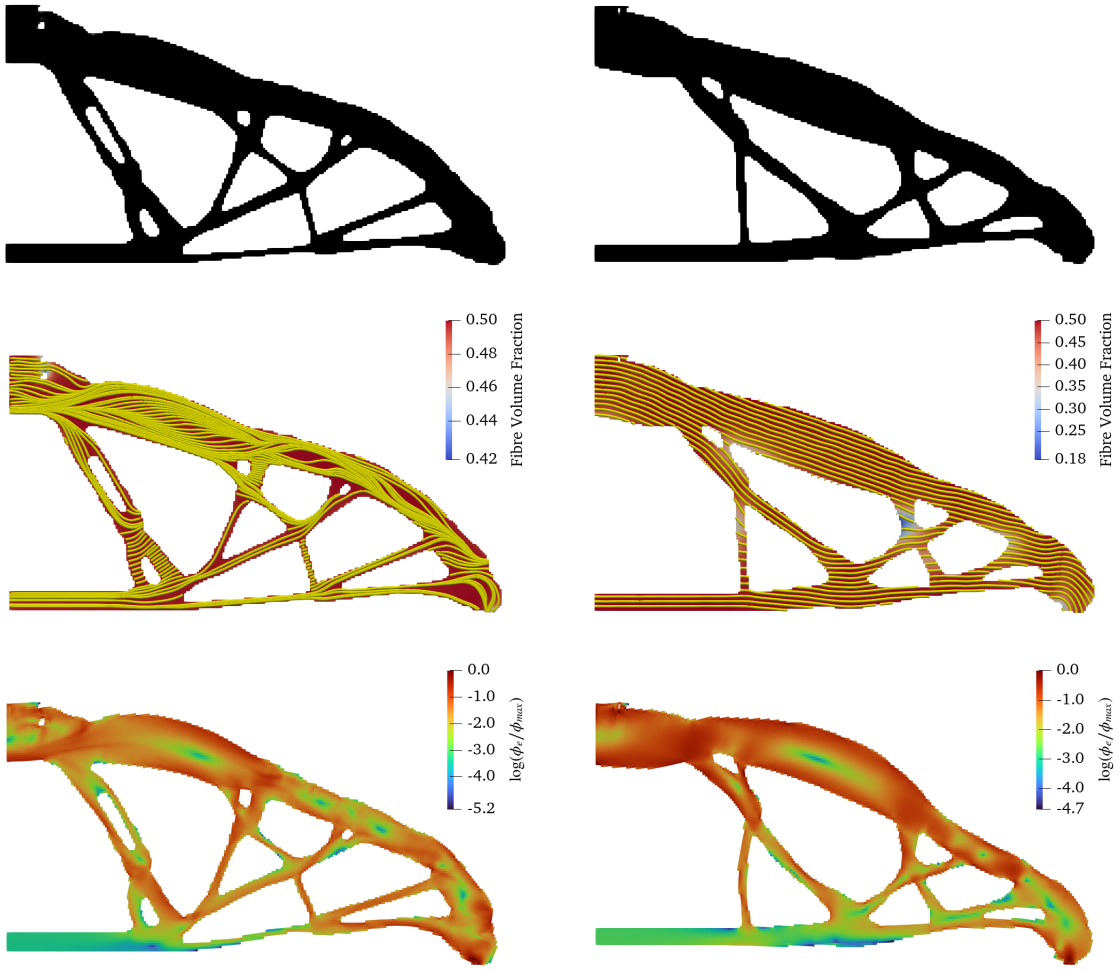


Figure 7.10: The principal stresses of the 2D MBB beam minimum compliance design (left: maximum, Right: minimum)

mostly aligns with the maximum principal stress direction (see Fig. 7.10). Note that the fibre orientation at some region is not aligned with any principal stress direction to have a better balance between them. The fibre volume fraction is pushed to its upper bound to minimise compliance. The issue with incorrect variation in fibre volume fraction is again observed. The buckling load factor for the minimum compliance design is 0.59, consistent with the indication above. In this case, the compliance is 1.95×10^{-2} and the compliance constraint constant is set to $c = 1.5$ for the buckling design.

The buckling designs illustrated in Fig. 7.11 are considered under the setup with manufacturing constraints disabled (Case F) and enabled (Case G). The buckling designs both have a thicker and shorter major compressive member and extra support members to withstand the compressive load, compared to the minimum compliance design. Comparing to the design demonstrated in Ferrari and Sigmund (2023), the topology is similar in terms of improved buckling resistance, apart from that the support members are less hierarchical and the support member at the middle of left hand side does not exist. This may be caused by different characteristics of how

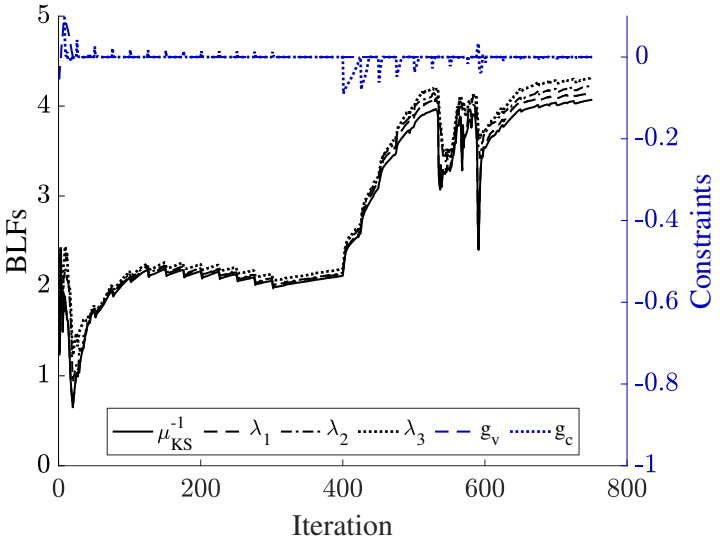


(a) (b)

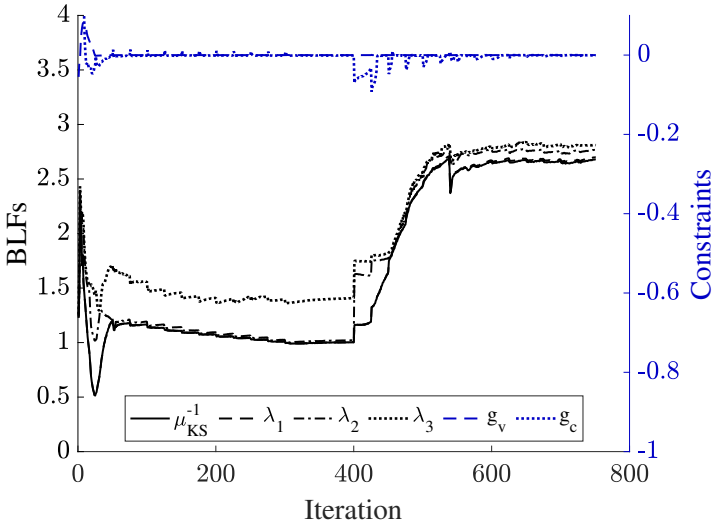
Figure 7.11: The MBB beam buckling design of (a) Case F and (b) Case G (Top: the topology; Middle: the fibre orientation and fibre volume fraction; Bottom: the first buckling mode)

compressive stress is distributed between isotropic and anisotropic materials. The buckling load factors of the designs are 4.15 and 2.7, which increase by 7.03 and 4.58 times, respectively. Due to the shear-dominant load case, the compliance constraints are active in both cases (see Fig. 7.12).

The topology of Case G has fewer small support members due to the limitation of variation in fibre orientation imposed by manufacturing constraints. The freely oriented fibre in Case F at the major compressive member shows a diverging and converging fibre orientation in each segment to redistribute the compressive load. The fibre orientation visualised using the randomly seeded method again shows the difficulty in reflecting the corresponding fibre volume



(a)



(b)

Figure 7.12: The convergence plots of (a) Case D and (b) Case E

fraction, leading to an overestimation of both stiffness and buckling resistance. In comparison with Case F, the fibre paths represented by the iso-contours show a smooth variation, especially in the region where the downward and upward fibres converge. Additionally, the fibre volume fraction in Case G accurately reflects variations in fibre orientation without overestimation. This provides evidence for why the buckling resistance in Case G is lower than in Case F.

In this example, both cases demonstrate significant improvements in buckling resistance compared to the minimum compliance design.

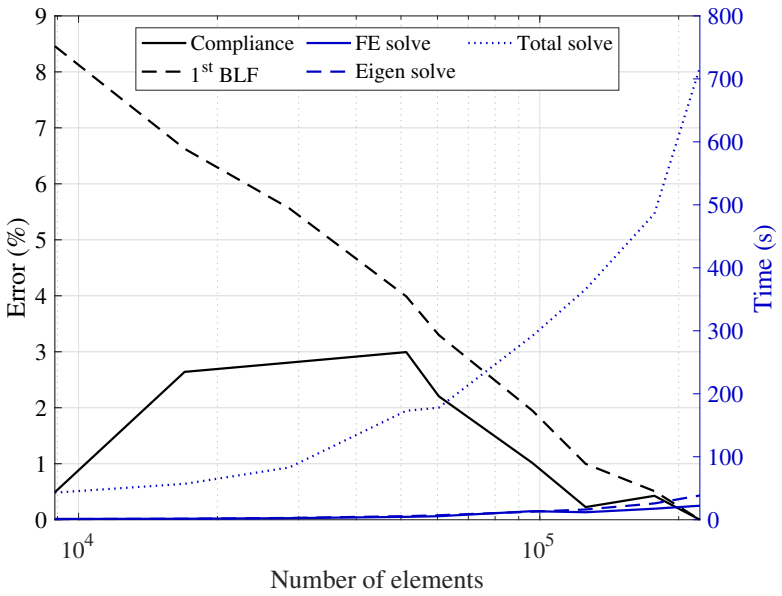
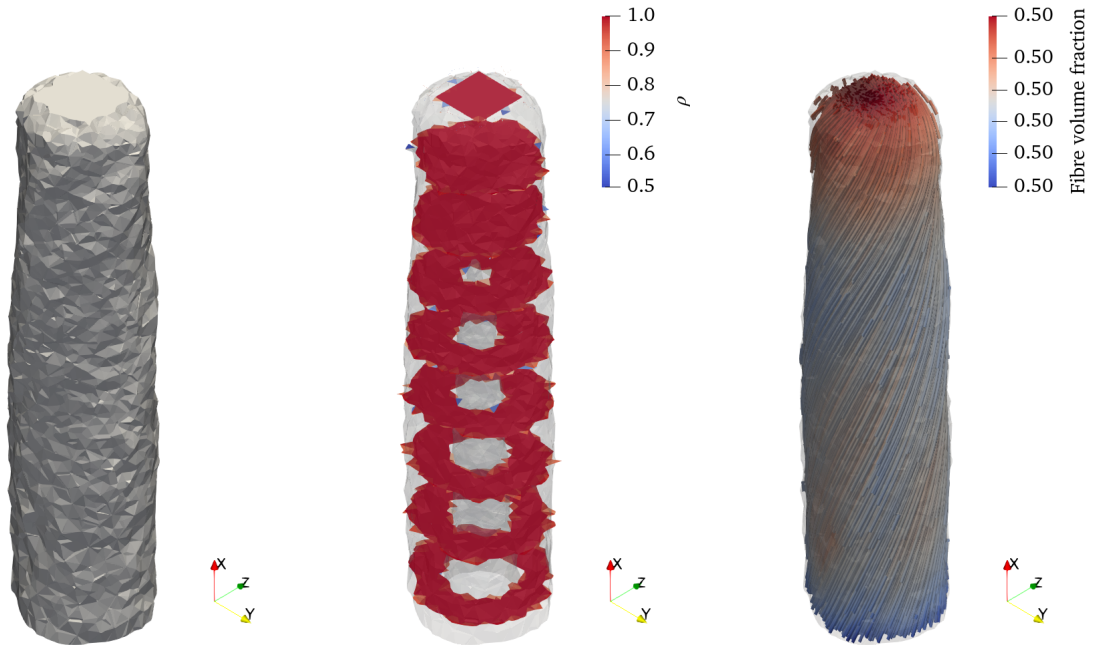


Figure 7.13: Mesh convergence plot of the twisted and compressed column

7.5 Twisted and Compressed Column

The twisted and compressed column problem solved in Sec. 5.2 shows an effective design of a hollow column with a spiral fibre orientation. However, The buckling analysis in Sec. 5.4 indicates that the potential of buckling failure is high due to the low buckling load factor. In this section, the problem is solved again whilst targeting on increase in the buckling resistance. Note that the problem now is solved using the optimisation formulation Eq. (6.23). The design domain is the same as shown in Fig. 5.12 and the problem setup is summarised in Tab. 7.3.

Prior to solving the optimisation problem, a mesh convergence test was conducted. During the convergence test, the optimisation problems were solved in parallel using twelve AMD EPYC 7316 processors operating at 3 GHz. The unit length division increased from 10 to 30 in increments of 2.5. The errors in compliance and the first buckling load factor and the computational cost are shown in Fig. 7.13. The convergence plot illustrates that the computational error decreases as the number of elements increases. Both errors are less than 1% when the number of elements is greater than 1.2×10^5, with a unit length division greater than 25. The computational costs of solving the finite element and eigenvalue problems do not significantly increase. However, the total computational cost increases by almost 1.5 times as the unit length division increases due to the sensitivity solve. The requirement of the assembly of the gradient



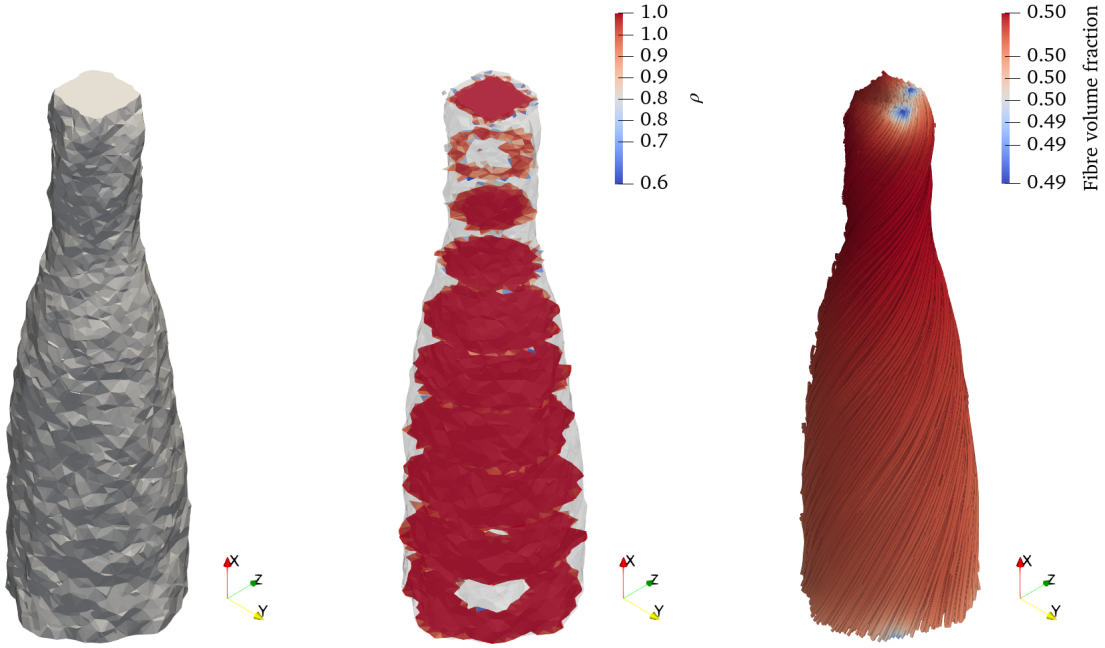
(a) (b) (c)

Figure 7.14: The minimum compliance design of the twisted and compressed column: (a) the topology (b) the slices of the topology (c) the fibre orientation

term, $\nabla_u \widehat{\boldsymbol{G}}$, and the multiple linear algebra computations of the adjoint displacement fields in Eq. (6.18) are the major reasons that slow the sensitivity evaluation. In addition, due to the implementation of the continuation approach, the required iterations increase significantly as well. To achieve a balance between error and computational cost, the twisted and compressed column accounting for buckling resistance, is solved at a lower mesh density compared to the results in the previous section, with an element size of $1/25\,\mathrm{m}$.

7.5.1 Minimum Compliance Design

The minimum compliance design demonstrated in Fig. 7.14 is slightly different from the design demonstrated in Secs. 5.2 since the pseudo-density has been push closer to a binary distribution through the continuation approach of the SIMP parameter and the threshold projection parameter. The fibre orientation remains a spiral orientation around the hollow column and the fibre volume fraction is pushed to its upper bound to achieve the minimum compliance design. The critical buckling load factor is 3.79 in this parameter setup. The compliance of this design is 3.97×10^{-4}. Note that the binary distribution of the pseudo-density significantly



(a) (b) (c)

Figure 7.15: The buckling design of the twisted and compressed column: (a) the topology (b) the slices of the topology (c) the fibre orientation

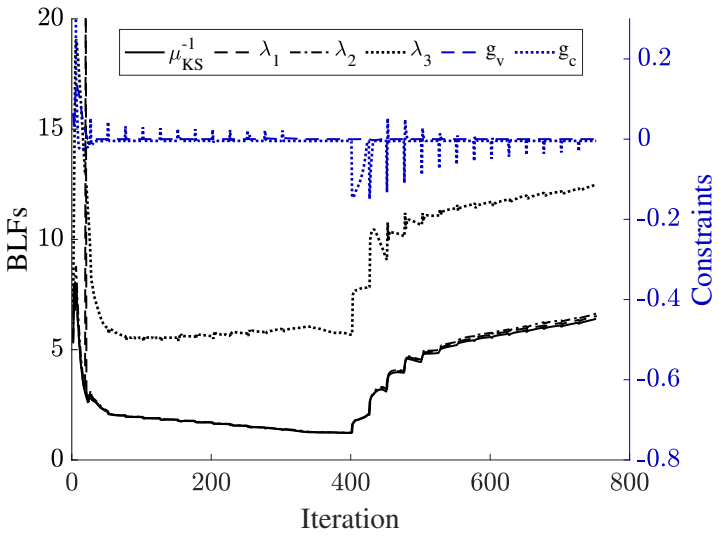


Figure 7.16: The convergence plot of the 3D twisted and compressed column

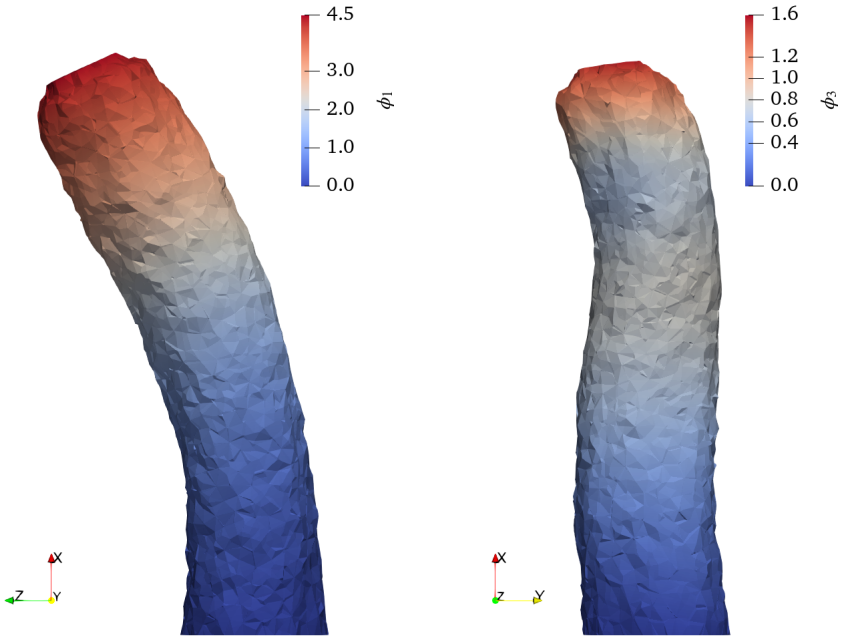
improves performance in terms of stiffness and buckling load factor. This is because the stiffness has been penalised to the power of three based on the pseudo density so that the stiffness in the intermediate region is significantly lower than a solid distribution. Additionally the solid distribution on the outer side of the column greatly enhances its ability to withstand torsional loading. The compliance constraint is set to $c = 2$ for the maximum buckling design.

7.5.2 Maximum Buckling Resistance Design

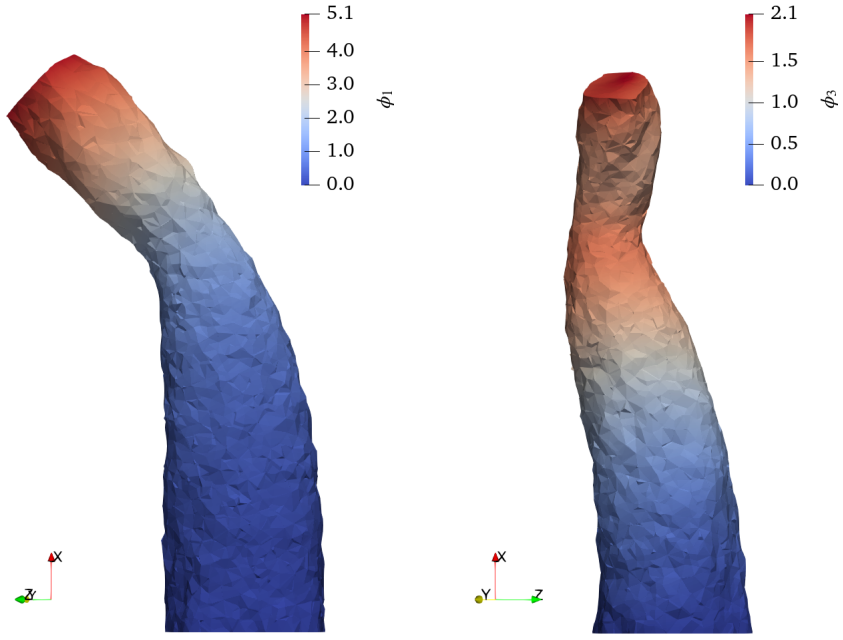
The maximum buckling resistance design is shown in Fig. 7.15. Unlike the compressed column in 2D forming a tower-like structure, the topology forms a column composed of a hollow thin neck and a solid wide base with a small hole at the bottom. The pseudo-density at the neck region is not as binary as the minimum compliance design. This may be caused by the limited element size which shows difficulty to generate detailed structural members around the neck region. The fibre orientation and the fibre volume fraction remain approximately the same as the minimum compliance design. In order to fulfil the compliance constraint, the spiral intensity close to the neck region is stronger to maintain the resistance against the torsion load due to less materials are distributed here compared to the minimum compliance design.

Due to the shear-dominant load condition, the compliance constraint is activate (see Fig. 7.16). The critical buckling load factor is 6.53, which is a 72% increase compared to the minimum compliance design. Due to the much wider base compared to the neck region, the column primarily buckles at the neck region, as shown in Fig. 7.17. Instead of increasing the overall second moment of area like the designs in previous section, the enhanced buckling resistance is partly attributed to the decreased effective length of the buckling column. The effective length decreases from the height of the entire column to the height of the neck region.

In this example, the mesh density is limited by the computational cost from the sensitivities evaluation, resulting in failing to generate a detail design at the neck region. Although the optimised design effectively improves the buckling resistance, a more efficient implementation is needed in the future work to fully address the buckling resistance optimisation in 3D. Note that the optimisation with manufacturing constraints is not considered in this section due



(a)



(b)

Figure 7.17: The first and third buckling modes of (a) minimum compliance design and (b) buckling resistance design

to the limitation of the mesh density and the extra computational cost whilst enabling the manufacturing constraints.

Table 7.3: The problem setup of the twisted and compressed column (maximisation of buckling resistance)

Mesh	
Element	3D tetrahedral
L_x	2 m
L_y	1 m
L_z	1 m
b	0.2 m
Element size	1/25 m
Number of elements	150,639
Number of design variables	264,035
Optimisation	
r_h (Helmholtz filter radius)	1/12.5 m
r_b (Helmholtz filter boundary radius)	1/12.5 m
p (SIMP parameter)	$3 \rightarrow 6$ (continuation)
β (projection parameter)	$2 \rightarrow 16$ (continuation)
V_0 (target volume)	15%
c (compliance constraint constant)	2
Initial guesses	
ρ	0.12
(U_x, U_y, U_z)	(1,0,0)
V_f	0.5
Material properties	
E_f	200 Pa
E_m	10 Pa
ν_f	0.3
ν_m	0.3

7.6 Summary

In this chapter, the optimisation results accounting for buckling resistance are presented. The buckling resistance of each case is summarised in Tab. 7.4 which shows that all of the designs demonstrate significant improvements compared to the corresponding minimum compliance designs. The designs in 2D have shown similar topology layout, comparing to the previous studies using isotropic materials. The advantage of using anisotropic continuous fibre is evidenced by the comparison with the isotropic random-oriented short fibre in the 2D compressed column

case, where the buckling load factor of the design using continuous fibre is 2.13 times greater. Although the improvements in the cases, where the manufacturing constraints are enabled, are not as large as in the other cases, the promising manufacturability with the improved buckling resistance shown in these cases prove the developed framework successfully achieve the objective of improving the buckling resistance whilst accounting for the manufacturability.

Table 7.4: The summary of the buckling resistance. Note that * denotes the case with random-oriented short fibre, and the improvement is compared to the corresponding minimum compliance design

Cases	Manufacturing constraints	BLFs	Improvement
Compressed column	Disabled	8.56	392%
	Enabled	6.69	284%
	Disabled *	4.01	361%
Stubby cantilever	Disabled	13.28	233%
	Enabled	8.27	107%
MBB beam	Disabled	4.15	603%
	Enabled	2.7	358%
Twisted and compressed column	Disabled	6.53	72%

Chapter 8

Conclusion

A novel topology and fibre orientation optimisation framework accounting for manufacturability is successfully implemented and presented in this thesis. Using the rule of mixtures to link the fibre volume fraction to the material properties is the first step in connecting the design framework to manufacturing. The desired continuous fibres are ensured, furthermore, when the fibre volume fraction is also coupled to the fibre orientation by the continuity constraints. This brings the optimisation results closer to manufacturable designs. The fibre path generation constraints successfully use the scalar fields to interpret the fibre volume fraction and the fibre orientation which not only reconstructs the model for visualisation but also provides sufficient information for the subsequent manufacturing stages.

To avoid the potential buckling failure, an extension accounting for buckling resistance based on the combination of topology and fibre orientation optimisation framework is also successfully implemented and presented in this thesis. Linear buckling analysis is incorporated to analyse and optimise for buckling behaviour, and strategies to prevent mode switching and spurious modes are included.

To validate the microscale model and the manufacturing constraints, a 2D cantilever beam problem and a 2D beam with holes problem solely focus on the optimisation of fibre orientation are solved. The material properties description and the rotation function are clearly validated through the varying fibre orientation and fibre volume fraction. The designs without

the manufacturing constraints, show significant improvements in compliance, 35% and 15% respectively, compared to the straight fibre orientation FRCs. For the designs with manufacturing constraints, although the improvement in stiffness is not as significant as in the cases without the manufacturing constraints, the successfully interpreted fibre path with corresponding fibre volume fraction demonstrates the effectiveness of these constraints.

A cantilever beam problem with five optimisation scenarios are presented to demonstrate the efficacy of the combination of topology and fibre orientation optimisation accounting for manufacturing. A reduction of 62% in the compliance of the spatially-optimised case is noted in comparison to the isotropic case. Although the compliance increases 36% and 65% in the manufacturing constraints cases, compared to the spatially-optimised case, the fibre continuity, the variation of the fibre volume fraction and the manufacturability are well controlled in these cases. The comparison to the unidirectional case which is currently manufacturable by commercial desktop printers illustrates that compromising with the manufacturing constraints by decreasing the fibre volume fraction and having the non-optimal fibre orientation in some part of the structure demonstrated in the fibre path generation case still results in a better design.

The twisted and compressed column and the L-shape beam problems demonstrate the ability of handling multiple loading case and complex geometry of the presented framework although the compromises in the compliance still exist whilst improving manufacturability. However, the buckling analyses of the optimal designs indicate that the potential of buckling failure is high.

To demonstrate the potential of using fibre-reinforced materials and the effectiveness of the framework on buckling resistance, fibre-reinforced cases are initially benchmarked against an isotropic case using short random-oriented fibres. The results show that the buckling load factor of the unconstrained continuous fibre case is 133% higher the short random-oriented case. In three loading scenarios, the unconstrained cases exhibit better buckling resistance, but they also exhibit undesired manufacturing issues and overestimated buckling resistance. Although the constrained cases are outperformed by the unconstrained cases, when compared to the minimum compliance design, they still show significant improvements in buckling resistance. The twisted and compressed column solved in 3D also shows significant improvement on the

buckling resistance, although the details of the topology is not as much as those designs in 2D due to the low mesh density limited by the computation cost and time.

The methodology presented in this thesis enables manufacturable optimised FRC structures with realistic fibre volume fraction. The manufacturing issues are alleviate through the novel manufacturing constraints. The information provided by the isosurfaces saves the additional efforts in interpreting the printer toolpaths, and the realistic fibre volume fraction improves the modelling accuracy. In addition, the results have also demonstrated the advantages of using continuous FRCs to enhance buckling resistance. Furthermore, manufacturability of the designs can be well ensured, accompanied by a significant improvement in buckling resistance.

8.1 Summary of Thesis Achievements

The specific achievements of this thesis are summarised as follows:

- The fibre path generated through the isosurfaces successfully interprets the element-wise fibre orientation and provides sufficient information for further fabrication processes, saving additional effort required for post-processing on the fibre path and the printer toolpaths.
- The manufacturing issues, such as sharp fibre turns, resin rich areas, and overestimated compliance, are alleviated by the novel continuity, orthogonality and aspect ratio constraints.
- The buckling resistance of the optimal designs is improved through the maximisation of the buckling load factor even when manufacturability is considered.

8.2 Limitations and Future Work

One limitation of the work presented in this thesis is that the considered manufacturability is based on the assumption of a potential integration with 3D printing technology, which has not yet been implemented in commercial printers. It is possible to adapt the approach to

fit existing 3D printing techniques by fixing the bound of the fibre volume fraction to be constant. However, this will result in a numerical challenge to parameterise the spatially-varying fibre orientation vector that achieves minimal compliance without violating the continuity or magnitude constraint.

Another limitation observed from the optimal designs is that the manufacturing constraints shrink the design space in some cases, resulting in compromising the fibre orientation or fibre volume fraction in some of the design domain to fulfil the constraints. One possible way to alleviate this is to use the stacking concept rooted in 3D printing techniques by including multiple sets of fibre orientation. The material properties can be evaluated through the homogeneous theory, and the manufacturability can be ensured by implementing the manufacturing constraints individually in each set of design variables. Although the variation of each set of the design variables may still be limited, the overall design space for the multiple sets of design variables is enlarged.

The expensive computational cost in the 3D cases whilst considering the buckling resistance is a huge limitation encountered. The limited element size results in rough designs without the full design freedom to determine the length scale of the design. The assembly of the gradient term and the multiple linear algebra computations of the adjoint displacement fields slow the sensitivity evaluation. The assembly of the gradient term can possibly be accelerated though extending the compact expression introduced in Ferrari et al. (2021) to 3D. The multiple linear algebra computations, which are solved concurrently using a single core for each displacement field, could be accelerated by implementing concurrently parallel computations. Another suggestion is to use a GPU-compatible solver to further accelerate the linear algebra computation.

The competition between the compliance and the buckling resistance results in a multi-objective optimisation problem. Setting the compliance as a constraint is the approach applied here; however, the suitable compliance constraint constant varies case by case, which is an obstacle to achieving the global optimum. Depending on the problem definition and the ultimate objective, using subjective weighted objectives or setting the buckling load factor as a constraint is worth to implement to achieve the global optimum for future work.

Bibliography

Abdalla, M. M., Setoodeh, S., and Gürdal, Z. (2007). Design of variable stiffness composite panels for maximum fundamental frequency using lamination parameters. *Composite Structures*, 81:283–291.

Allaire, G., Jouve, F., and Toader, A. M. (2002). A level-set method for shape optimization. *Comptes Rendus Mathematique*, 334:1125–1130.

Allaire, G., Jouve, F., and Toader, A. M. (2004). Structural optimization using sensitivity analysis and a level-set method. *Journal of Computational Physics*, 194:363–393.

Alnaes, M. S., Blechta, J., Hake, J., Johansson, A., Kehlet, B., Logg, A., Richardson, C., Ring, J., Rognes, M. E., and Wells, G. N. (2015). The fenics project version 1.5. *Archive of Numerical Software*, 3.

Antonio, C. A. C. (2006). A hierarchical genetic algorithm with age structure for multimodal optimal design of hybrid composites. *Structural and Multidisciplinary Optimization*, 31:280–294.

Aragh, B. S., Farahani, E. B., Xu, B. X., Ghasemnejad, H., and Mansur, W. J. (2021). Manufacturable insight into modelling and design considerations in fibre-steered composite laminates: State of the art and perspective. *Computer Methods in Applied Mechanics and Engineering*, 379:113752.

Avanzini, A., Battini, D., Petrogalli, C., Pandini, S., and Donzella, G. (2022). Anisotropic Behaviour of Extruded Short Carbon Fibre Reinforced PEEK Under Static and Fatigue Loading. *Applied Composite Materials*, 29(3):1041–1060.

Bažant, Z. P. and Cedolin, L. (2010). *Stability of Structures*. World Scientific.

Bendsøe, M. P. (1989). Optimal shape design as a material distribution problem. *Structural optimization 1989 1:4*, 1(4):193–202.

Bendsøe, M. P., Guedes, J. M., Haber, R. B., Pedersen, P., and Taylor, J. E. (1994). An analytical model to predict optimal material properties in the context of optimal structural design. *Journal of Applied Mechanics*, 61:930–937.

Bendsøe, M. P. and Kikuchi, N. (1988). Generating optimal topologies in structural design using a homogenization method. *Computer Methods in Applied Mechanics and Engineering*, 71:197–224.

Bendsøe, M. P. and Sigmund, O. (1999). Material interpolation schemes in topology optimization. *Archive of Applied Mechanics*, 69:635–654.

Bendsøe, M. P. and Sigmund, O. O. (2004). *Topology optimization : theory, methods, and applications*. Springer.

Boddeti, N., Tang, Y., Maute, K., Rosen, D. W., and Dunn, M. L. (2020). Optimal design and manufacture of variable stiffness laminated continuous fiber reinforced composites. *Scientific Reports*, 10:16507.

Bourdin, B. (2001). Filters in topology optimization. *International Journal for Numerical Methods in Engineering*, 50:2143–2158.

Brampton, C. J., Wu, K. C., and Kim, H. A. (2015). New optimization method for steered fiber composites using the level set method. *Structural and Multidisciplinary Optimization*, 52:493–505.

Bruns, T. E. and Tortorelli, D. A. (2001). Topology optimization of non-linear elastic structures and compliant mechanisms. *Computer Methods in Applied Mechanics and Engineering*, 190:3443–3459.

Bruyneel, M. (2011). Sfp-a new parameterization based on shape functions for optimal material selection: Application to conventional composite plies. *Structural and Multidisciplinary Optimization*, 43:17–27.

Bruyneel, M., Colson, B., and Remouchamps, A. (2007). Discussion on some convergence problems in buckling optimisation. *Structural and Multidisciplinary Optimization 2007 35:2*, 35:181–186.

Bruyneel, M. and Fleury, C. (2002). Composite structures optimization using sequential convex programming. *Advances in Engineering Software*, 33(7-10):697–711.

Burger, M., Hackl, B., and Ring, W. (2004). Incorporating topological derivatives into level set methods. *Journal of Computational Physics*, 194:344–362.

Caivano, R., Tridello, A., Paolino, D., and Chiandussi, G. (2020). Topology and fibre orientation simultaneous optimisation: A design methodology for fibre-reinforced composite components. *Proceedings of the Institution of Mechanical Engineers, Part L: Journal of Materials: Design and Applications*, 234:1267–1279.

Chen, X., Fang, G., Liao, W. H., and Wang, C. C. (2022). Field-based toolpath generation for 3d printing continuous fibre reinforced thermoplastic composites. *Additive Manufacturing*, 49:102470.

Cheng, H. C., Kikuchi, N., and Ma, Z. D. (1994). An improved approach for determining the optimal orientation of orthotropic material. *Structural Optimization*, 8:101–112.

Cho, H. K. and Rowlands, R. E. (2009). Optimizing fiber direction in perforated orthotropic media to reduce stress concentration. *Journal of Composite Materials*, 43:1177–1198.

Christensen, A. K. P. W. (2008). *An Introduction to Structural Optimization*. Springer Netherlands.

Clausen, A. and Andreassen, E. (2017). On filter boundary conditions in topology optimization. *Structural and Multidisciplinary Optimization*, 56:1147–1155.

Clyne, T. W. and Hull, D. (2019). *An Introduction to Composite Materials*. Cambridge University Press.

Crothers, P. J., Drechsler, K., Feltin, D., Herszberg, I., and Bannister, M. (1997). The design and application of tailored fibre placement. *Proceedings of ICCM–11*, July 1997, Gold Coast, Australia.

Dalklint, A., Wallin, M., and Tortorelli, D. A. (2021). Structural stability and artificial buckling modes in topology optimization. *Structural and Multidisciplinary Optimization*, 64:1751–1763.

Diaconu, C. G., Sato, M., and Sekine, H. (2012). Feasible region in general design space of lamination parameters for laminated composites. *AIAA Journal*, 40:559–565.

Dickson, A. N., Abourayana, H. M., and Dowling, D. P. (2020). 3D printing of fibre-reinforced thermoplastic composites using fused filament fabrication—a review. *Polymers*, 12:2188.

Dijk, N. P. V., Maute, K., Langelaar, M., and Keulen, F. V. (2013). Level-set methods for structural topology optimization: A review. *Structural and Multidisciplinary Optimization*, 48:437–472.

Dunning, P. D. (2023). Stability constraints for geometrically nonlinear topology optimization. *Structural and Multidisciplinary Optimization*, 66:1–17.

Dunning, P. D., Ovtchinnikov, E., Scott, J., and Kim, H. A. (2016). Level-set topology optimization with many linear buckling constraints using an efficient and robust eigensolver. *International Journal for Numerical Methods in Engineering*, 107:1029–1053.

Díaz, A. and Sigmund, O. (1995). Checkerboard patterns in layout optimization. *Structural Optimization*, 10:40–45.

Díaz, A. R. and Bendsøe, M. P. (1992). Shape optimization of structures for multiple loading conditions using a homogenization method. *Structural Optimization*, 4:17–22.

Fang, G., Zhang, T., Zhong, S., Chen, X., Zhong, Z., and Wang, C. C. L. (2020). Reinforced fdm: multi-axis filament alignment with controlled anisotropic strength. *ACM Trans. Graph.*, 39(6):1–15.

Ferrari, F. and Sigmund, O. (2019). Revisiting topology optimization with buckling constraints. *Structural and Multidisciplinary Optimization*, 59:1401–1415.

Ferrari, F. and Sigmund, O. (2020). Towards solving large-scale topology optimization problems with buckling constraints at the cost of linear analyses. *Computer Methods in Applied Mechanics and Engineering*, 363:112911.

Ferrari, F. and Sigmund, O. (2023). A strategy for avoiding spurious localized buckling modes in topology optimization. *International Journal for Numerical Methods in Engineering*, 124(18):4118–4140.

Ferrari, F., Sigmund, O., and Guest, J. K. (2021). Topology optimization with linearized buckling criteria in 250 lines of matlab. *Structural and Multidisciplinary Optimization*, 63:3045–3066.

Fulmanski, P., Laurain, A., Scheid, J. F., and Sokoowski, J. (2008). Level set method with topological derivatives in shape optimization. *International Journal of Computer Mathematics*, 85(10):1491–1514.

Gao, T., Zhang, W., and Duysinx, P. (2012). A bi-value coding parameterization scheme for the discrete optimal orientation design of the composite laminate. *International Journal for Numerical Methods in Engineering*, 91:98–114.

Gao, X. and Ma, H. (2015). Topology optimization of continuum structures under buckling constraints. *Computers & Structures*, 157:142–152.

Gea, H. C. and Luo, J. H. (2004). On the stress-based and strain-based methods for predicting optimal orientation of orthotropic materials. *Structural and Multidisciplinary Optimization*, 26:229–234.

Geier, B. and Zimmermann, R. (1994). Composite laminate stiffnesses and their sensitivities. *Proceedings of the ASME Design Engineering Technical Conference*, Part F167892-7:237–246.

Ghiasi, H., Fayazbakhsh, K., Pasini, D., and Lessard, L. (2010). Optimum stacking sequence design of composite materials part ii: Variable stiffness design. *Composite Structures*, 93:1–13.

Ghiasi, H., Pasini, D., and Lessard, L. (2009). Optimum stacking sequence design of composite materials part i: Constant stiffness design. *Composite Structures*, 90:1–11.

GrabCAD (2013). GE jet engine bracket challenge. `https://grabcad.com/challenges/ge-jet-engine-bracket-challenge`. Assessed: 07/07/2022.

Gravesen, J., Evgrafov, A., and Nguyen, D. M. (2011). On the sensitivities of multiple eigenvalues. *Structural and Multidisciplinary Optimization*, 44:583–587.

Guest, J. K., Prévost, J. H., and Belytschko, T. (2004). Achieving minimum length scale in topology optimization using nodal design variables and projection functions. *International Journal for Numerical Methods in Engineering*, 61:238–254.

Gürdal, Z., Tatting, B. F., and Wu, C. K. (2008). Variable stiffness composite panels: Effects of stiffness variation on the in-plane and buckling response. *Composites Part A: Applied Science and Manufacturing*, 39:911–922.

Hammer, V. B., Bendsøe, M. P., Lipton, R., and Pedersen, P. (1997). Parametrization in laminate design for optimal compliance. *International Journal of Solids and Structures*, 34:415–434.

Huang, J. and Haftka, R. T. (2005). Optimization of fiber orientations near a hole for increased load-carrying capacity of composite laminates. *Structural and Multidisciplinary Optimization*, 30:335–341.

Huang, Y., Zhang, J., Hu, X., Song, G., Liu, Z., Yu, L., and Liu, L. (2016). Framefab: robotic fabrication of frame shapes. *ACM Trans. Graph.*, 35(6):1–11.

Hvejsel, C. F. and Lund, E. (2011). Material interpolation schemes for unified topology and multi-material optimization. *Structural and Multidisciplinary Optimization*, 43:811–825.

Hyer, M. W. and Charette, R. F. (1991). Use of curvilinear fiber format in composite structure design. *AIAA Journal*, 29:1011–1015.

Jantos, D. R., Hackl, K., and Junker, P. (2020). Topology optimization with anisotropic materials, including a filter to smooth fiber pathways. *Structural and Multidisciplinary Optimization*, 61:2135–2154.

Jog, C. S. and Haber, R. B. (1996). Stability of finite element models for distributed-parameter optimization and topology design. *Computer Methods in Applied Mechanics and Engineering*, 130(3):203–226.

Jung, T., Lee, J., Nomura, T., and Dede, E. M. (2022). Inverse design of three-dimensional fiber reinforced composites with spatially-varying fiber size and orientation using multiscale topology optimization. *Composite Structures*, 279:114768.

Jørgensen, O. (1991). Optimization of the flutter load by material orientation. *Journal of Structural Mechanics*, 19:411–436.

Keane, A. J. and Nair, P. B. (2005). *Computational approaches for aerospace design: The pursuit of excellence*. Wiley.

Keller, D. (2010). Optimization of ply angles in laminated composite structures by a hybrid, asynchronous, parallel evolutionary algorithm. *Composite Structures*, 92:2781–2790.

Khani, A., Abdalla, M. M., Gürdal, Z., Sinke, J., Buitenhuis, A., and Tooren, M. J. V. (2017). Design, manufacturing and testing of a fibre steered panel with a large cut-out. *Composite Structures*, 180:821–830.

Khani, A., Ijsselmuiden, S. T., Abdalla, M. M., and Gürdal, Z. (2011). Design of variable stiffness panels for maximum strength using lamination parameters. *Composites Part B: Engineering*, 42:546–552.

Kim, J. S., Kim, C. G., and Hong, C. S. (1999). Optimum design of composite structures with ply drop using genetic algorithm and expert system shell. *Composite Structures*, 46:171–187.

Kocvara, M., Stingl, M., and Zowe, J. (2008). Free material optimization: recent progress. *Optimization*, 57:79–100.

Kreisselmeier, G. and Steinhauser, R. (1979). Systematic control design by optimizing a vector performance index. *IFAC Proceedings Volumes*, 12:113–117.

Lazarov, B. S. and Sigmund, O. (2011). Filters in topology optimization based on helmholtz-type differential equations. *International Journal for Numerical Methods in Engineering*, 86:765–781.

Lee, J., Kim, D., Nomura, T., Dede, E. M., and Yoo, J. (2018). Topology optimization for continuous and discrete orientation design of functionally graded fiber-reinforced composite structures. *Composite Structures*, 201:217–233.

Li, R., Kelly, D., and Crosky, A. (2002). Strength improvement by fibre steering around a pin loaded hole. *Composite Structures*, 57:377–383.

Li, S. and Atluri, S. N. (2008). The MLPG mixed collocation method for material orientation and topology optimization of anisotropic solids and structures. *Computer Modeling in Engineering & Sciences*, 30:37–56.

Lindgaard, E. and Lund, E. (2010). Nonlinear buckling optimization of composite structures. *Computer Methods in Applied Mechanics and Engineering*, 199:2319–2330.

Liu, B. and Haftka, R. T. (2001). Composite wing structural design optimization with continuity constraints. *19th AIAA Applied Aerodynamics Conference*, June 2001, Anaheim, California.

Liu, T., Tian, X., Zhang, Y., Cao, Y., and Li, D. (2020). High-pressure interfacial impregnation by micro-screw in-situ extrusion for 3d printed continuous carbon fiber reinforced nylon composites. *Composites Part A: Applied Science and Manufacturing*, 130:105770.

Luo, J., Luo, Z., Chen, L., Tong, L., and Wang, M. Y. (2008). A semi-implicit level set method for structural shape and topology optimization. *Journal of Computational Physics*, 227:5561–5581.

Luo, J. H. and Gea, H. C. (1998). Optimal orientation of orthotropic materials using an energy based method. *Structural Optimization*, 15:230–236.

Luo, Y. R., Hewson, R., and Santer, M. (2023). Spatially optimised fibre-reinforced composites with isosurface-controlled additive manufacturing constraints. *Structural and Multidisciplinary Optimization*, 66:1–14.

Matsuzaki, R., Nakamura, T., Sugiyama, K., Ueda, M., Todoroki, A., Hirano, Y., and Yamagata, Y. (2018). Effects of set curvature and fiber bundle size on the printed radius of curvature by a continuous carbon fiber composite 3D printer. *Additive Manufacturing*, 24:93–102.

Mattheck, C. and Burkhardt, S. (1990). A new method of structural shape optimization based on biological growth. *International Journal of Fatigue*, 12:185–190.

Matveev, M. Y., Schubel, P. J., Long, A. C., and Jones, I. A. (2016). Understanding the buckling behaviour of steered tows in automated dry fibre placement (ADFP). *Composites Part A: Applied Science and Manufacturing*, 90:451–456.

Mitusch, S. K., Funke, S. W., and Dokken, J. S. (2019). dolfin-adjoint 2018.1: automated adjoints for fenics and firedrake. *Journal of Open Source Software*, 4:1292.

Neves, M. M., Rodrigues, H., and Guedes, J. M. (1995). Generalized topology design of structures with a buckling load criterion. *Structural Optimization*, 10:71–78.

Nomura, T., Dede, E. M., Lee, J., Yamasaki, S., Matsumori, T., Kawamoto, A., and Kikuchi, N. (2015). General topology optimization method with continuous and discrete orientation design using isoparametric projection. *International Journal for Numerical Methods in Engineering*, 101:571–605.

Nomura, T., Kawamoto, A., Kondoh, T., Dede, E. M., Lee, J., Song, Y., and Kikuchi, N. (2019). Inverse design of structure and fiber orientation by means of topology optimization with tensor field variables. *Composites Part B: Engineering*, 176:107187.

Osher, S. and Sethian, J. A. (1988). Fronts propagating with curvature-dependent speed: Algorithms based on hamilton-jacobi formulations. *Journal of Computational Physics*, 79:12–49.

Papapetrou, V. S., Patel, C., and Tamijani, A. Y. (2020). Stiffness-based optimization framework for the topology and fiber paths of continuous fiber composites. *Composites Part B: Engineering*, 183:107681.

Parnas, L., Oral, S., and Ümit Ceyhan (2003). Optimum design of composite structures with curved fiber courses. *Composites Science and Technology*, 63:1071–1082.

Pedersen, N. L. and Pedersen, P. (2018). Buckling load optimization for 2D continuum models, with alternative formulation for buckling load estimation. *Structural and Multidisciplinary Optimization*, 58:2163–2172.

Pedersen, P. (1989). On optimal orientation of orthotropic materials. *Structural Optimization*, 1:101–106.

Pedersen, P. (1990). Bounds on elastic energy in solids of orthotropic materials. *Structural Optimization*, 2:55–63.

Pedersen, P. (1991). Structural optimization on thickness and orientational design with orthotropic materials. *Structural Optimization*, 3:69–78.

Pelzer, L. and Hopmann, C. (2021). Additive manufacturing of non-planar layers with variable layer height. *Additive Manufacturing*, 37:101697.

Petersson, J. (1999). A finite element analysis of optimal variable thickness sheets. *SIAM Journal on Numerical Analysis*, 36(6):1759–1778.

Rao, S. S. (2019). *Engineering optimization: Theory and practice*. Wiley.

Raspanti, C. G., Bandoni, J. A., and Biegler, L. T. (2000). New strategies for flexibility analysis and design under uncertainty. *Computers & Chemical Engineering*, 24:2193–2209.

Rion, V. and Bruyneel, M. (2006). Topology optimization of membranes made of orthotropic material. In *Collection of Papers from Prof. Nguyen Dang Hung's Former Students*. Vietnam National University-HCM Publishing House.

Rodrigues, H. C., Guedes, J. M., and Bendsøe, M. P. (1995). Necessary conditions for optimal design of structures with a nonsmooth eigenvalue based criterion. *Structural optimization*, 9:52–56.

Rojas-Labanda, S. and Stolpe, M. (2015). Benchmarking optimization solvers for structural topology optimization. *Structural and Multidisciplinary Optimization*, 52:527–547.

Sanomura, Y. and Kawamura, M. (2003). Fiber orientation control of short-fiber reinforced thermoplastics by ram extrusion. *Polymer Composites*, 24(5):587–596.

Schmidt, M. P., Couret, L., Gout, C., and Pedersen, C. B. (2020). Structural topology optimization with smoothly varying fiber orientations. *Structural and Multidisciplinary Optimization*, 62:3105–3126.

Sethain, J. (1999). *Level set methods and fast marching*. Cambridge University Press.

Setoodeh, S., Abdalla, M. M., and Gürdal, Z. (2005). Combined topology and fiber path design of composite layers using cellular automata. *Structural and Multidisciplinary Optimization*, 30:413–421.

Setoodeh, S., Abdalla, M. M., and Gürdal, Z. (2006a). Design of variable–stiffness laminates using lamination parameters. *Composites Part B: Engineering*, 37:301–309.

Setoodeh, S., Abdalla, M. M., IJsselmuiden, S. T., and Gürdal, Z. (2009). Design of variable-stiffness composite panels for maximum buckling load. *Composite Structures*, 87:109–117.

Setoodeh, S., Gürdal, Z., and Watson, L. T. (2006b). Design of variable-stiffness composite layers using cellular automata. *Computer Methods in Applied Mechanics and Engineering*, 195:836–851.

Seyraniant, A. P., Lund, E., and Olhoff, N. (1994). Multiple eigenvalues in structural optimization problems*. *Structural Optimization*, 8:207–227.

Shafighfard, T., Cender, T. A., and Demir, E. (2021). Additive manufacturing of compliance optimized variable stiffness composites through short fiber alignment along curvilinear paths. *Additive Manufacturing*, 37:101728.

Sigmund, O. (2007). Morphology-based black and white filters for topology optimization. *Structural and Multidisciplinary Optimization*, 33:401–424.

Sigmund, O. and Maute, K. (2013). Topology optimization approaches. *Structural and Multidisciplinary Optimization*, 48:1031–1055.

Sigmund, O. and Petersson, J. (1998). Numerical instabilities in topology optimization: A survey on procedures dealing with checkerboards, mesh-dependencies and local minima. *Structural Optimization*, 16:68–75.

Sigmund, O. and Torquato, S. (1997). Design of materials with extreme thermal expansion using a three-phase topology optimization method. *Journal of the Mechanics and Physics of Solids*, 45:1037–1067.

Stegmann, J. and Lund, E. (2005). Discrete material optimization of general composite shell structures. *International Journal for Numerical Methods in Engineering*, 62:2009–2027.

Stolpe, M. and Bendsøe, M. P. (2011). Global optima for the zhou–rozvany problem. *Structural and Multidisciplinary Optimization*, 43:151–164.

Sun, M. and Hyer, M. W. (2012). Use of material tailoring to improve buckling capacity of elliptical composite cylinders. *AIAA Journal*, 46:770–782.

Suzuki, K. and Kikuchi, N. (1991). A homogenization method for shape and topology optimization. *Computer Methods in Applied Mechanics and Engineering*, 93:291–318.

Svanberg, K. (1987). The method of moving asymptotes—a new method for structural optimization. *International Journal for Numerical Methods in Engineering*, 24:359–373.

Svanberg, K. and Werme, M. (2006). Topology optimization by a neighbourhood search method based on efficient sensitivity calculations. *International Journal for Numerical Methods in Engineering*, 67:1670–1699.

Tosh, M. W. and Kelly, D. W. (2000). On the design, manufacture and testing of trajectorial fibre steering for carbon fibre composite laminates. *Composites Part A: Applied Science and Manufacturing*, 31:1047–1060.

Tosh, M. W. and Kelly, D. W. (2001). Fibre steering for a composite c-beam. *Composite Structures*, 53:133–141.

van Campen, J. M., Kassapoglou, C., and Gürdal, Z. (2012). Generating realistic laminate fiber angle distributions for optimal variable stiffness laminates. *Composites Part B: Engineering*, 43:354–360.

Wallin, M., Ivarsson, N., Amir, O., and Tortorelli, D. (2020). Consistent boundary conditions for pde filter regularization in topology optimization. *Structural and Multidisciplinary Optimization*, 62:1299–1311.

Wang, F., Lazarov, B. S., and Sigmund, O. (2011). On projection methods, convergence and robust formulations in topology optimization. *Structural and Multidisciplinary Optimization*, 43:767–784.

Wang, F., Lazarov, B. S., Sigmund, O., and Jensen, J. S. (2014). Interpolation scheme for fictitious domain techniques and topology optimization of finite strain elastic problems. *Computer Methods in Applied Mechanics and Engineering*, 276:453–472.

Wang, M. Y., Wang, X., and Guo, D. (2003). A level set method for structural topology optimization. *Computer Methods in Applied Mechanics and Engineering*, 192:227–246.

Whalen, E., Beyene, A., and Mueller, C. (2021). Simjeb: Simulated jet engine bracket dataset. *Computer Graphics Forum*, 40:9–17.

Wu, K. C. (2008). Design and analysis of tow-steered composite shells using fiber placement -

core. *American Society for Composites 23rd Annual Technical Conference*, September 2008, Memphis, Tennessee.

Wu, Z., Raju, G., White, S., and Weaver, P. M. (2014). Optimal design of post-buckling behaviour of laminated composite plates using lamination parameters. *55th AIAA/ASMe/ASCE/AHS/SC Structures, Structural Dynamics, and Materials Conference*, January 2014, National Harbor, Maryland.

Wu, Z., Weaver, P. M., Raju, G., and Kim, B. C. (2012). Buckling analysis and optimisation of variable angle tow composite plates. *Thin-Walled Structures*, 60:163–172.

Wächter, A. and Biegler, L. T. (2005). On the implementation of an interior-point filter line-search algorithm for large-scale nonlinear programming. *Mathematical Programming*, 106:25–57.

Xie, Y. M. and Steven, G. P. (1993). A simple evolutionary procedure for structural optimization. *Computers & Structures*, 49:885–896.

Xu, S., Cai, Y., and Cheng, G. (2010). Volume preserving nonlinear density filter based on heaviside functions. *Structural and Multidisciplinary Optimization*, 41:495–505.

Xu, T., Huang, X., Lin, X., and Xie, Y. M. (2023). Topology optimization for maximizing buckling strength using a linear material model. *Computer Methods in Applied Mechanics and Engineering*, 417:116437.

Yamasaki, S., Nishiwaki, S., Yamada, T., Izui, K., and Yoshimura, M. (2010). A structural optimization method based on the level set method using a new geometry-based re-initialization scheme. *International Journal for Numerical Methods in Engineering*, 83:1580–1624.

Young, V., Querin, O. M., Steven, G. P., and Xie, Y. M. (1999). 3d and multiple load case bi-directional evolutionary structural optimization (beso). *Structural optimization 1999 18:2*, 18:183–192.

Zabinsky, Z. B., Tuttle, M. E., and Khompatraporn, C. (2006). A case study: Composite structure design optimization. In *Global Optimization*. Springer, Boston, MA.

Zelinski, P. (2022). Faster fff build rate using rectangular, variable-orifice nozzle (includes video) — additive manufacturing. `https://www.additivemanufacturing.media/articles/faster-fff-build-rate-using-rectangular-variable-orifice-nozzle-includes-video`. Accessed: 19/05/2022.

Zhou, M. and Rozvany, G. I. (1991). The COC algorithm, part II: Topological, geometrical and generalized shape optimization. *Computer Methods in Applied Mechanics and Engineering*, 89:309–336.

Zowe, J., Kočvara, M., and Bendsøe, M. P. (1997). Free material optimization via mathematical programming. *Mathematical Programming*, 79:445–466.